

THESIS FOR THE DEGREE OF DOCTOR OF PHILOSOPHY

Parametric interactions with signals and the vacuum

MICHAËL SIMOEN

Department of Microtechnology and Nanoscience (MC2)
CHALMERS UNIVERSITY OF TECHNOLOGY
Göteborg, Sweden 2015

Parametric interactions with signals and the vacuum
MICHAËL SIMOEN
ISBN 978-91-7597-299-2

© MICHAËL SIMOEN, 2015

Doktorsavhandlingar vid Chalmers tekniska högskola
Ny serie nr. 3980
ISSN 0346-718X

Technical Report MC2-322
ISSN 1652-0769

Quantum Device Physics Laboratory
Department of Microtechnology and Nanoscience (MC2)
Chalmers University of Technology
SE-412 96 Göteborg
Sweden
Telephone: +46 (0)31-772 1000

Cover:
An illustration of the stepped-impedance multimode coplanar waveguide resonator used in this thesis.

Chalmers Reproservice
Göteborg, Sweden 2015

Parametric interactions with signals and the vacuum
Thesis for the degree of Doctor of Philosophy
MICHAËL SIMOEN
Department of Microtechnology and Nanoscience (MC2)
Chalmers University of Technology

ABSTRACT

In this thesis I present different experiments on superconducting circuits exploring parametric interactions with external signals and the vacuum in the microwave regime. These parametric processes are the result of the periodic modulation of a property of a system which results in different interactions. The systems used in this thesis are circuits where the nonlinear inductance of a superconducting quantum interference device (SQUID) is parametrically driven.

I present the first experimental observation of the dynamical Casimir effect (DCE), since it was predicted in 1970. The DCE is an interaction between the vacuum and a periodically modulated boundary condition of the electromagnetic field, here implemented by a flux-tuned SQUID. In essence the modulated boundary will parametrically amplify the vacuum fluctuations which results in the pairwise generation of photons over a broad frequency range. I have characterized the system and measured the statistical properties of the emitted radiation to show that the radiation exhibits two-mode squeezing.

Next, I present measurements on a superconducting multimode resonator containing a SQUID. I show that it is possible to get parametric amplification by driving the SQUID at either twice the frequency of one of the modes or by driving it at the sum of two mode frequencies. In both cases I show that it is possible to reach quantum-limited noise performance.

In the same system I also demonstrate frequency conversion which occurs when the system is pumped at the difference frequency between two modes. Microwave photons are coherently transferred from one mode to the other. I show that the coupling strength depends linearly on the applied pump amplitude.

The thesis also contains a linearized theoretical model to describe and analyze the flux-pumped SQUID. The model describes an equivalent circuit element called the pumpistor, with an impedance which depends on the pump phase. I show that under specific conditions the impedance becomes real and negative allowing pump power to be injected into the circuit, providing gain.

Finally I also present a demonstration of an on-chip Mach-Zehnder interferometer. This experiment uses the tunability of the SQUID to provide a controllable phase shift in one of the interferometer arms. The transmission through the device can be modulated with a maximum change of 45 dB.

Keywords: parametric amplification, mode conversion, vacuum, dynamical Casimir effect, multimode resonator, superconducting circuits, SQUID, circuit-QED, pumpistor, interferometer

*Dedicated to two very important people:
Jenny, the love of my life, &
Vincent, the most beautiful son in the world.*

ACKNOWLEDGEMENTS

This thesis is the result of more than six years of work at QDP. During my time I have had the privilege to meet and work with many inspiring, dedicated and passionate people. I would like to start with expressing my gratitude towards my supervisors, professor Per Delsing and professor Chris Wilson. They gave me the opportunity to pursue my PhD at Chalmers and have supported me throughout the years with advice and knowledge. A special thanks to Chris, Sandbo and Pol for the fantastic time I had at the university of Waterloo. I really enjoyed the stay, both the long hours in the lab as well as the dinners in the evenings.

Next I would like to thank Jonas Bylander. I think you have been a great addition to the group, bringing order where there is a mess and red ink where there is a new manuscript. Thanks for all the advice and for making time for discussions even when your schedule is overfull.

A big thank you goes also to Arsalan Pourkabirian and Philip Krantz. I have shared office with you two for nearly six years and during that time we shared many laughs and frustrations. Thank you for putting up with me even when I already pulled out the Christmas tree in October.

I am grateful that I have been able to work with many bright people over the last years. I would like to thank all the PhD students and Post-docs from EMP both past and current: André, Andreas, Arsalan, Arseniy, Astghik, Baladitya, Ben, David, Fredrik, Gustav, Ida-Maria, Io-Chun, Kyle, Maria, Martin G., Martin S., Mathieu, Matthias, Philip, Sebastian, Seçkin, Simon, Tauno, Thomas and Tom. I am sure I missed a few, but you know if you belong on this list. A big thank you also to the rest of QDP and the colleagues of AQP for all their help and support.

A few of you have become more than just colleagues and I have the pleasure of calling you my friends. An extra special thanks to Sophie, André, Niclas, Sebastian, Mathieu, Philip and Arsalan for all the fun times, lunch discussions, trips, dinners, parties and BBQs we have spent together.

Next I would like to thank some invaluable people at QDP. A big thank you to Lars Jönsson, Staffan Pehrson and Jan Jacobsson for the fantastic technical support we receive! The same goes for Susannah Carlsson, Maria Tremblay, Marie Fredriksson and Ann-Marie Frykestig. Thank you for always being there, even when I spam you with my many questions. A special mention goes to Marie for introducing me to my sweetheart and for being a fantastic “fadder” to Vincent. I cannot thank you enough.

Finally I would like to thank my family and friends for their unrelenting support throughout the years. Thank you mom and dad for all the opportunities that you have given me. You have never said no and I would not have been here today without you. Also thank you to Anna-Karin and Lars for taking me up in your family and making Alingsås my home away from home. Last but not least, I would like to thank my beautiful fiancée Jenny. Thank you sweetheart for all your support and love. Thank you for being such a fantastic mom to Vincent. I do not know how I would have managed without you.

SYMBOLS & ABBREVIATIONS

Abbreviations

| | |
|-------|---|
| SQUID | Superconducting quantum interference device |
| CPW | Coplanar waveguide |
| UV | Ultraviolet |
| DCE | Dynamical Casimir effect |
| OPO | Optical parametric oscillator |
| JPA | Josephson parametric amplifier |
| HEMT | High-electron-mobility transistor |
| SNTJ | Shot-noise tunnel junction |
| IVC | Inner vacuum chamber |
| TMS | Two-mode squeezing |
| AWG | Arbitrary waveform generator |
| LO | Local oscillator |
| IF | Intermediate frequency |
| SNR | Signal-to-noise ration |

Constants

| | |
|---------|-------------------------|
| e | Electron charge |
| h | Planck constant |
| \hbar | Reduced Planck constant |
| k_B | Boltzmann constant |
| c | Speed of light |

Superconductivity

| | |
|---------------|--|
| Ψ | Superconducting wave function |
| n_p | Density of Cooper pairs |
| θ | Superconducting phase |
| Δ_{sc} | Half the superconducting energy gap |
| \mathbf{A} | Magnetic vector potential |
| ϕ | Phase difference across Josephson junction |
| I_c | Critical current of a Josephson junction |
| $I_{c,sq}$ | Critical current of the SQUID |
| I_{sq} | Current through the SQUID |
| R_N | Normal resistance |
| L_J | Josephson junction inductance |
| C_J | Josephson junction capacitance |
| L_{sq} | Josephson inductance of the SQUID |
| $L_{sq,0}$ | Josephson inductance of the SQUID at zero flux |

| | |
|--------------------|---------------------------------------|
| C_{sq} | SQUID capacitance |
| Φ | Magnetic flux |
| Φ_0 | Magnetic flux quantum |
| Φ_{DC} | DC magnetic flux |
| Φ_{AC} | AC magnetic flux amplitude |
| F | Normalized DC magnetic flux |
| δF | Normalized AC magnetic flux amplitude |

Circuit parameters

| | |
|------------------|--|
| Γ | Reflection coefficient |
| C_c | Coupling capacitor |
| Z_{C_c} | Impedance of the coupling capacitor |
| C_r | Equivalent lumped element capacitor |
| C_0 | Capacitance per unit length |
| C_{tot} | Total capacitance of lumped element circuit |
| L_r | Equivalent lumped element inductor |
| L_0 | Inductance per unit length |
| R_r | Equivalent lumped element resistor |
| α_0 | Loss per unit length |
| Z_r | Equivalent lumped element impedance |
| Z_0 | Characteristic impedance of the measurement line |
| Z_{CPW} | Characteristic impedance of the CPW |
| γ_0 | SQUID inductance participation ratio |
| d | Resonator CPW length |
| λ | Wavelength |
| ω_0 | Angular resonance frequency |
| v_p | Phase velocity |
| k_m | Angular wave number of mode m |
| ω_m | Angular resonance frequency of mode m |
| f_m | Resonance frequency of mode m |
| f_R | Bare resonator frequency (without SQUID) |
| u_m | Envelope function of mode m |
| Q^e | External quality factor |
| Q^i | Internal quality factor |
| Q | Total quality factor |

Parametric driving

| | |
|------------------------------------|--|
| f_p, ω_p | Pump frequency, angular pump frequency |
| P_p | Pump power |
| f_s, f_i | Signal frequency, idler frequency |
| ω_s | Angular signal frequency |
| $\theta_p, \theta_s, \Delta\theta$ | Pump phase, signal phase, phase difference |
| L_p | Pumpistor |

| | |
|------------------------|---|
| α_m | Duffing parameter of mode m |
| ϵ | Effective pump strength |
| ϵ_{th} | Parametric oscillation threshold |
| M_m | “Mass” of mode m |
| δ | Angular pump detuning |
| Δ | Angular signal detuning |
| A | Intra-cavity field amplitude |
| B | Incoming field amplitude |
| C | Outgoing field amplitude |
| Γ_m^e | Coupling rate of mode m |
| Γ_m^i | Internal damping rate of mode m |
| Γ_m | Total damping rate of mode m |
| G, G_s, G_i | Gain, signal gain, idler gain |
| BW, \sqrt{GBW} | Bandwidth, gain-bandwidth product |
| S | Reflection coefficient/Conversion coefficient |

DCE

| | |
|---|---|
| a | Mirror motion amplitude |
| L_{eff} | Effective length |
| δL_{eff} | Effective length modulation amplitude |
| $\bar{n}_\omega^{\text{in}}, n_\omega^{\text{out}}$ | Thermal input field, total output photon flux density |
| I, Q | The quadratures |
| P_{avg}, P | Total average power in both sidebands, output power |
| σ_1, σ_2 | Single-mode squeezing, two-mode squeezing |
| $g_{+-}^{(2)}$ | Normalized second-order correlation function |

Noise Calibration

| | |
|---------------------|---|
| N_{QL} | Quantum limit |
| T_{N} | Noise temperature |
| S_I | Current noise spectral density |
| P_{N} | Total noise power |
| R_{SNTJ} | Shot-noise tunnel junction resistance |
| R_{b} | Room temperature bias resistor |
| $V_{\text{b,RT}}$ | Room temperature bias voltage |
| $V_{\text{b,SNTJ}}$ | Bias voltage across the SNTJ |
| V_{co} | Crossover voltage between shot-noise and vacuum noise |
| f_{samp} | Sampling frequency |
| A_{IL} | Insertion loss factor |
| $T_{\text{N,IL}}$ | Noise temperature of the insertion loss element |
| T_{IL} | Physical temperature of the insertion loss element |
| N_{IL} | Number of added noise photons by the insertion loss element |
| $N_{\text{out,IL}}$ | Total noise at the output of the insertion loss element |

| | |
|---------------------------|---|
| T_{SNTJ} | Physical temperature of the SNTJ |
| N_{in} | Input noise of the unbiased SNTJ |
| G_{J} | Gain of the JPA |
| N_{J} | Added noise by the JPA |
| G_{SYS} | Gain of the measurement chain (from JPA onwards) |
| N_{SYS} | Added noise by the measurement chain (from JPA onwards) |
| G_{TOT} | Total gain from SNTJ calibration (including insertion loss) |
| S_{out} | Output signal level |
| N_{out} | Output noise level |
| SNR_{out} | Output signal-to-noise ratio |
| ΔSNR | Signal-to-noise ratio improvement |

Other

| | |
|------------------|--|
| T | Temperature |
| f | Frequency |
| ω | Angular frequency |
| V | Voltage |
| I | Current |
| ψ | Flux |
| \mathcal{L} | Lagrangian |
| J_n | Bessel function of the first kind |
| G_{CPW} | Gap between center conductor and ground planes (CPW) |
| W_{CPW} | Center conductor width (CPW) |

LIST OF PUBLICATIONS

This thesis is based on the work contained in the following papers:

- Paper A** C. M. Wilson, G. Johansson, A. Pourkabirian, M. Simoen, J. R. Johansson, T. Duty, F. Nori, and P. Delsing. Observation of the dynamical Casimir effect in a superconducting circuit. *Nature* **479**: 376, 2011. DOI: 10.1038/nature10561
- Paper B** K. M. Sundqvist, S. Kintag, M. Simoen, P. Krantz, M. Sandberg, C. M. Wilson, and P. Delsing. The pumpistor: A linearized model of a flux-pumped superconducting quantum interference device for use as a negative-resistance parametric amplifier. *Applied Physics Letters* **103**: 102603, 2013. DOI: 10.1063/1.4819881
- Paper C** M. Simoen, C. W. S. Chang, P. Krantz, J. Bylander, W. Wustmann, V. Shumeiko, P. Delsing, and C. M. Wilson. Characterization of a multimode coplanar waveguide parametric amplifier. *Journal of Applied Physics* **118**: 154501, 2015. DOI: 10.1063/1.4933265
- Paper D** M. Simoen, A. Bengtsson, J. Bylander, W. Wustmann, V. Shumeiko, C. M. Wilson, and P. Delsing. Intermode conversion in a superconducting multimode resonator. *Unpublished manuscript*, 2015
- Paper E** S. Schuermans, M. Simoen, M. Sandberg, P. Krantz, C. M. Wilson, and P. Delsing. An on-chip Mach-Zehnder interferometer in the microwave regime. *IEEE Transactions on Applied Superconductivity* **21**: 448, 2011. DOI: 10.1109/TASC.2010.2088354

Other papers that are outside the scope of this thesis:

- Paper I** M. U. Staudt, I.-C. Hoi, P. Krantz, M. Sandberg, M. Simoen, P. Bushev, N. Sangouard, M. Afzelius, V. S. Shumeiko, G. Johansson, P. Delsing, and C. M. Wilson. Coupling of an erbium spin ensemble to a superconducting resonator. *Journal of Physics B: Atomic, Molecular and Optical Physics* **45**: 124019, 2012. DOI: 10.1088/0953-4075/45/12/124019
- Paper II** P. Krantz, A. Bengtsson, M. Simoen, S. Gustavsson, V. Shumeiko, W. D. Oliver, C. M. Wilson, P. Delsing, and J. Bylander. Single-shot readout of a superconducting qubit using a Josephson parametric oscillator. arXiv: 1508.02886

CONTENTS

| | |
|--|-------------|
| Abstract | i |
| Acknowledgements | v |
| Symbols & Abbreviations | vii |
| List of publications | xi |
| Contents | xiii |
| | |
| 1 Introduction | 3 |
| | |
| 2 Theory | 7 |
| 2.1 Superconducting Circuits | 7 |
| 2.1.1 The Josephson effect and SQUIDs | 7 |
| 2.1.2 Resonator | 11 |
| 2.1.3 Multimode coplanar waveguide resonator | 14 |
| 2.2 Parametric Amplification | 20 |
| 2.2.1 Pumpistor | 21 |
| 2.2.2 Nondegenerate phase-insensitive parametric amplification | 24 |
| 2.3 Intermode conversion in a multimode resonator | 31 |
| 2.4 Dynamical Casimir Effect | 34 |
| 2.4.1 Introduction | 34 |
| 2.4.2 SQUID as tunable boundary condition | 38 |
| 2.4.3 Two-mode squeezing and second-order coherence | 39 |
| 2.5 On-chip Mach-Zehnder interferometer | 41 |
| | |
| 3 Experimental techniques | 45 |
| 3.1 Sample fabrication | 45 |
| 3.1.1 Photolithography | 45 |
| 3.1.2 Electron-beam lithography | 46 |
| 3.1.3 Two-angle evaporation | 48 |
| 3.2 Measurement techniques | 50 |
| 3.2.1 Cryogenics | 50 |
| 3.2.2 Microwave measurements | 53 |
| 3.3 Noise calibration | 58 |
| 3.3.1 Noise calibration setup | 58 |
| 3.3.2 Calculation of the added noise | 61 |

| | |
|---|------------|
| 4 Results | 67 |
| 4.1 The dynamical Casimir effect | 67 |
| 4.2 Parametric amplification in a multimode resonator | 71 |
| 4.2.1 Single-mode parametric amplification | 75 |
| 4.2.2 Multimode parametric amplification | 78 |
| 4.3 Intermode conversion in a multimode resonator | 82 |
| 4.4 On-chip Mach-Zehnder interferometer | 87 |
| 5 Conclusions and outlook | 93 |
| A Recipes for sample fabrication | 95 |
| A.1 Wafer cleaning | 95 |
| A.2 Photolithography for lift-off | 95 |
| A.3 Deposition of the contact pads | 96 |
| A.4 Protective resist and dicing | 96 |
| A.5 Electron-beam lithography for lift-off | 96 |
| A.6 Two-angle evaporation and lift-off | 97 |
| References | 99 |
| Paper A | 107 |
| Paper B | 121 |
| Paper C | 127 |
| Paper D | 139 |
| Paper E | 147 |

Thesis

1

Introduction

In 1831 Michael Faraday reported one of the first observations of a parametrically driven system.⁸ When experimenting with free liquid surfaces in a vertically vibrating container he observed the formation of standing surface waves. He noticed that each crest of the surface wave (referred to as a heap) oscillated once for every two periods of the applied vibration: “Each heap (identified by its locality) recurs or is re-formed in two complete vibrations of the sustaining surface...”.⁸ It took another 52 years until Lord Raleigh provided the first more general treatment of parametric oscillations.^{9,10}

The first applications of parametric processes were found in the field of radio communications. It was the Swedish electrical engineer Ernst Alexanderson who patented the so-called magnetic amplifier, which provides gain by modulating the inductance in an electric circuit.¹¹ These amplifiers have been used in transoceanic radio communication in the beginning of the twentieth century. Since then other implementations of parametric amplifiers have appeared. In the 1950s-1960s the varactor-based parametric amplifier was introduced. This circuit offers low-noise performance in the microwave regime. It is based on a variable reactance diode which is embedded in a resonant circuit, where it is the capacitance of the varactor which is modulated in order to achieve gain. In optics there also exist parametrically driven systems. One example is the optical parametric oscillator which is based on the combination of a nonlinear optical crystal and an optical cavity. A strong laser beam is used to modulate the dielectric polarization of the crystal. This device is for instance used for the generation of nonclassical states of light.

An everyday classic example of parametric oscillation is a child on a swing. The swing acts as a pendulum, and its frequency depends on its length. If the child periodically stands up and kneels down, the frequency gets modulated. In this case the swing becomes a parametric oscillator. In order to amplify the swing’s motion, it is needed that the child stands up when the swing reaches its highest point and kneels down whenever the swing reaches its lowest position. This means that the frequency of the child’s periodic motion is twice



1. INTRODUCTION

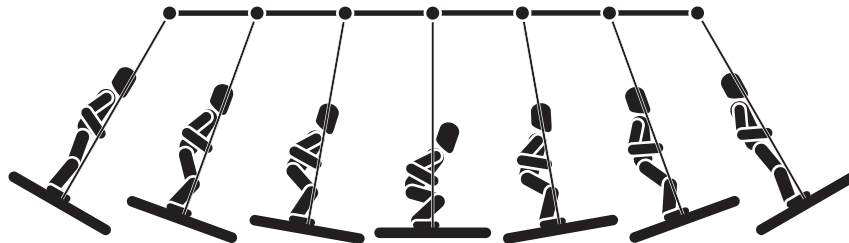


Figure 1.1: A child on a swing. The parametric oscillator is pumped by the periodic motion of a child standing up and kneeling down. To amplify the swing's motion the pumping motion has to be done in such a way that the frequency is twice the swing's oscillation frequency and that the child kneels down when the swing is at its lowest point and stands up when the swing reaches its highest point. The child can also deamplify the motion by doing the opposite.

the oscillation frequency of the swing.

This thesis is centered around a number of experiments where we have studied the interaction of such parametrically driven systems both with classical signals as well as with the quantum mechanical vacuum. The experiments are performed at very low temperatures and at microwave frequencies such that $k_B T \ll \hbar f$.

In the first part of the thesis we look at the parametric interaction with the vacuum. An interesting result of quantum theory is the existence of vacuum fluctuations. These fluctuations can be thought of as the continuous creation and annihilation of virtual particle-antiparticle pairs. Their momentary existence is allowed by the Heisenberg uncertainty principle, even though their creation and annihilation seems to violate the conservation of energy. The existence of these fluctuations was first thought of as just a theoretical curiosity, but has manifested itself in a number of observable effects such as spontaneous emission of excited atoms and the Lamb shift.¹² In 1970 it was predicted that the parametric interaction of a boundary condition (a perfect moving mirror) on the electromagnetic field and the vacuum could excite the virtual particle pairs into existence, provided that the boundary condition changed at relativistic speeds.^{13–15} This was later coined the dynamical Casimir effect.¹⁶

In Chapter 4 and in Paper A, I present the first experimental observation of this effect, where we measured the produced broadband radiation in a superconducting circuit where we modulated an electrical boundary condition, rather than a real moving mirror. The modulation was achieved by means of a superconducting quantum interference device (SQUID). We have also studied the statistical properties of the radiation.

In a second part of the thesis I present experiments where we studied parametric processes in another type of superconducting circuit. In this part we will look at the interaction between the device and externally applied signals. More specifically we will look at parametric amplification and intermode conversion. Parametric amplification in superconducting circuits has received

considerable interest in recent years because of their promise of quantum-limited noise performance. One possible implementation of such an amplifier involves a superconducting resonator where the resonance frequency is made tunable by embedding a variable inductance in the form of a SQUID in the resonator. These SQUID based parametric amplifiers have proven to be very successful. These devices have been used for quantum-limited measurements of nanomechanical resonators,¹⁷ readout schemes for superconducting qubits^{18–21} and quantum feedback,²² as well as for the generation and measurement of nonclassical states of light.²³ Intermode conversion is another possibility in these systems and has been used to put a single photon in a superposition of two different frequencies.²⁴ The effect has also been used for the parametric coupling between cavities and measurement lines.^{25,26}

In Chapter 4 and in Paper C, I present measurements on parametric amplification in a multimode superconducting resonator. I show that we can have gain in a number of different pumping schemes. When using a single mode, we pump the system at twice the mode frequency, whereas multimode amplification requires pumping at the sum frequency of two of the modes. I show that we were able to get gain in all different modes and that we reach quantum-limited noise performance. In Paper D, I present measurements where we used frequency conversion in order to couple different modes of the same resonator together. In this case the system is parametrically driven at the difference frequency between two of the modes. The coupling strength is proportional to the applied pump strength.

When a signal is applied to a parametric amplifier of half the pump frequency, the gain will depend on the phase relation between the signal and the applied pump. In terms of the child on the swing, we can understand this by contemplating what would happen if the child bends through the knees when the swing reaches the top, and stands up when the swing reaches the lowest point. In that case the swing will be parametrically damped, until fully at rest. The motion of the swing is deamplified. In Chapter 2 and Paper B, we present a model which describes the parametrically driven SQUID, where the signal is at half the pump frequency. The model introduces a new equivalent impedance called the pumpistor. The exact impedance will depend on the phase between the signal and the pump. The goal of the pumpistor is to provide a more intuitive circuit-based picture of parametric amplification using a SQUID. The more general case where the signal and pump are not related in frequency has been treated elsewhere.²⁷

The last experiment I present is a demonstration of an on-chip Mach-Zehnder interferometer. This type of interferometer is a well-known device in the field of optics. It is a device in which a signal is split using a beam splitter and fed into two different arms of the interferometer. At the other end of the device the arms are recombined. The phase difference between the two arms will then provide interference. These interferometers have been used, for instance, to generate entangled radiation.²⁸ In the experiments presented in Chapter 4 and Paper E, we have made an on-chip microwave interferometer.



1. INTRODUCTION

The phase difference between the arms stems from two SQUIDs embedded in the interferometer. We show that it is possible to get a significant reduction in the transmission through the device, depending on the phase difference across the SQUIDs.

The outline of the thesis is as follows: In Chapter 2, we introduce the theoretical background necessary to understand the results and the interpretation of the different experiments. The derivation of the pumpistor model is also included in this chapter. In Chapter 3 I describe the experimental techniques I used throughout my measurements. I discuss the working principle of cryostats and I give a detailed overview of the calibration methods used in Paper C in order to prove the quantum-limited performance of the parametric amplifier. In Chapter 4 I lift out the main findings of the different papers. I also include some unpublished results to provide a little more background to the appended papers. Finally in Chapter 5, I reiterate the main findings and provide an outlook for future measurements and possible improvements.

2

Theory

2.1 Superconducting Circuits

Superconductivity was discovered in 1911 shortly after Helium was liquefied for the first time. The discovery was made by Heike Kamerlingh Onnes when he noticed that mercury loses all electrical resistivity when it is cooled below a certain critical temperature.²⁹ Adding impurities to the mercury did not have any effect on the loss of resistance. The same effect was shortly after also observed in a number of different materials such as lead and tin.

It took another 46 years, until 1957, before the first microscopic theory for superconductivity was developed by Bardeen, Cooper and Schieffer.³⁰ This theory was called the BCS theory, and at the center of the theory is the assumption that there exists an attractive force between the electrons. This force is assumed to be mediated through the ion lattice, although the exact source is not important for the implications of such a force. The result is that electrons can overcome the Coulomb repulsion and pair up when the temperature drops below a critical temperature. Such pairs of electrons are called Cooper pairs and unlike single electrons these Cooper pairs are bosons.³¹ This means that there is no Pauli exclusion principle, and condensation of the Cooper pairs into a single quantum state is possible. This state is described by the wave function $\Psi = \sqrt{n_p} e^{i\theta}$, where θ denotes the superconducting phase and where the amplitude is defined such that $\Psi\Psi^* = n_p$ is the density of Cooper pairs.

2.1.1 The Josephson effect and SQUIDs

In 1962 B. Josephson theoretically predicted that a weak link between two superconductors can still sustain a supercurrent made up of Cooper pairs albeit one not as strong as the supercurrent in the bulk superconductors.³² In this work the weak links are formed by tunnel junctions, where two superconducting leads are separated by a thin insulating oxide barrier. They are referred to as



2. THEORY

Josephson junctions and are the main elements used in the superconducting circuits described and studied in this thesis. The leads must be close enough to each other such that the exponentially decaying wave function, describing the center of mass motion of the Cooper pairs in each superconductor, overlap. In this case the phase difference between the wave functions on each side of the junction, $\phi = \theta_1 - \theta_2$, will obey the following two relations:³²

$$V = \left(\frac{\hbar}{2e} \right) \frac{d\phi}{dt} = \left(\frac{\Phi_0}{2\pi} \right) \frac{\partial\phi}{\partial t} \quad (2.1)$$

$$I = I_c \sin(\phi), \quad (2.2)$$

where we introduced $\Phi_0 = h/2e$ as the magnetic flux quantum and I_c as the critical current. These two Josephson effects describe the relation between the voltage V and the phase across a junction (AC Josephson effect, Eq. (2.1)) on the one hand, and the current I through the junction and the phase difference across the junction (DC Josephson effect, Eq. (2.2)) on the other hand. If we have a constant phase ϕ across the junction, there will be a current given by Eq. (2.2), without developing a voltage. The maximum value of this so called supercurrent is $\pm I_c$. The critical current, I_c , of a Josephson junction can be related to the normal state resistance R_N of the junction with the Ambegaokar-Baratoff relation:^{33,34}

$$\begin{aligned} I_c &= \frac{\pi \Delta_{sc}(T)}{2eR_N} \tanh \left(\frac{\Delta_{sc}(T)}{2k_B T} \right) \\ &= \frac{\pi \Delta_{sc}(0)}{2eR_N}, \text{ for } T \approx 0, \end{aligned} \quad (2.3)$$

where $2\Delta_{sc}$ is the superconducting energy gap of the electrodes on either sides of the junction.

In reality the temperature is finite, such that there will also be some quasiparticle population in the superconductors. These quasiparticles can tunnel through the junction as well, giving rise to a resistance, which will be in parallel with the ideal Josephson junction. As the junction consists of superconducting leads, separated by only a thin oxide barrier, we also have to take into account the capacitance. The full combination is called the RCSJ-model, or the Resistively and Capacitively Shunted Junction model. It shows that if we current bias the junctions that the dynamics are the same as that of a particle confined to a tilted washboard potential, where the slope of the washboard is set by the bias current.³⁵

When we now assume a perfect Josephson element DC biased with a current $I_b = I_c \sin \phi_b < I_c$, and we allow for small fluctuations around this current,

we can derive the current-voltage relation as follows:

$$\frac{dI}{dt} = I_c \cos(\phi_b) \frac{d\phi}{dt} = I_c \cos(\phi_b) V \left(\frac{2\pi}{\Phi_0} \right) \quad (2.4)$$

$$V = \left(\frac{\Phi_0}{2\pi} \right) \frac{1}{I_c \cos(\phi_b)} \frac{dI}{dt} = L_J \frac{dI}{dt}, \quad (2.5)$$

$$\text{where } L_J = \left(\frac{\Phi_0}{2\pi} \right) \frac{1}{I_c \cos(\phi_b)}. \quad (2.6)$$

Here we have used Eqs. (2.1) and (2.2). We see that the ideal Josephson junction acts as an inductor with an inductance equal to L_J . This inductance is dependant on ϕ and thus on the bias current through the junction.

In all our experiments we use the Josephson junction in a SQUID geometry, a superconducting loop, intersected with two junctions, see Fig. 2.1. In such a geometry there will be a quantum interference between the supercurrents running through each junction, where the phase difference between the junction will be dependent on the magnetic flux. If we now take the line integral of the superconducting phase over a contour around the ring, it is easy to understand that the phase must have wrapped a multiple of 2π as we end up in the same point:

$$\oint \nabla\theta \cdot d\mathbf{l} = (\theta_B - \theta_A) + \int_B^C \nabla\theta \cdot d\mathbf{l} + (\theta_D - \theta_C) + \int_D^A \nabla\theta \cdot d\mathbf{l} = 2\pi n. \quad (2.7)$$

As we have chosen the contour to be deep within the superconducting material (where the supercurrent density is zero), we can use $\nabla\theta = -\frac{2e}{\hbar} \mathbf{A}$, where \mathbf{A} is the magnetic vector potential. In the presence of the magnetic vector potential, it is also necessary to redefine the phase difference across the junction as $\phi = \theta_1 - \theta_2 - \frac{2e}{\hbar} \int_1^2 \mathbf{A} \cdot d\mathbf{l}$, with the integral taken in the direction of the current. We can then rewrite Eq. (2.7) as follows:

$$\begin{aligned} 2\pi n &= -\phi_1 - \frac{2e}{\hbar} \int_A^B \mathbf{A} \cdot d\mathbf{l} - \frac{2e}{\hbar} \int_B^C \mathbf{A} \cdot d\mathbf{l} + \phi_2 - \frac{2e}{\hbar} \int_C^D \mathbf{A} \cdot d\mathbf{l} - \frac{2e}{\hbar} \int_D^A \mathbf{A} \cdot d\mathbf{l} \\ &= \phi_2 - \phi_1 - \frac{2e}{\hbar} \oint \mathbf{A} \cdot d\mathbf{l}. \end{aligned} \quad (2.8)$$

As the line integral of the magnetic vector potential around a closed contour equals the magnetic flux through that contour, and when ignoring the multiples of 2π , we get:

$$\phi_2 - \phi_1 = \frac{2\pi\Phi}{\Phi_0}. \quad (2.9)$$

The total current through the SQUID will now be the sum of the currents through each junction:

$$I_{\text{sq}} = I_{c,1} \sin \phi_1 + I_{c,1} \sin \phi_2. \quad (2.10)$$



2. THEORY

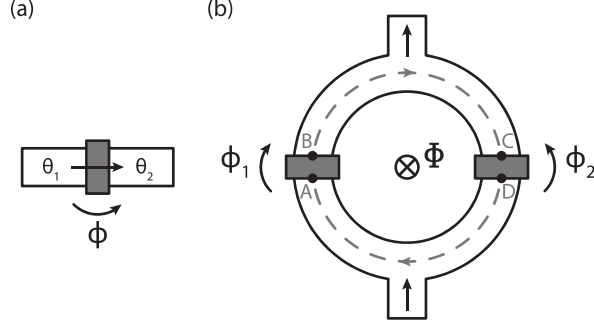


Figure 2.1: The SQUID consisting of two Josephson junctions in parallel. (a) The phase across the junction in the presence of a magnetic vector potential is defined as $\phi = \theta_1 - \theta_2 - \frac{2e}{\hbar} \int_1^2 \mathbf{A} \cdot d\mathbf{l}$. (b) If we integrate the superconducting phase θ around a contour deep inside the superconductor (dashed line), we find that there is a quantum interference between the supercurrent through each junction which is described by $\phi_2 - \phi_1 = \frac{2\pi\Phi}{\Phi_0}$.

We can rewrite this equation using Eq. (2.9):

$$\begin{aligned}
 I_{\text{sq}} &= I_{c,1} \sin \left(\phi_1 + \frac{\phi_2}{2} - \frac{\phi_2}{2} \right) + I_{c,1} \sin \left(\phi_2 + \frac{\phi_1}{2} - \frac{\phi_1}{2} \right) \\
 &= (I_{c,1} + I_{c,2}) \sin \left(\frac{\phi_1 + \phi_2}{2} \right) \cos \left(\frac{\phi_2 - \phi_1}{2} \right) \\
 &\quad - (I_{c,1} - I_{c,2}) \cos \left(\frac{\phi_1 + \phi_2}{2} \right) \sin \left(\frac{\phi_2 - \phi_1}{2} \right) \\
 &= (I_{c,1} + I_{c,2}) \sin \phi_s \cos \frac{\pi\Phi}{\Phi_0} - (I_{c,1} - I_{c,2}) \cos \phi_s \sin \frac{\pi\Phi}{\Phi_0}, \quad (2.11)
 \end{aligned}$$

where we have introduced $\phi_s = \frac{\phi_1 + \phi_2}{2}$ as the phase difference across the SQUID. When we maximize this with respect to the phase ϕ_s we see that the critical current of the SQUID is:

$$I_{c,\text{sq}}(\Phi) = \sqrt{(I_{c,1} - I_{c,2})^2 + 4I_{c,1}I_{c,2} \cos^2 \left(\frac{\pi\Phi}{\Phi_0} \right)}. \quad (2.12)$$

For a symmetric SQUID ($I_{c,1} = I_{c,2} = I_c$), Eq. (2.12) reduces to:

$$I_{c,\text{sq}}(\Phi) = 2I_c \left| \cos \left(\frac{\pi\Phi}{\Phi_0} \right) \right|. \quad (2.13)$$

We can then rewrite Eq. (2.11) as:

$$I_{\text{sq}}(\Phi, \phi_s) = 2I_c \left| \cos \left(\frac{\pi\Phi}{\Phi_0} \right) \right| \sin \phi_s. \quad (2.14)$$

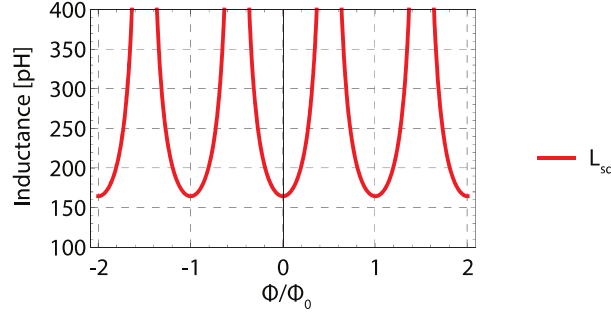


Figure 2.2: The SQUID inductance is plotted versus external magnetic flux for a Josephson junction with critical current $I_c = 1 \mu\text{A}$. The inductance is periodic with magnetic flux and diverges at $\Phi = (n + \frac{1}{2})\Phi_0$, n being an integer. Note that this is in the small signal limit, $\phi_s \ll \pi$.

We can see that the SQUID acts as a single Josephson junction where the critical current is controlled by the magnetic flux threading its loop. The Josephson inductance of the SQUID becomes:

$$\begin{aligned} L_{\text{sq}}(\Phi, \phi_s) &= \left(\frac{\Phi_0}{2\pi} \right) \frac{1}{2I_c \left| \cos\left(\frac{\pi\Phi}{\Phi_0}\right) \right| \cos(\phi_s)} \\ &= \frac{L_{\text{sq},0}}{\left| \cos\left(\frac{\pi\Phi}{\Phi_0}\right) \right| \cos(\phi_s)} \end{aligned} \quad (2.15)$$

with $L_{\text{sq},0} = \left(\frac{\Phi_0}{2\pi} \right) \frac{1}{2I_c}$. I have plotted the SQUID inductance in Fig. 2.2 for the small signal limit ($\phi_s = 0$).

2.1.2 Resonator

The resonators used in this work are distributed circuits. They consist of a $\lambda/4$ coplanar waveguide (CPW) resonator. This circuit will have several resonances and at frequencies close to a resonance frequency we can model the circuit as a lumped element circuit. In this section I will derive an expression for the reflection coefficient of the lumped element resonator and I will examine the different coupling regimes for the resonator.

The resonator is modeled as the lumped element circuit presented in Fig. 2.3(b). The lumped element parameters are coupled to the CPW param-



2. THEORY

ters as follows:

$$C_r = \frac{C_0 d}{2} \quad (2.16)$$

$$L_r = \frac{8L_0 d}{\pi^2} \quad (2.17)$$

$$R_r = \frac{Z_{\text{CPW}}}{\alpha_0 d}, \quad (2.18)$$

where C_0 and L_0 are the capacitance and inductance per unit length, $Z_{\text{CPW}} = \sqrt{L_0/C_0}$ is the characteristic impedance of the CPW, α_0 describes the losses per unit length, and d is the length of the resonator, see Fig. 2.3(a).³⁶ The internal loss in the resonator is represented with the real impedance R_r . This will give rise to the internal quality factor, Q^i . The coupling to the measurement line, which has an impedance of Z_0 , leads to the external quality factor, Q^e . Close to the resonance frequency we can rewrite the model such that Z_0 and C_c get rearranged into the new circuit elements, \widetilde{Z}_0 and \widetilde{C}_c , in parallel with the rest of the circuit, see Fig. 2.3(c). These elements can be expressed in terms of the coupling capacitor C_c and the impedance of the measurement line $Z_0 \approx 50 \Omega$ when we are close to resonance as:³⁷

$$\widetilde{C}_c = \frac{C_c}{1 + \omega_0^2 C_c^2 Z_0^2} \approx C_c \quad (2.19)$$

$$\widetilde{Z}_0 = \frac{1 + \omega_0^2 C_c^2 Z_0^2}{\omega_0^2 C_c^2 Z_0} \approx \frac{1}{\omega_0^2 C_c^2 Z_0}, \quad (2.20)$$

where the approximations assumes that $\omega_0 Z_0 C_c \ll 1$, which is the case for our resonators close to the resonance frequency. As $\widetilde{C}_c = C_c$ ends up in parallel with C_r , we have used that the angular resonance frequency $\omega_0 = 1/\sqrt{L_r C_{\text{tot}}} = 1/\sqrt{L_r (C_r + C_c)}$. The quality factors are then:³⁸

$$Q^i = \omega_0 R_r C_{\text{tot}} = \omega_0 R_r (C_r + C_c) = \frac{R_r}{\sqrt{L_r / (C_r + C_c)}} \quad (2.21)$$

$$Q^e = \omega_0 \widetilde{Z}_0 C_{\text{tot}} = \frac{(C_r + C_c)}{\omega_0 Z_0 C_c^2} = \left(\frac{C_r + C_c}{C_c} \right)^2 \frac{\sqrt{L_r / (C_r + C_c)}}{Z_0} \quad (2.22)$$

The total quality factor is then defined as $1/Q = 1/Q^i + 1/Q^e$.

The response of the circuit is represented by the reflection coefficient Γ which is defined as follows:³⁸

$$\Gamma = \frac{V^-}{V^+} = \frac{Z_r - Z_0}{Z_r + Z_0}, \quad (2.23)$$

where V^- and V^+ are the outgoing and incoming voltages respectively. From

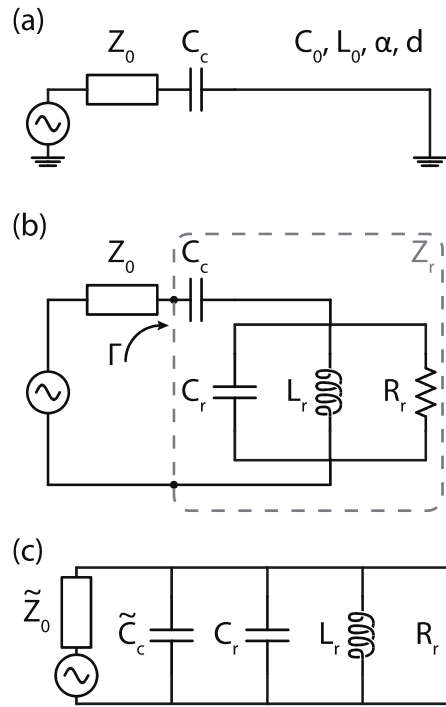


Figure 2.3: (a) Circuit model for a quarter-wavelength CPW transmission line resonator. (b) Circuit model for a lumped element resonator. (c) Equivalent circuit close to the resonance frequency.



2. THEORY

Fig. 2.3 we can derive the resonator impedance as:

$$\begin{aligned} Z_r &= \frac{1}{i\omega C_c} + \frac{1}{\frac{1}{R_r} + \frac{1}{i\omega L_r} + i\omega C_r} \\ &= \frac{1 - \omega^2 L_r (C_r + C_c) + i\omega \frac{L_r}{R_r}}{i\omega C_c (1 - \omega^2 L_r C_r) - \omega^2 C_c \frac{L_r}{R_r}}. \end{aligned} \quad (2.24)$$

We can now substitute Eq. (2.24) into Eq. (2.23). We also use the definitions for the internal and external quality factors, see Eqs. (2.21) and (2.22), and the resonance frequency:

$$\begin{aligned} \Gamma &= \frac{1 - \omega^2 L_r (C_r + C_c (1 + \frac{Z_0}{R_r})) + i\omega (\frac{L_r}{R_r} - Z_0 C_c (1 - \omega^2 L_r C_r))}{1 - \omega^2 L_r (C_r + C_c (1 - \frac{Z_0}{R_r})) + i\omega (\frac{L_r}{R_r} + Z_0 C_c (1 - \omega^2 L_r C_r))} \\ &= \frac{1 - (\frac{\omega}{\omega_0})^2 + i\frac{\omega}{\omega_0} \left(\frac{1}{Q^i} - \frac{1}{Q^e} \left(\frac{C_r + C_c - C_r (\frac{\omega}{\omega_0})^2}{C_c} \right) \right)}{1 - (\frac{\omega}{\omega_0})^2 + i\frac{\omega}{\omega_0} \left(\frac{1}{Q^i} + \frac{1}{Q^e} \left(\frac{C_r + C_c - C_r (\frac{\omega}{\omega_0})^2}{C_c} \right) \right)}, \end{aligned} \quad (2.25)$$

where we used that $R_r \gg Z_0$. We now rewrite the expression for a small detuning from the resonance frequency, $\omega = \omega_0 + \delta\omega$, with $\delta\omega \ll \omega$:

$$\begin{aligned} \Gamma &= \frac{\delta\omega - i \left(\frac{\omega_0}{2Q^i} - \frac{\omega_0}{2Q^e} + \frac{C_r \delta\omega}{C_c Q^e} \right) - i \left(\frac{\delta\omega}{2Q^i} - \frac{\delta\omega}{2Q^e} + \frac{C_r \delta\omega^2}{C_c Q^e \omega_0} \right)}{\delta\omega - i \left(\frac{\omega_0}{2Q^i} + \frac{\omega_0}{2Q^e} - \frac{C_r \delta\omega}{C_c Q^e} \right) - i \left(\frac{\delta\omega}{2Q^i} + \frac{\delta\omega}{2Q^e} - \frac{C_r \delta\omega^2}{C_c Q^e \omega_0} \right)} \\ &\approx \frac{\delta\omega - i \left(\frac{\omega_0}{2Q^i} - \frac{\omega_0}{2Q^e} \right)}{\delta\omega - i \left(\frac{\omega_0}{2Q^i} + \frac{\omega_0}{2Q^e} \right)} = \frac{\frac{2\delta\omega}{\omega_0} - i \left(\frac{1}{Q^i} - \frac{1}{Q^e} \right)}{\frac{2\delta\omega}{\omega_0} - i \left(\frac{1}{Q^i} + \frac{1}{Q^e} \right)} \end{aligned} \quad (2.26)$$

We can use Eq. (2.26) to fit the magnitude and the phase and three different regimes can be recognized, see Fig. 2.4. When $Q^e > Q^i$ the loss rate in the resonator due to loss is larger than the coupling rate to the measurement line. However, when $Q^e = Q^i$, we have the so-called critically coupled regime. When this occurs the magnitude of the reflection coefficient drops to zero. Finally when $Q^e < Q^i$ we are in the overcoupled regime, meaning that the internal losses are smaller than the coupling to the measurement line. This regime is marked by the phase of the reflection coefficients which wraps a full 2π on resonance and there is only a small magnitude response.

2.1.3 Multimode coplanar waveguide resonator

In the previous section I analyzed the microwave response of a lumped element resonator. This is an approximation for the response around resonance of the coplanar waveguide resonators discussed in this thesis. Such a resonator

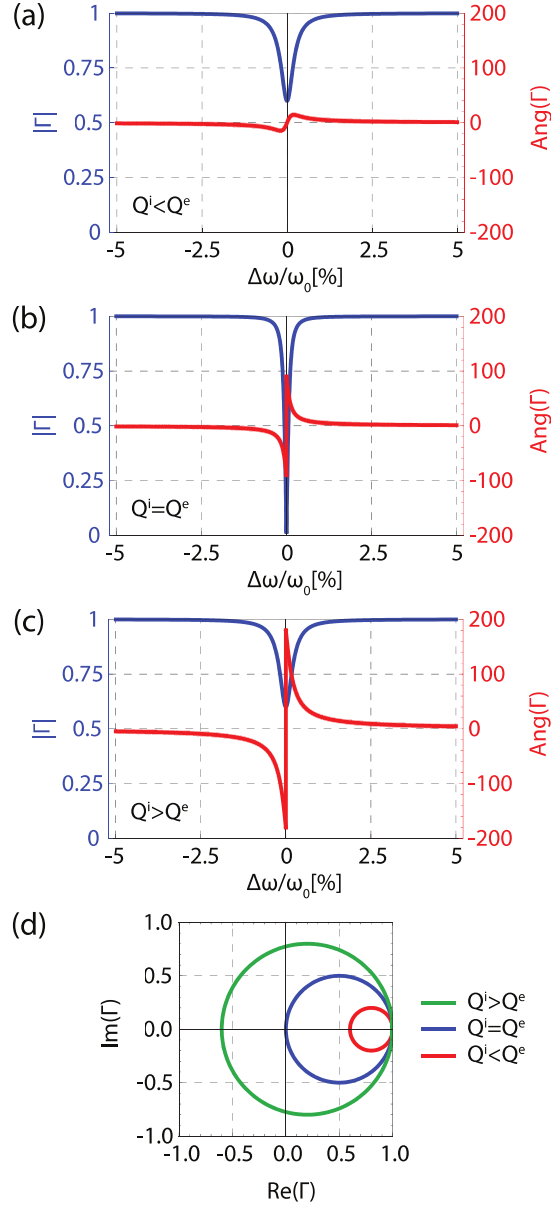


Figure 2.4: The reflection coefficient Γ for the different coupling regimes. (a) The undercoupled regime, $Q^i < Q^e$. (b) The critically coupled resonator $Q^i = Q^e$. Notice that the magnitude reaches down to zero at resonance. (c) The overcoupled regime $Q^i > Q^e$. In this regime the phase of Γ wraps 360° on resonance. (d) Γ plotted in the complex plane. When the resonator is overcoupled, Γ will encircle the origin.



2. THEORY

basically consist of a coplanar waveguide (CPW) coupled to the measurement setup through a coupling capacitor and terminated to ground at the other end by means of a SQUID. Such a SQUID acts as a flux-tunable inductor, as we discussed before, which will allow for frequency tuning of the resonator. As the resonator is grounded in one end and open in the other, it is a $\lambda/4$ -resonator. There will however be additional resonances at approximately all the odd multiples of this first mode. In this section I will derive an expression for the spectrum of the resonator, starting out from the Lagrangian of the circuit.

We give a representation of the $\lambda/4$ CPW resonator in Fig. 2.5. Using this representation and following the derivations found in Bourassa *et al.*³⁹ and Wallquist *et al.*⁴⁰, we start by writing down the Lagrangians for the different parts of the circuit. The Lagrangian for the coupling capacitor at position $x = 0$ is given by:

$$\mathcal{L}_{C_c} = \frac{C_c}{2} [\dot{\psi}(0, t) - V_0(t)]^2, \quad (2.27)$$

where we introduce the flux notation $\psi(x, t) = \int_{-\infty}^t V(x, t) dt$. C_c is the coupling capacitance and $V_0(t)$ is the voltage to the right of the coupling capacitance. The Lagrangian for the SQUID at position $x = d$ is given by:

$$\begin{aligned} \mathcal{L}_{\text{sq}} &= \frac{C_{\text{sq}}}{2} \dot{\psi}^2(d, t) + \frac{1}{L_{\text{sq}}(\Phi)} \left(\frac{\Phi_0}{2\pi} \right)^2 \cos \left(\frac{2\pi\psi(d, t)}{\Phi_0} \right) \\ &= \frac{C_{\text{sq}}}{2} \dot{\psi}^2(d, t) + \frac{1}{L_{\text{sq}}(\Phi)} \left(\frac{\Phi_0}{2\pi} \right)^2 \left[1 - \left(\frac{2\pi}{\Phi_0} \right)^2 \frac{\psi^2(d, t)}{2} + \right. \\ &\quad \left. \sum_{n=2}^{\infty} (-1)^n \frac{\left(\frac{2\pi\psi(d, t)}{\Phi_0} \right)^{2n}}{(2n)!} \right] \\ &\approx \frac{C_{\text{sq}}}{2} \dot{\psi}^2(d, t) - \frac{\psi^2(d, t)}{2L_{\text{sq}}(\Phi)}, \end{aligned} \quad (2.28)$$

where we Taylor expanded the cosine and neglected the higher order nonlinearities and the constant term (as the latter does not add to the dynamics). In this equation C_{sq} is the SQUID capacitance and $L_{\text{sq}}(\Phi)$, assuming the small signal limit ($\phi_s = 0$ in Eq. (2.15)), is the SQUID inductance, which depends on the external magnetic flux Φ .

Finally the Lagrangian for the CPW is given by:

$$\mathcal{L}_{\text{CPW}} = \int_0^d \left[\frac{C_0}{2} \dot{\psi}^2(x, t) - \frac{[\partial_x \psi(x, t)]^2}{2L_0} \right] dx, \quad (2.29)$$

where C_0 and L_0 are the capacitance and inductance per unit length. The CPW is superconducting and therefore we model it as a lossless transmission line. The total Lagrangian is then simply:

$$\mathcal{L}_{\text{tot}} = \mathcal{L}_{C_c} + \mathcal{L}_{\text{CPW}} + \mathcal{L}_{\text{sq}}. \quad (2.30)$$

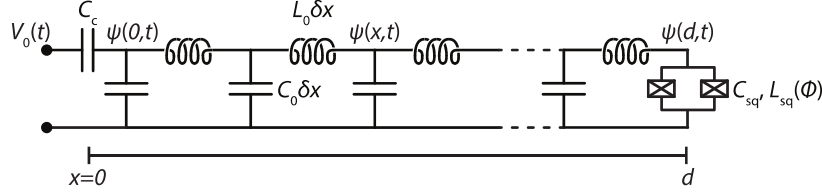


Figure 2.5: The $\lambda/4$ coplanar waveguide resonator. The circuit consists of a CPW, modeled by a distributed network of capacitors $C_0\delta x$ and inductors $L_0\delta x$, terminated to ground with a SQUID at position $x = d$. The SQUID has a capacitance C_{sq} and a flux-dependent inductance $L_{sq}(\Phi)$. The coupling capacitor C_c is found at position $x = 0$ and couples the CPW to the transmission line. The voltage at the input is $V_0(t)$.

As we are now interested in the normal modes of the resonator, we have to solve the Euler-Lagrange equation of motion:

$$\sum_{\nu=x,t} \partial_\nu \left(\frac{\partial \mathcal{L}_{\text{tot}}}{\partial [\partial_\nu \psi(x,t)]} \right) - \frac{\partial \mathcal{L}_{\text{tot}}}{\partial \psi(x,t)} = 0. \quad (2.31)$$

In the middle of the resonator Eq. (2.31) reduces to the standard wave equation:

$$\ddot{\psi}(x,t) = v_p^2 \partial_{xx} \psi(x,t), \quad (2.32)$$

which has a solution which is composed of traveling modes and is of the form:

$$\psi(x,t) = \sum_m \psi_m(t) u_m(x). \quad (2.33)$$

Note that $v_p = 1/\sqrt{L_0 C_0}$ is the phase velocity of the waves in the CPW. At the ends of the resonator, $x = 0, d$, we have the following boundary conditions:

$$C_c \ddot{\psi}(x,t)|_{x=0} - C_c \dot{V}_0(t) - \frac{1}{L_0} \partial_x (\psi(x,t))|_{x=0} = 0 \quad (2.34)$$

$$2 \frac{C_{sq}}{2} \ddot{\psi}(x,t)|_{x=d} + \frac{1}{L_{sq}(\Phi)} \psi(d,t) + \frac{1}{L_0} \partial_x (\psi(x,t))|_{x=d} = 0 \quad (2.35)$$

We postulate that the mode envelope function $u_m(x)$ is of the form:

$$u_m(x) = A_m \sin(k_m x - \phi_m), \quad (2.36)$$

where A_m is a mode-dependent normalization factor, $k_m = \omega_m/v_p$ is the angular wave number of mode m , with ω_m the angular resonance frequency, and ϕ_m is the phase factor, which we can determine by substituting Eq. (2.33)



2. THEORY

into Eq. (2.34) and looking at the stationary solution ($\dot{V}_0(t) = 0$):

$$\begin{aligned}
 C_c v_p^2 A_m k_m^2 \sin \phi_m &= \frac{A_m k_m \cos \phi_m}{L_0} \\
 \tan \phi_m &= \frac{1}{C_c v_p^2 L_0 k_m} \\
 &= \frac{1}{\omega_m C_c} \\
 &= \frac{1}{\sqrt{\frac{L_0}{C_0}}} \\
 &= \left| \frac{Z_{C_c}}{Z_{\text{CPW}}} \right|, \tag{2.37}
 \end{aligned}$$

where $Z_{C_c} = 1/(i\omega_m C_c)$ is the impedance of the coupling capacitor and $Z_{\text{CPW}} = \sqrt{L_0/C_0}$ is the characteristic impedance of the (lossless) CPW.³⁸ Note that $|Z_{C_c}| \gg |Z_{\text{CPW}}|$ such that $\phi_m \approx \pi/2$. We can now go to the dispersion equation for the cavity modes f_m by inserting Eq. (2.33) into Eq. (2.35):

$$\begin{aligned}
 -\frac{A_m k_m \cos(k_m d - \phi_m)}{L_0} &= \left[-C_{\text{sq}} v_p^2 A_m k_m^2 + \frac{A_m}{L_{\text{sq}}(\Phi)} \right] \sin(k_m d - \phi_m) \\
 -k_m d \cot(k_m d - \phi_m) &= -\frac{C_{\text{sq}}}{C_0 d} (k_m d)^2 + \frac{L_0 d}{L_{\text{sq}}(\Phi)} \\
 k_m d \tan(k_m d) &= -\frac{C_{\text{sq}}}{C_0 d} (k_m d)^2 + \frac{L_0 d}{L_{\text{sq}}(\Phi)}, \text{ with } \phi_m = \frac{\pi}{2} \\
 \frac{\pi f_m}{2 f_R} \tan\left(\frac{\pi f_m}{2 f_R}\right) &= -\frac{C_{\text{sq}}}{C_0 d} \left(\frac{\pi f_m}{2 f_R}\right)^2 + \left| \cos\left(\frac{\pi \Phi}{\Phi_0}\right) \right| \frac{L_0 d}{L_{\text{sq},0}}, \tag{2.38}
 \end{aligned}$$

where $f_R = \omega_R/(2\pi)$ is the bare resonator frequency and $C_0 d$ and $L_0 d$ are the total resonator capacitance and inductance, respectively. Note that we explicitly broke out the flux dependence from the SQUID inductance. We also used that $k_m d = \pi \omega_m/(2\omega_R) = \pi f_m/2f_R$.

Eq. (2.38) is a transcendental equation which cannot be solved analytically. The graphical solution to Eq. (2.38) as well as the mode spectrum $f_m(\Phi)$ as a function of magnetic flux is given in Fig. 2.6(a). The first mode $f_0(0)$ will be approximately found at $f_R/(1 + \gamma_0/|\cos(\pi\Phi/\Phi_0)|)$, with $\gamma_0 = L_{\text{sq},0}/L_0 d$ the inductance participation ratio at zero flux, because of the small squid capacitance and inductance compared to the resonator capacitance and inductance. The first mode will tune to zero, when $\Phi = \Phi_0/2$. The higher modes are found at approximately $f_m(0) \approx (2m+1)f_0(0)$ and they tune down to $f_m(\Phi_0/2) \approx (2m)f_0(0)$. This is also visible in the mode envelopes, which are presented for the first three modes in Fig. 2.6(b).

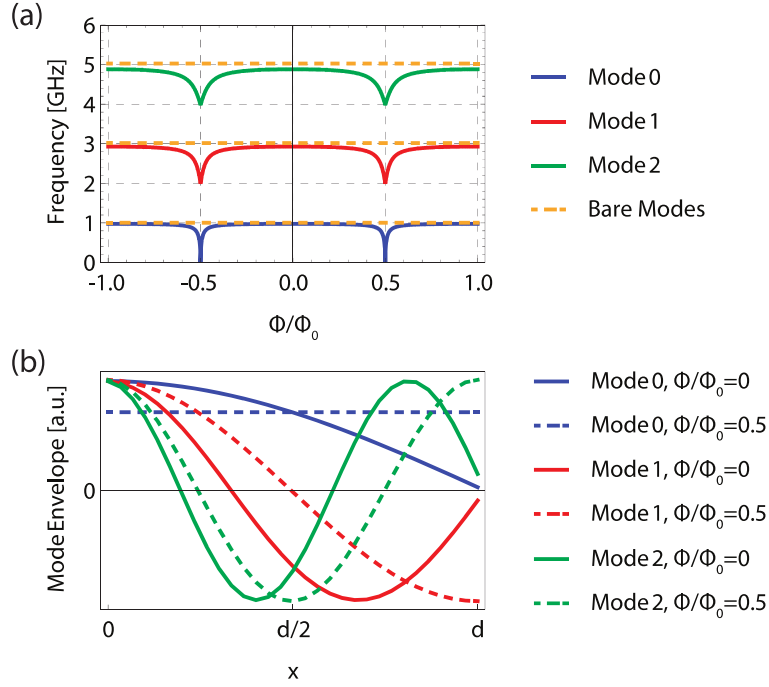


Figure 2.6: *The multimode resonator. (a) The frequency of the first three modes of a $\lambda/4$ CPW resonator terminated to ground with an ideal SQUID as a function of the normalized magnetic flux Φ/Φ_0 threading the SQUID. In this specific example the bare resonator (neglecting the SQUID) has a fundamental mode at 1 GHz. The first three (equidistant) modes of the bare resonator are denoted with the orange dashed lines. Introducing the SQUID will introduce flux-tunability and make the spectrum nonequidistant. The inductance participation ratio of SQUID $\gamma_0 = L_{\text{sq},0}/L_0 d = 2\%$ and its capacitance participation ratio can be neglected, which is typical for our devices. The modes will tune from approximately $f_m(0) \approx (2m+1)f_0(0)$ at $\Phi/\Phi_0 = 0$ down to $f_m(\Phi_0/2) \approx (2m)f_0(0)$ at $\Phi/\Phi_0 = 0.5$. (b) The mode envelopes of the first three modes of the resonator for two different flux values. The coupling capacitor is found at $x = 0$ and the SQUID at $x = d$. We see that the envelope does not quite reach zero at $x = d$, which is due to the phase across the ideal SQUID. When tuning the flux to $\Phi/\Phi_0 = 0.5$, the SQUID inductance becomes infinite, meaning that it will essentially act as an open.*



2.2 Parametric Amplification

In this section we will look at the effect of modulating the SQUID inductance periodically. The modulation is achieved by coupling an AC magnetic flux pump, through the SQUID loop by means of an inductively coupled CPW in the vicinity of the SQUID, so-called flux pumping. Such an amplifier which uses a parametrically modulated SQUID is called a Josephson Parametric amplifier (JPA). Note that it is also possible to modulate the SQUID using the bias current through the SQUID, so-called current pumping, but this case will not be treated in this thesis. It is possible to achieve parametric amplification, when the frequency of the pump matches one of the resonance conditions in the circuit. We can recognize two different cases for which we get amplification: i) The case where the pump is at twice a mode frequency, so called single-mode amplification, where any signal, in the vicinity of the mode being pump, will get amplified, $f_p \approx 2 \times f_m$, ii) the multimode case, where the pump equals the sum of two different modes, $f_p \approx f_m + f_n$. In this case any signal which falls in one of the pumped modes will be amplified.

The parametric amplification process will not only amplify a signal, but also generate an idler, symmetrically around half the pump frequency, with respect to the signal. For the multimode case, this means that if the signal $f_s \approx f_m$, that the idler will appear in the other mode, $f_i \approx f_n$. In the single-mode case however both the idler and the signal will appear in the same mode $f_s \approx f_m \approx f_i$. Both of these processes involve three photons: a pump photon, a signal photon and an idler photon, and are thus called three-wave mixing processes. This has to be compared to four-wave mixing processes, involving two pump photons, a signal photon and an idler photon. The current-pumped JPA is an example of this.

When the signal occurs at exactly half the pump frequency then the idler will occur at that same frequency, $f_s = f_p/2 = f_i$. The signal and idler will then interfere, where the interference condition is dependent on the pump phase. This is so called phase-sensitive amplification (also called degenerate amplification). However, when the signal is detuned from half the pump frequency, $f_s \neq f_p/2 \neq f_i$, then the idler can not interfere, which means that the gain is phase-insensitive. This is so called nondegenerate amplification. Note that the multimode case always provides nondegenerate amplification. The minimally added noise, expressed in photon number, in this case will follow the quantum limit:⁴¹

$$N_{\text{QL}} = \frac{1}{2} \left| 1 - \frac{1}{G} \right|, \quad (2.39)$$

where G is the gain of the parametric amplifier. This will tend to 0.5 added noise photons when G goes to infinity. In the degenerate case however the signal and the idler interfere to provide quadrature-dependent gain. This will amplify one of the quadratures and deamplify the other one with the same amount. Whichever quadrature is being amplified can be chosen by rotating

| | Three-wave mixing | Four-wave mixing |
|---|--|--|
| Degenerate amplification (phase-sensitive) | $f_p = f_s + f_i, f_s = f_i$ $f_p = 2f_s$ | $2f_p = f_s + f_i, f_s = f_i$ $f_p = f_s$ |
| Nondegenerate amplification (phase-insensitive) | $f_p = f_s + f_i, f_s \neq f_i$ | $2f_p = f_s + f_i, f_s \neq f_i$ |

Table 2.1: Comparing different ways of categorizing parametric amplification. In three-wave mixing the signal and idler frequency add up to the pump frequency. When the signal is at exactly half the pump frequency (degenerate amplification), signal and idler will have the same frequency allowing them to interfere. This gives phase-sensitive amplification. When the signal is not at half the pump frequency, the idler ends up at a different frequency (nondegenerate amplification). In the four-wave mixing case, the pump frequency is at half the sum of the signal and idler frequencies. Degenerate amplification will in this case be problematic as signal, idler and pump would all have the same frequency.

the phase between the signal and the pump. This regime allows for noiseless amplification. We give an overview of the different regimes in Fig. 2.7. We have also made a table, categorizing parametric amplification according to their properties, see Table 2.1.

In the following two sections I will discuss the pumpistor model, presented in Paper B, and a more general theory for parametric amplification. The pumpistor provides a linearized circuit model for the flux-pumped SQUID, providing an intuitive insight in terms of circuit analysis. In this thesis we will derive the degenerate phase-sensitive operation scheme, but the pumpistor model has been extended to the more general nondegenerate cases as well.²⁷ The more general theory will start from the equations of motion for the amplitudes of the field in the resonator and we will derive expressions for the gain for both the single-mode nondegenerate case and the multimode case.

2.2.1 Pumpistor

The goal of the pumpistor is to provide an analysis of the flux-pumped SQUID in terms of an equivalent set of circuit elements. In this section we specifically look at degenerate, phase-sensitive, parametric amplification, where the signal is at exactly half the pump frequency so that the idler occurs at the same frequency as the signal. As we saw before in Eq. (2.15), we know that the SQUID acts as a nonlinear, tunable inductance. The inductance is flux-modulated around a DC value Φ_{DC} with an AC-flux pump Φ_{AC} , coupled into the SQUID loop by means of a mutual inductance to a microwave line nearby. In this case the SQUID can be separated into the standard Josephson inductance, in parallel to a phase-sensitive impedance. The derivation follows



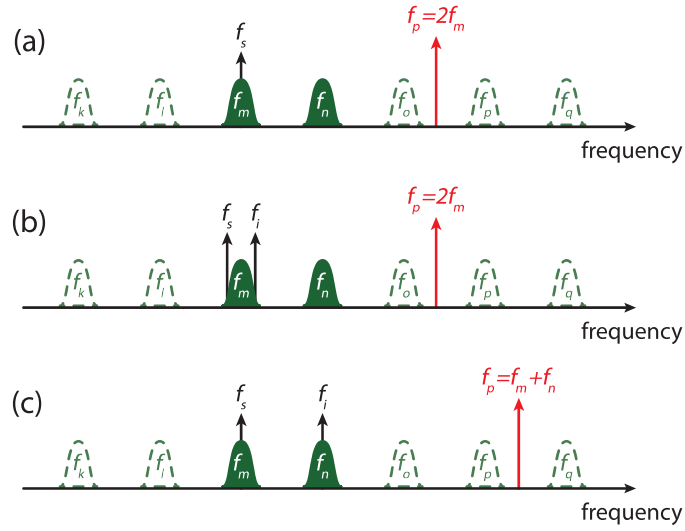


Figure 2.7: The different flux-pumped parametric amplification regimes. (a) Degenerate phase-sensitive parametric amplification, where $f_p \approx 2 \times f_m$ and $f_s = f_p/2 = f_i$, we discuss this in Section 2.2.1. In this case the signal and idler interfere and the gain is quadrature-dependent. (b) Nondegenerate single-mode parametric amplification, with $f_p \approx 2 \times f_m$ and $f_s \neq f_i$. This is discussed in Section 2.2.2. (c) Nondegenerate multimode parametric amplification, where $f_p = f_m + f_n$. Any signal in mode m , $f_s \approx f_m$, will be amplified and the idler will end up in mode n , $f_i \approx f_n$, or vice versa, see Section 2.2.2.

the one found in Paper B. We start by writing the equation for the current of the symmetric SQUID, see Eq. (2.14), where we now insert the time-dependent flux $\Phi(t) = \Phi_{\text{DC}} + \Phi_{\text{AC}} \cos(\omega_{\text{p}}t + \theta_{\text{p}})$:

$$I_{\text{sq}} = I_{\text{c,sq}} \underbrace{\left| \cos \left(\frac{\pi [\Phi_{\text{DC}} + \Phi_{\text{AC}} \cos(\omega_{\text{p}}t + \theta_{\text{p}})]}{\Phi_0} \right) \right|}_{\text{flux term}} \underbrace{\sin(\phi_{\text{s}}(t))}_{\text{phase term}}. \quad (2.40)$$

We can now Taylor expand the flux term around Φ_{DC} which leads to:

$$I_{\text{c,sq}} \left| \cos \left(\frac{\pi \Phi_{\text{p}}(t)}{\Phi_0} \right) \right| \approx I_{\text{c,sq}} \cos(F) - I_{\text{c,sq}} \sin(F) \delta f \cos(\omega_{\text{p}}t + \theta_{\text{p}}), \quad (2.41)$$

where $I_{\text{c,sq}} = 2I_{\text{c}}$ is the SQUID critical current at zero DC flux. We also introduced the normalized DC flux, $F = \pi\Phi_{\text{DC}}/\Phi_0$, and AC flux amplitude, $\delta f = \pi\Phi_{\text{AC}}/\Phi_0$. In a next step we assume the phase to be of the form $\phi_{\text{s}}(t) = \phi_{\text{s}} \cos(\omega_{\text{s}}t + \theta_{\text{s}})$. We can insert this into the phase term of Eq. (2.40) and perform a Fourier-Bessel expansion:⁴²

$$\sin(\phi_{\text{s}} \cos(\omega_{\text{s}}t + \theta_{\text{s}})) = 2 \sum_{n=0}^{\infty} (-1)^n J_{2n+1}(\phi_{\text{s}}) \cos[(2n+1)(\omega_{\text{s}}t + \theta_{\text{s}})], \quad (2.42)$$

where $J_n(\phi_{\text{s}})$ is the Bessel function of the first kind. We can now multiply Eqs. (2.41) and (2.42) and get an approximation for the current through the SQUID. We see that there are frequency mixing terms in the equation for the SQUID current, and we only keep the terms $I_{\omega_{\text{s}}}$ at the signal frequency $\omega_{\text{s}} = \omega_{\text{p}}/2$. The voltage across the SQUID and at the signal frequency, $V_{\omega_{\text{s}}}$, is calculated by inserting $\phi_{\text{s}}(t)$ into the AC Josephson relation, see Eq. (2.1), and only keeping the terms at the (positive) signal frequency, $e^{+i\omega_{\text{s}}t}$. We can then calculate the SQUID inductance at the signal frequency as:

$$\begin{aligned} L_{\omega_{\text{s}}} &= \frac{V_{\omega_{\text{s}}}}{i\omega_{\text{s}}I_{\omega_{\text{s}}}} \\ &= \frac{(\Phi_0/2\pi I_{\text{c,sq}}) \phi_{\text{s}}}{2J_1(\phi_{\text{s}}) \cos(F) + \delta f \sin(F) (-J_1(\phi_{\text{s}}) e^{i(\theta_{\text{p}}-2\theta_{\text{s}})} + J_3(\phi_{\text{s}}) e^{i(-\theta_{\text{p}}+2\theta_{\text{s}})})}. \end{aligned} \quad (2.43)$$

$L_{\omega_{\text{s}}}$ can be thought of as two inductive elements in parallel, see Fig. 2.8(a), which are grouped by their DC-flux dependence:

$$\frac{1}{L_{\omega_{\text{s}}}} = \frac{1}{L_{\text{sq}}} + \frac{1}{L_{\text{p}}}, \quad (2.44)$$

where Josephson inductance, L_{sq} , groups the terms with a $\cos(F)$ dependence:

$$\frac{1}{L_{\text{sq}}} = \frac{2J_1(\phi_{\text{s}}) \cos(F)}{L_{\text{sq},0} \phi_{\text{s}}}, \quad (2.45)$$



2. THEORY

and where a new effective element called the pumpistor, L_P , groups the terms with a $\sin(F)$ dependence:

$$\frac{1}{L_P} = \frac{\delta f \sin(F) (-J_1(\phi_s) e^{i(\theta_p - 2\theta_s)} + J_3(\phi_s) e^{i(-\theta_p + 2\theta_s)})}{L_{sq,0} \phi_s}, \quad (2.46)$$

where we defined $L_{sq,0}$ as in Eq. (2.15). We can now introduce the phase difference $\Delta\theta = 2\theta_s - \theta_p$ and we get:

$$L_{sq} = \frac{L_{sq,0}}{\cos(F)} \left[\frac{\phi_s}{2J_1(\phi_s)} \right] \quad (2.47)$$

$$L_P = \frac{e^{i\Delta\theta}}{\delta f \sin(F)} \frac{L_{sq,0}}{\left[J_3(\phi_s) e^{i2\Delta\theta} - J_1(\phi_s) \right]}. \quad (2.48)$$

The inductance Eq. (2.47) reduces to the ordinary Josephson inductance, Eq. (2.15), in the small signal limit. The pumpistor element, Eq. (2.48), shows some interesting properties. The impedance of this element for a given pump strength δf will change with the phase difference $\Delta\theta$. We have plotted $\text{Re}[L_P]$ and $\text{Im}[L_P]$ as a function of $\Delta\theta$ in Fig. 2.8(b). For comparison we also plotted L_{sq} . For $\Delta\theta = 0$, L_P will be negative and real, however when $\Delta\theta = \pi$, L_P will be positive and real. In these cases L_P looks like a negative inductance and positive inductance respectively. We see that at $\Delta\theta = 0, \pi$ that $|L_P| \gg L_{sq}$, and as they add in parallel, L_P on presents a minor correction to the SQUID inductance. When $\Delta\theta = \pi/2, 3\pi/2$, L_P will become imaginary. This means that its impedance will be real. When $\Delta\theta = \pi/2$, the pumpistor inductance will be imaginary and negative, meaning that its impedance, $Z_P = i\omega L_P$, is positive and real such that it presents extra dissipation in the circuit. The most interesting case however, is when $\Delta\theta = 3\pi/2$, then the pumpistor impedance will be real and negative. In this case the pumpistor extracts energy from the pump and injects it into the circuit at f_s . The pumpistor presents thus a circuit element whose behavior is periodic with $\Delta\theta$ and can be controlled by varying the pump phase. The model allows for a straightforward analysis of any circuit which incorporates a SQUID, flux-pumped at twice the signal frequency, by replacing the SQUID with the pumpistor element in the circuit model. In Paper B, such an analysis is made for a $\lambda/4$ reflection resonator, terminated to ground with a SQUID. It is shown for degenerate parametric amplification with $f_p = 2f_s$, that the phase dependence of the gain can be fitted with the equivalent circuit model.

2.2.2 Nondegenerate phase-insensitive parametric amplification

In this section we will analyze parametric amplification in the more general sense. More specifically we will look at nondegenerate single mode amplification and multimode amplification in a flux-pumped CPW resonator such as the one

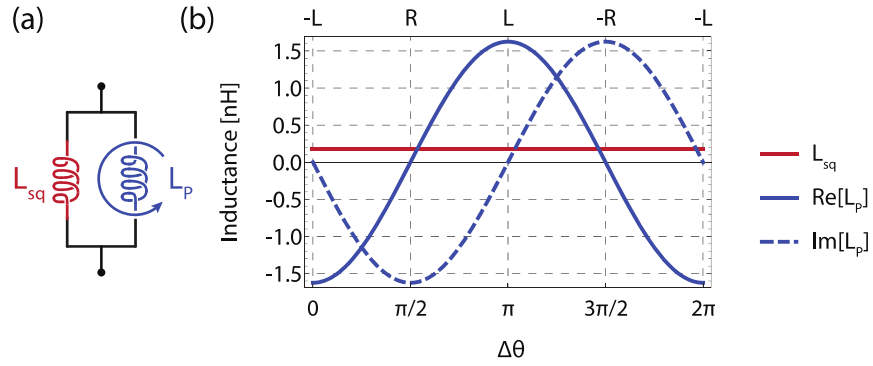


Figure 2.8: *The pumpistor element. (a) The flux-pumped SQUID can be approximated as two inductive elements in parallel: the Josephson inductance L_{sq} (in red) and the pumpistor L_P (in blue). The impedance of the latter is phase dependent. (b) The phase dependence of the real and imaginary parts of L_P . At $\Delta\theta = 0$ ($\Delta\theta = \pi$), the inductance L_P is real and negative (positive). This means that it acts as a negative (positive) inductance in parallel with L_{sq} , plotted for comparison. The pumpistor element will only be a minor correction on the Josephson inductance as $|L_P| \gg L_{sq}$. When $\Delta\theta = \pi/2$ however, L_P becomes imaginary and negative. This means that its impedance, $Z_P = i\omega L_P$, will be real and positive and look thus as a resistance. At this point the pumpistor will present extra loss. When $\Delta\theta = 3\pi/2$ however, L_P becomes imaginary and positive. This means that its impedance look as a negative resistance. At this point the pumpistor will be able to inject energy from the flux pump to the signal frequency f_s .*



2. THEORY

found in Fig. 2.5. The formulas follow from the derivations found in Wustmann and Shumeiko.⁴³ for the single-mode case and have been extended for the multimode case.⁴⁴ We will present the relevant formulas for the gain and discuss the behavior of the amplifier in detail, when modulating the flux through the SQUID around a DC flux bias Φ_{DC} such that $\Phi_{\text{p}}(t) = \Phi_{\text{DC}} + \Phi_{\text{AC}} \cos(\omega_{\text{p}} t)$.

Single-mode nondegenerate parametric amplification

We start out with the equation of motion for the intra-cavity field amplitude $A(t)$, in the case that the (angular) pump frequency ω_{p} is close twice to the mode frequency of mode m and with an input field $B(t)$. The equation of motion in a rotating frame with frequency $\omega_{\text{p}}/2$ is then:

$$i\dot{A} + \delta A + \epsilon A^* + \alpha_m |A|^2 A + i\Gamma_m^{\text{e}} = \sqrt{2\Gamma_m^{\text{e}}} B, \quad (2.49)$$

where $\delta = \omega_{\text{p}}/2 - \omega_m$ is the pump detuning (in angular frequency) between half the pump frequency and the mode frequency $\omega_m = 2\pi f_m$ and $\Gamma_m^{\text{e}} = \omega_m/2Q_m^{\text{e}}$ is the coupling rate of mode m to the transmission line. Note that internal losses in the resonator are neglected. α_m is the Duffing parameter given by:

$$\alpha_m = \frac{\hbar \cos(F)}{2\gamma_0 E_{\text{L}}} \left[\frac{\omega_m \cos^2(k_m d)}{M_m (k_m d)^2} \right]^2, \quad (2.50)$$

where $\gamma_0 = \frac{L_{\text{sq},0}}{L_0 d}$ is the inductance participation ratio, $E_{\text{L}} = (\hbar/2e)^2 (1/L_0 d)$, and M_m is the ‘‘Mass’’ of mode m given by:

$$M_m = 1 + \frac{\sin(2k_m d)}{2k_m d} + \frac{2C_{\text{sq}}}{C_0 d} \cos^2(k_m d). \quad (2.51)$$

The effective pump strength in Eq. (2.49) is denoted by:

$$\epsilon = \delta f \frac{\sin(F)}{2\gamma_0} \frac{\omega_m \cos^2(k_m d)}{M_m (k_m d)^2}. \quad (2.52)$$

We are now interested in the gain of a signal which is detuned by $\Delta = \omega_{\text{s}} - \omega_{\text{p}}/2$ from half the pump frequency, by starting with an input signal $B(t) = B(\Delta)e^{-i\Delta t} + B(-\Delta)e^{i\Delta t}$ and inserting it into the equation of motion, Eq. (2.49). We will also assume that we are in the linear response regime ($\alpha_m \approx 0$) and that we are below threshold ($\epsilon < \epsilon_{\text{th}} = \sqrt{\delta^2 + \Gamma_m^{\text{e}2}}$) for parametric oscillations:

$$\begin{pmatrix} \delta + \Delta + i\Gamma_m^{\text{e}} & \epsilon \\ \epsilon & \delta - \Delta - i\Gamma_m^{\text{e}} \end{pmatrix} \begin{pmatrix} A(\Delta) \\ A^*(-\Delta) \end{pmatrix} = \sqrt{2\Gamma_m^{\text{e}}} \begin{pmatrix} B(\Delta) \\ B^*(-\Delta) \end{pmatrix}, \quad (2.53)$$

or inversely:

$$\begin{pmatrix} A(\Delta) \\ A^*(-\Delta) \end{pmatrix} = \frac{\sqrt{2\Gamma_m^{\text{e}}}}{D} \begin{pmatrix} \delta - \Delta - i\Gamma_m^{\text{e}} & -\epsilon \\ -\epsilon & \delta + \Delta + i\Gamma_m^{\text{e}} \end{pmatrix} \begin{pmatrix} B(\Delta) \\ B^*(-\Delta) \end{pmatrix}, \quad (2.54)$$

where $D = (\Gamma_m^e - i\Delta)^2 + \delta^2 - \epsilon^2$, is the determinant of the matrix in Eq. (2.54). We can now insert this result in the input-output relations:

$$\begin{pmatrix} C(\Delta) \\ C^*(\Delta) \end{pmatrix} = \begin{pmatrix} B(\delta) \\ B^*(-\Delta) \end{pmatrix} + \begin{pmatrix} -i\sqrt{2\Gamma_m^e} \\ i\sqrt{2\Gamma_m^e} \end{pmatrix} \begin{pmatrix} A(\Delta) \\ A^*(-\Delta) \end{pmatrix}, \quad (2.55)$$

and solve for the outgoing field $C(t)$:

$$\begin{pmatrix} C(\Delta) \\ C^*(\Delta) \end{pmatrix} = \frac{1}{D} \begin{pmatrix} (\delta - i\Gamma_m^e)^2 - \delta^2 - \epsilon^2 & 2i\Gamma_m^e\epsilon \\ 2i\Gamma_m^e\epsilon & (\delta + i\Gamma_m^e)^2 - \delta^2 - \epsilon^2 \end{pmatrix} \begin{pmatrix} B(\Delta) \\ B^*(-\Delta) \end{pmatrix} \quad (2.56)$$

The signal power gain is now defined as $G_s = |C(\Delta)|^2 / |B(\Delta)|^2$:

$$\begin{aligned} G_s(\Delta) &= 1 + \frac{4\epsilon^2\Gamma_m^e{}^2}{4\Gamma_m^e{}^2\Delta^2 + (\Gamma_m^e{}^2 - \Delta^2 + \delta^2 - \epsilon^2)^2} \\ &= 1 + \frac{4\epsilon^2\Gamma_m^e{}^2}{4\Gamma_m^e{}^2\Delta^2 + (\Delta^2 + \epsilon^2 - \epsilon_{\text{th}}^2)^2}, \end{aligned} \quad (2.57)$$

whereas the idler gain $G_i = |C(-\Delta)|^2 / |B(\Delta)|^2 = G_s - 1$. The signal gain has a peculiar structure. For small signal detunings $\delta^2 < \epsilon^2 + \Gamma_m^e{}^2$ it is single peaked, with a maximum at $\Delta = 0$. For larger detunings however, the gain becomes smaller and double peaked.⁴³ Close to threshold the gain function can be approximated as a Lorentzian:

$$G_s(\Delta) \approx 1 + \frac{\epsilon^2}{\Delta^2 + \frac{(\epsilon^2 - \epsilon_{\text{th}}^2)^2}{4\Gamma_m^e{}^2}}. \quad (2.58)$$

The bandwidth BW is now defined as:

$$\text{BW} = \frac{(\epsilon^2 - \epsilon_{\text{th}}^2)}{\Gamma_m^e}. \quad (2.59)$$

The amplitude gain for zero detuning ($\Delta = 0$) is then $\sqrt{G} = \epsilon/(\text{BW}/2)$, such that at the threshold, the gain-bandwidth product becomes:

$$\sqrt{G} \cdot \text{BW} = 2\epsilon_{\text{th}}. \quad (2.60)$$

We have plotted the gain and the Lorentzian approximation in Fig. 2.9.

Multimode parametric amplification

In the case that the pump is on resonance with the sum of two modes, $\omega_p = \omega_m + \omega_n + 2\delta$, we will have nondegenerate gain. A signal which falls in one of the modes will be amplified, and as in the degenerate case, an idler will be generated, but now it will end up in the other mode. The expression



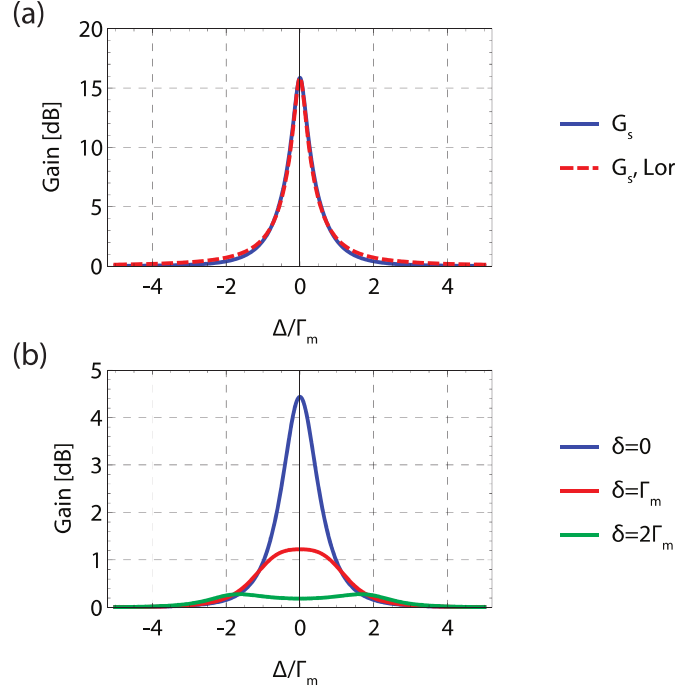


Figure 2.9: Phase-insensitive gain for single-mode parametric amplification. (a) The gain in mode m as a function of normalized signal detuning Δ/Γ_m^e , when the system is pumped at $\omega_p = 2\omega_m$. The pump strength $\epsilon = 0.85\Gamma_m^e$ and the pump detuning $\delta = 0$. The red dashed line shows the Lorentzian approximation of the gain peak. (b) The gain in mode m as a function of normalized signal detuning Δ/Γ_m^e , when the system is pumped at $\omega_p = 2\omega_m + 2\delta$. The pump strength $\epsilon = 0.5\Gamma_m^e$. We have plotted the gain for three different pump detunings δ . We see that at larger detunings the gain becomes smaller and double peaked.

for the gain can be derived in a similar way as for the single-mode case. The equations of motion are however slightly modified:

$$\begin{aligned} i\dot{A}_m + \delta A_m + \alpha_m |A_m|^2 A_m + 2\sqrt{\alpha_m \alpha_n} |A_n|^2 A_m + \epsilon A_n^* + i\Gamma_m^e A_m &= \sqrt{2\Gamma_m^e} B_m \\ -i\dot{A}_n^* + \delta A_n^* + \alpha_n |A_n|^2 A_n^* + 2\sqrt{\alpha_m \alpha_n} |A_m|^2 A_n^* + \epsilon A_m - i\Gamma_n^e A_n^* &= \sqrt{2\Gamma_n^e} B_n^*. \end{aligned}$$

The Duffing parameters α_m and α_n are defined as before, see Eq. (2.50). The pump strength ϵ is now redefined as:

$$\epsilon = \delta f \frac{\sin(F)}{2\gamma_0} \frac{\sqrt{\omega_m} \cos(k_m d)}{\sqrt{M_m} k_m d} \frac{\sqrt{\omega_n} \cos(k_n d)}{\sqrt{M_n} k_n d}. \quad (2.61)$$

Following a similar derivation as before and again in the linear response regime, we now get the following expression for the gain as a function of the signal detuning $\Delta = \omega_s - (\omega_m + \delta)$:

$$G_{mn} = \delta_{mn} + \frac{4\epsilon^2 \Gamma_m^e \Gamma_n^e}{(\Delta^2 - \Delta_0^2 + \epsilon^2 - \epsilon_{\text{th}}^2)^2 + (\Gamma_m^e + \Gamma_n^e)^2 (\Delta - \Delta_0)^2}. \quad (2.62)$$

In this equation δ_{mn} is the Kronecker delta function, $\epsilon_{\text{th}} = \sqrt{\Gamma_m^e \Gamma_n^e + \delta^2 - \Delta_0}$ is the threshold for parametric oscillations. Δ_0 is an asymmetry parameter which takes the difference between the coupling rates Γ_m^e and Γ_n^e into account:

$$\Delta_0 = \delta \frac{\Gamma_n^e - \Gamma_m^e}{\Gamma_n^e + \Gamma_m^e}. \quad (2.63)$$

For $m = n$ Eq. (2.62) reduces to the single-mode result, Eq. (2.57). The equation will also be double peaked for sufficiently large detunings, but now the peaks are asymmetric in height, due to the difference in coupling rates. Even for modest detunings the single peak will have an asymmetric shape. Nevertheless, it is possible to make a Lorentzian approximation close to threshold:

$$\begin{aligned} G_{mn}(\Delta) &\approx \delta_{mn} \\ &+ \frac{4\epsilon^2 \chi \Gamma_m^e \Gamma_n^e}{[\Delta - \Delta_0 + 2\chi \Delta_0 (\epsilon^2 - \epsilon_{\text{th}}^2)]^2 + \chi^2 (\Gamma_m^e + \Gamma_n^e)^2 (\epsilon^2 - \epsilon_{\text{th}}^2)^2}, \end{aligned} \quad (2.64)$$

where $\chi = [4\Delta_0^2 + (\Gamma_m^e + \Gamma_n^e)^2]^{-1}$. When we are at zero pump detuning, $\delta = 0$, the bandwidth is now defined as:

$$\text{BW} = 2\chi(\Gamma_m^e + \Gamma_n^e)(\epsilon^2 - \epsilon_{\text{th}}^2). \quad (2.65)$$

The peak amplitude gain, where $\Delta = 0$, is then $\sqrt{G} = 2\epsilon\sqrt{\chi\Gamma_m^e\Gamma_n^e}/(\text{BW}/2)$. ϵ can now be replaced by ϵ_{th} which gives:

$$\sqrt{G} \cdot \text{BW} = 4\epsilon_{\text{th}} \sqrt{\chi\Gamma_m^e\Gamma_n^e}. \quad (2.66)$$

It is possible to get a Lorentzian approximation and the gain-bandwidth product for the degenerate case by taking $\Gamma_m^e = \Gamma_n^e$. We have plotted the gain as a function of the different detunings, as well as the Lorentzian approximations, in Fig. 2.10



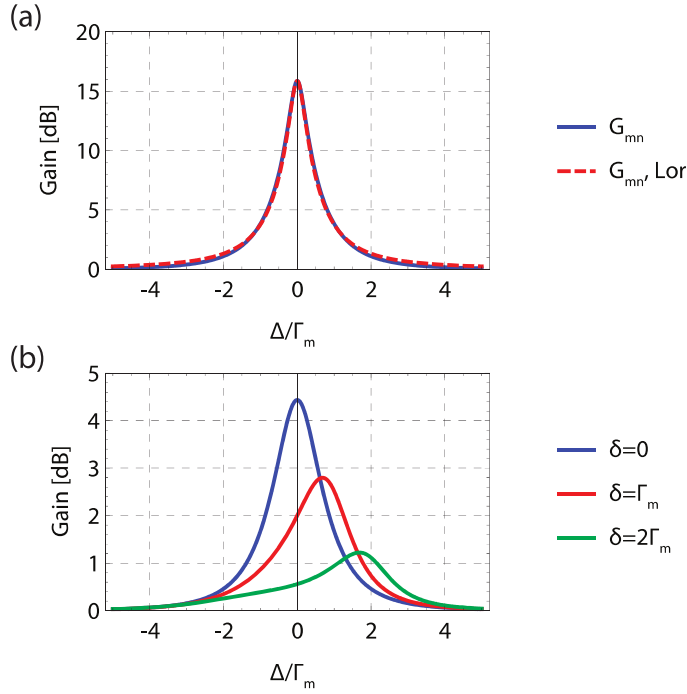


Figure 2.10: *Multimode gain.* (a) The gain in mode m as a function of normalized signal detuning Δ/Γ_m^e , when the system is pumped at $\omega_p = \omega_m + \omega_n$. The pump strength $\epsilon = 0.85\sqrt{\Gamma_m^e \Gamma_n^e}$ and the pump detuning $\delta = 0$. The red dashed line show the Lorentzian approximation of the gain peak. (b) The gain in mode m as a function of normalized signal detuning Δ/Γ_m^e , when the system is pumped at $\omega_p = \omega_m + \omega_n + 2\delta$. The pump strength $\epsilon = 0.5\sqrt{\Gamma_m^e \Gamma_n^e}$. We have plotted the gain for three different pump detunings δ . We see that at larger detunings, the gain becomes double peaked. Note that the coupling rates for the different modes is different, $\Gamma_m^e \approx 0.4 \cdot \Gamma_n^e$.

2.3 Intermode conversion in a multimode resonator

In this section we consider intermode conversion resulting from parametrically driving a multimode resonator. The resonator I consider is very similar to the one used in the parametric amplification section above and consists of a SQUID terminated CPW resonator which is flux-pumped. Parametric amplification occurs when the pump frequency is equal to either twice the frequency of one of the modes, $f_p \approx 2 \times f_m$ (single-mode amplification), or to the sum of the frequencies of two of the modes, $f_p \approx f_m + f_n$ (multimode amplification). Intermode conversion on the other hand is possible when the pump frequency is equal to the difference frequency between two modes, $f_p \approx f_n - f_m$ with $f_n > f_m$. In parametric amplification there is an energy transfer from the pump to both the signal and idler, providing gain. In intermode frequency conversion however an excitation at the signal frequency will exchange energy with the pump and be coherently transferred to the idler frequency and vice versa. A continuous drive will cause the photons to oscillate between the modes similar to Rabi oscillations for an atom. The result is an interaction where the total number of photons at the signal and idler frequencies remain constant, meaning that there is no power gain.

The derivation for the intermode conversion presented here follows the work from Wustmann and Shumeiko but where the pump is now on resonance with the difference between two of the modes $\omega_p = \omega_n - \omega_m + 2\delta$ (with δ as before the angular pump detuning and $\omega_n > \omega_m$).⁴⁴ Any signal close to one of the pumped modes will then be converted to the other mode. Similar to the multimode case I start out from the equation of motion for the pumped modes:

$$\begin{aligned} i\dot{A}_m - \delta A_m + \alpha_m |A_m|^2 A_m + 2\sqrt{\alpha_m \alpha_n} |A_n|^2 A_m + \epsilon A_n + i\Gamma_m A_m &= \sqrt{2\Gamma_m^e} B_m \\ i\dot{A}_n + \delta A_n + \alpha_n |A_n|^2 A_n + 2\sqrt{\alpha_m \alpha_n} |A_m|^2 A_n + \epsilon A_m + i\Gamma_n A_n &= \sqrt{2\Gamma_n^e} B_n, \end{aligned}$$

where Δ is the signal detuning from the coupled frequencies, $\omega_m - \delta$ and $\omega_n + \delta$. The relation between the different detuning is shown in Fig. 2.11. The Duffing parameters α_m and α_n are defined as before, see Eq. (2.50). The pump strength ϵ is given by Eq. (2.61). Different from before is that we now explicitly allow for internal loss. The external coupling rate is defined as before, $\Gamma_m^e = \omega_m / (2Q_m^e)$, but I now also introduce the total damping rate $\Gamma_m = \Gamma_m^e + \Gamma_m^i = \omega_m / (2Q_m)$. This includes the internal damping rate $\Gamma_m^i = \omega_m / (2Q_m^i)$.

Similar to the derivation of the single-mode nondegenerate gain it is possible to use the input-output relation to express the outgoing field $C(t)$ as a function of the incoming field $B(t)$ in the linear response regime ($\alpha_m = \alpha_n = 0$):

$$\begin{pmatrix} C_m \\ C_n \end{pmatrix} = \begin{pmatrix} 1 - \frac{2i\Gamma_m^e(\Delta + i\Gamma_n + \delta)}{D} & \frac{2i\epsilon\sqrt{\Gamma_m^e\Gamma_n^e}}{D} \\ \frac{2i\epsilon\sqrt{\Gamma_m^e\Gamma_n^e}}{D} & 1 - \frac{2i\Gamma_n^e(\Delta + i\Gamma_m - \delta)}{D} \end{pmatrix} \begin{pmatrix} B_m \\ B_n \end{pmatrix}, \quad (2.67)$$



2. THEORY

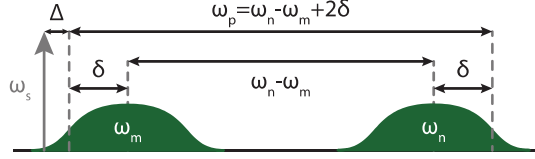


Figure 2.11: An overview of the different detunings for the intermode conversion. δ is the angular pump detuning from $\omega_n - \omega_m$, where $\omega_n > \omega_m$. The signal detuning, Δ , is referred to the pumped frequencies $\omega_m - \delta$ and $\omega_n + \delta$.

We can now identify the reflection coefficient for modes m and n :

$$S_{mm} = \frac{C_m}{B_m} = \frac{(\Delta - \delta + i(\Gamma_m^i - \Gamma_m^e))(\Delta + \delta + i\Gamma_n) - \epsilon^2}{(\Delta - \delta + i\Gamma_m)(\Delta + \delta + i\Gamma_n) - \epsilon^2} \quad (2.68)$$

$$S_{nn} = \frac{C_n}{B_n} = \frac{(\Delta - \delta + i\Gamma_m)(\Delta + \delta + i(\Gamma_n^i - \Gamma_n^e)) - \epsilon^2}{(\Delta - \delta + i\Gamma_m)(\Delta + \delta + i\Gamma_n) - \epsilon^2}. \quad (2.69)$$

The conversion between the modes is given by:

$$S_{mn} = \frac{C_m}{B_n} = S_{nm} = \frac{C_n}{B_m} = \frac{2i\epsilon\sqrt{\Gamma_m^e\Gamma_n^e}}{(\Delta - \delta + i\Gamma_m)(\Delta + \delta + i\Gamma_n) - \epsilon^2}. \quad (2.70)$$

I have plotted the reflection coefficients and the conversion in , see Fig. 2.12. It is possible to identify two distinct resonances in Eqs. (2.68) and (2.69) when $\Delta = \pm\delta$. Around mode m these resonances are found at $\omega_{m,1} = \omega_m$ and $\omega_{m,2} = \omega_m - 2\delta$, whereas close to mode n these resonances are found at $\omega_{n,1} = \omega_n + 2\delta$ and $\omega_{n,2} = \omega_n$. Note that $\omega_{m,1}$ equals $\omega_{n,1}$ shifted by the pump frequency, $\omega_{m,1} = \omega_{n,1} - \omega_p$, and that also $\omega_{m,2}$ equals $\omega_{n,2}$ shifted by the pump frequency, $\omega_{m,2} = \omega_{n,2} - \omega_p$. The resonances $\omega_{m,1}$ and $\omega_{m,2}$, and the resonances $\omega_{n,1}$ and $\omega_{n,2}$ are thus coupled by the pump, leading to the new hybridized frequencies, see Fig. 2.12:

$$\omega_{m,\pm} = \frac{1}{2} \left(\omega_{m,1} + \omega_{m,2} \pm \sqrt{4\epsilon^2 + (\omega_{m,1} - \omega_{m,2})^2} \right) \quad (2.71)$$

$$\omega_{n,\pm} = \frac{1}{2} \left(\omega_{n,1} + \omega_{n,2} \pm \sqrt{4\epsilon^2 + (\omega_{n,1} - \omega_{n,2})^2} \right). \quad (2.72)$$

These can be rewritten as:

$$\omega_{m,\pm} = \omega_m - \delta \pm \sqrt{\epsilon^2 + \delta^2} \quad (2.73)$$

$$\omega_{n,\pm} = \omega_n + \delta \pm \sqrt{\epsilon^2 + \delta^2}. \quad (2.74)$$

This shows that the minimum splitting is found when the pump detuning $\delta = 0$. At that point the splitting is equal to 2ϵ .

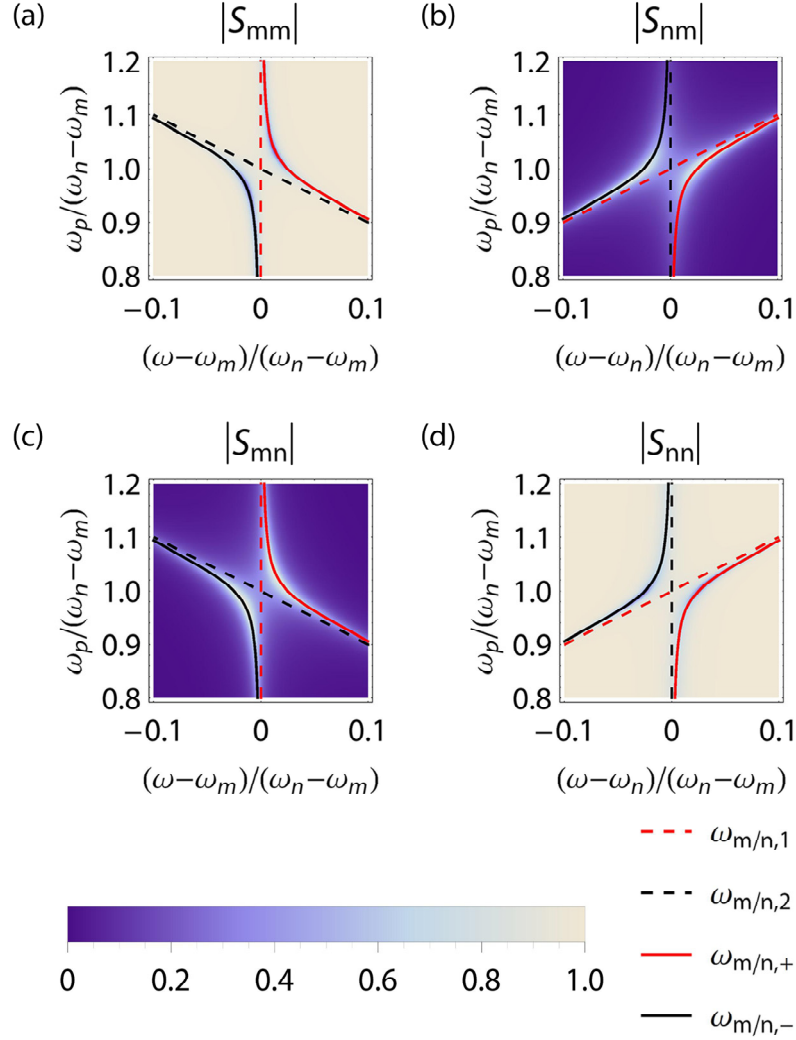


Figure 2.12: The magnitude response of the intermode conversion when pumping the resonator at the difference frequency of modes m and n , with a pump strength $\epsilon = 10\Gamma_m^e$. (a) $|S_{mm}| = |\frac{C_m}{B_m}|$, (b) $|S_{nm}| = |\frac{C_n}{B_m}|$, (c) $|S_{mn}| = |\frac{C_m}{B_n}|$ and (d) $|S_{nn}| = |\frac{C_n}{B_n}|$ as a function of probe frequency and pump frequency. We see that the magnitude at the mode where we send in a signal shows the largest dip when on resonance, see panels (a) and (d). At those points we see that we get a maximum output in the other mode, see panels (b) and (c) respectively, showing that we have frequency conversion there. The reflection coefficient contains two resonances when $\Delta = \pm\delta$. These resonances are shown as the dashed lines, where the red dashed line is for $\Delta = +\delta$ and the black dashed lines is for $\Delta = -\delta$. When we turn on the pump these resonances couple and hybridize into two new resonances, marked by the full red and black lines. The minimum splitting is reached when $\delta = 0$ and is equal to 2ϵ .



2.4 Dynamical Casimir Effect

2.4.1 Introduction

The Casimir force was first postulated in 1948 by the Dutch scientist H. Casimir.⁴⁵ It stated that there is an attractive force between two perfectly conducting plates when they are brought into close proximity of one another, even when in perfect vacuum, see Fig. 2.13(a). The effect, now called the static Casimir effect, is a direct result from the quantized nature of the vacuum field. Due to the Heisenberg uncertainty principle,⁴⁶ the vacuum is not void from energy, but has a so called zero-point energy. This energy is found as so called vacuum fluctuations which can be understood as pairs of virtual particles continuously flitting in and out of existence. As the plates pose now a boundary condition on the vacuum modes, the number of modes able to exist between the plates, when they are brought closely together, is smaller than the number of modes available outside of the plates. This means that the amount of vacuum fluctuations between the plates is lower than outside of the plates. Due to this there will be a radiative pressure on the plates, pushing them together. However, the forces generated are minute. Two plates of 1 m² held at the width of a human hair (100 μm) only generates a force of approximately 13 pN between them. It took until 1997 for the first conclusive experimental verification of the effect, when attractive force between a sphere and a plate, held as close as 600 nm apart, was measured to within 5% of the theoretically predicted value by S.K. Lamoreaux.⁴⁷

In 1970, Gerald Moore predicted another effect which stems from the interaction between the vacuum and a set of perfectly conducting mirrors that make up a cavity.¹⁵ He stated that if one of the mirrors is oscillating, the interaction between the mirror (to be more precise the boundary condition) and the vacuum fluctuation is capable of exciting photons out of the vacuum, see Fig. 2.13(b). The result was later generalized to the case of a single mirror undergoing a nonuniform acceleration in vacuum.^{13,14} The effect was only termed the dynamical Casimir effect (DCE) much later and there exist still today some ambiguity about the definition.^{48,49} The excitations are created due to a vacuum mode mismatch in time. As the mirror constitutes a boundary condition on the vacuum modes, any movement of the mirror must be accompanied with a change in the mode structure of the vacuum. Whenever the velocity of the mirrors is small, the mode structure adapts adiabatically. However, when the rate of change becomes appreciable to the speed of light, the mode structure is unable to adjust and photons are excited non-adiabatically. For the case of a single moving mirror the photon production rate has been calculated by A. Lambrecht *et al.*:⁵⁰

$$\frac{N}{T} = \frac{a^2 \omega_p^3}{6\pi c^2} = \frac{\omega_p}{6\pi} \left(\frac{v}{c}\right)^2, \quad (2.75)$$

where N is the number of photons produced in a frequency range from 0

| Action | $\omega_p/2\pi$ | a | N/T |
|--------------------|-----------------|-----------|---|
| Hand-waving mirror | 1 Hz | 1 m | $\sim 1.4 \times 10^{-16}$ photons/s ≈ 10 photons in the lifetime of the earth |
| MEMS Oscillator | 10 MHz | 1 μ m | $\sim 1.4 \times 10^{-7}$ photons/s ≈ 1 photon per 169 days |
| SQUID | 10 GHz | 0.5 mm | $\sim 1.15 \times 10^6$ photons/s ≈ 145000 photons in the time it takes to blink an eye |

Table 2.2: DCE photon production N/T , where N is the number of photons produced in a frequency range from 0 to ω_p per unit time T . For mechanical systems the photon production rate is extremely low because the maximum reachable velocity is only a small fraction of the speed of light. The SQUID provides an electromagnetic boundary condition, meaning that much larger speeds are possible. The speed of light in the transmission line is also reduced to $\sim 40\%$ of the speed of light in vacuum.

to ω_p per unit time T . Note that this expression is valid for a double-sided mirror (and has to be divided by two in the case of a single-sided mirror). The trajectory of the mirror is given by $a \cos(\omega_p t)$, c is the speed of light and $v = \omega_p a$ is the maximal velocity reached by the mirror. We see thus that the photon production rate is proportional to the square of the ratio of the maximum mirror velocity to the speed of light. This explains why it has been so difficult to measure the DCE in mechanical systems, as it is unfeasible to reach sufficiently high mirror velocities. We give some examples in Table 2.2. In the results presented in Paper A, we overcome this difficulty by modulating an effective length rather than a physical object.

There are a number of other effects which stem from the interaction with vacuum fluctuation and which are related to the DCE, namely parametric amplification of vacuum fluctuations,⁵¹ the Unruh effect,⁵² and Hawking radiation,^{53,54} see Fig. 2.14. I will briefly touch upon these other effects and explain their relation to the DCE in a conceptual manner. For a nice review I can recommend the paper by P.D. Nation *et al.*⁵⁵ The relation between the DCE and parametric amplification of the vacuum has also been treated in another paper.⁵⁶

Parametric amplification of vacuum fluctuation and the DCE are closely related and the exact differences between the two effects are still debated. Both effects will excite photons out of the vacuum, by modulating the mode structure of the vacuum in a non-adiabatic way. We distinguish two different methods of modulating the mode structure. In the original proposals, the position of a mirror was modulated, which is the modulation of a boundary condition on the mode structure. I assume a boundary condition to be much smaller than the wavelength. Another option is the modulation of a bulk



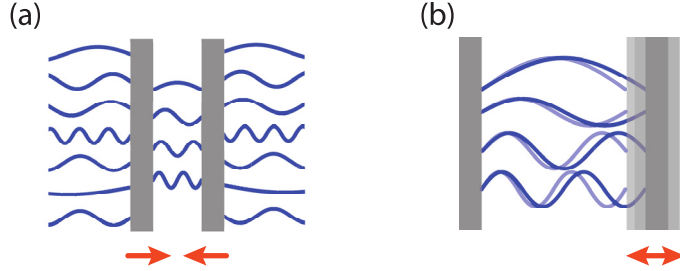


Figure 2.13: *The static and dynamical Casimir effect. (a) The static Casimir effect is described as the attractive force between two plates when they are held closely together. This is due to a spatial mismatch in the mode structure of the vacuum. (b) The dynamical Casimir effect is the excitation of vacuum fluctuations out of the vacuum due to a mismatch of the mode structure of the vacuum in time. The case shown here is a cavity where one of the mirror is oscillating.*

property of the nonlinear medium, essentially modulating the speed of light. This has been done in superconducting circuits by the flux-modulation of a Josephson metamaterial in a cavity setup.⁵⁷ In quantum optics it is often the polarization of an optical nonlinear crystal which is modulated, such as in an optical parametric oscillator (OPO). Another way of categorizing these effects is by the use of a resonant cavity or not. The shape of the spectrum of the produced radiation will depend strongly on the presence of such a cavity. In a cavity setup the quality factor of the cavity will now reshape the output spectrum of the generated photons to a peaked spectrum whose shape depends on the detuning between the cavity and half the pump frequency. In the case that the pump is on resonance with twice the cavity frequency, the spectrum will exhibit a single peak centered at half the pump frequency. A detuning will make the spectrum double peaked. In the absence of a cavity, such as in the single mirror setup, there will be broadband photon generation instead, which is parabolic of shape and centered around half the pump frequency. We have categorized some experimental implementations in Table 2.3. In all cases shown in Table 2.3, the process will produce photons in correlated pairs (due to down-conversion from the pump) and this means that the spectrum will exhibit two-mode squeezing (TMS). I will discuss the properties of TMS more in detail below, but one important attribute is that if one measures the statistics of only one of the two-mode squeezed modes, that mode will appear to be in a thermal state.

The Unruh effect on the other hand states that a continuously accelerating observer, will observe the quantum vacuum as a thermal state, with a temperature proportional to his acceleration. This is because if we convert the vacuum modes from the inertial reference frame to the accelerating reference frame of the observer that each vacuum mode is rewritten as a two-mode squeezed state, where the two modes are lying on the opposite sides of the event horizon. This means that the observer is only able to sample one of the modes (the

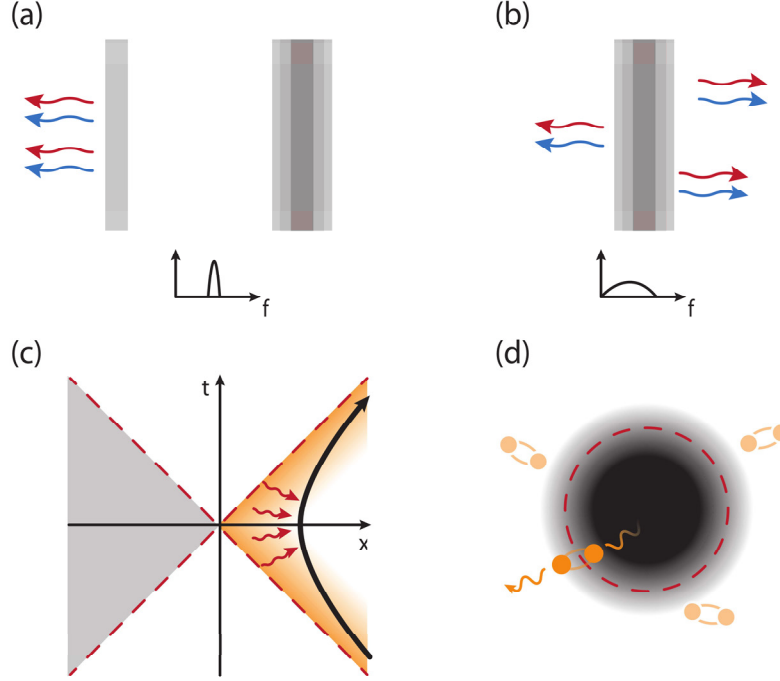


Figure 2.14: An illustration of interaction with the vacuum. (a) Parametric amplification of vacuum fluctuations occurs in a resonant setup. Represented here is the case where one of the mirror of a cavity is modulated, generating two-mode squeezed radiation (depicted with the blue and red arrows). These modes share strong correlations of their noise properties. The spectrum is peaked and enhanced by the quality factor of the cavity. (b) The DCE in the single-mirror setup also generates two-mode squeezed radiation. The output spectrum is now parabolic in shape and has a maximum at half the oscillation frequency. (c) The Unruh effect is where a continuously accelerating observer (depicted here by the black arrow) will observe the inertial vacuum as a thermal state in his reference frame. This is because each vacuum mode in the inertial frame will be a two-mode squeezed state in the observer's frame, where one of the two modes lies on the other side of the event horizon (red dashed lines) in a part of space-time which is out of causal contact with the observer (grey area). This means that the observer only has access to one mode which then appears as a thermal state, with a temperature proportional to the acceleration. (d) Hawking radiation is the black body radiation of a black hole. This occurs because virtual particle-antiparticle pairs which are formed everywhere (depicted by the connected dots) can have one of the particles appear across the event horizon of the black hole (red dashed line) before they can annihilate. This leaves the remaining particle free to reach an observer at infinity. As the modes of the virtual pair which was excited are also two-mode squeezed, and only one of the two is observable, the radiation will look thermal with a temperature proportional to the surface gravity of the black hole.



2. THEORY

| | Open space | Cavity Setup |
|---------------------------------|---|---|
| Modulated boundary | SQUID terminated transmission line ¹ | Flux-pumped JPA Thin Crystal OPO ⁵⁸ |
| Modulated speed of light | Spontaneous parametric down-conversion | Josephson metamaterial ⁵⁷ general OPO |

Table 2.3: *Comparing different implementations which provide parametric amplification of vacuum fluctuation. The experimental observation of the DCE described in this thesis uses a SQUID terminated transmission line.*

one on his side of the event horizon). Just as we explained above, that mode (which is part of a two-mode squeezed pair of modes) will now appear to be in a thermal state.

Finally Hawking radiation is also connected to the DCE in a similar way. Hawking radiation is the thermal blackbody radiation which is measured by an observer at infinity, when looking at a black hole. The temperature measured will now be proportional to the surface gravity of the black hole. A toy model to explain Hawking radiation uses the virtual particle pair interpretation of quantum vacuum fluctuation. A virtual photon pair close to the event horizon of a black hole has a chance that one the virtual photons will be trapped in the black hole, before they can annihilate again. In that case the remaining photon will be free to reach the observer. As the photons were initially two-mode squeezed, the radiation reaching the observer will now appear again as a thermal stated.

2.4.2 SQUID as tunable boundary condition

In the measurements presented in the Paper A, we have a system which reproducing the single-mirror DCE. The system consists of a CPW transmission line which is terminated to ground by a SQUID. The SQUID will have an inductance, which is modulated by an external magnetic flux. The SQUID poses a boundary condition on the vacuum modes similar to Eq. (2.35). By inserting the proper equation for the wave function in terms of input and output operators (and neglecting the term proportional to C_{sq}) it is possible to map the SQUID inductance to an effective length $L_{eff}(\Phi)$:⁵⁹

$$L_{eff}(\Phi) = \frac{L_{sq}(\Phi)}{L_0}, \quad (2.76)$$

where $L_{sq}(\Phi)$ is the flux dependent SQUID inductance and L_0 is the inductance per unit length of the CPW, see Fig. 2.15. It is now easy to understand that periodically modulating the flux through the SQUID around a DC value, allows us to periodically modulate the effective length, thereby virtually moving the point at which the transmission line is shorted. As we are not changing a physical length the maximum velocities that can be reached are much higher

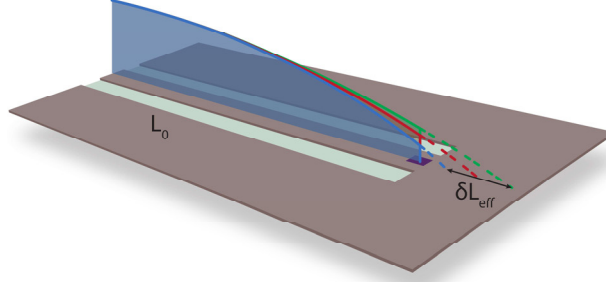


Figure 2.15: *Modulation of the effective length. When we tune the SQUID inductance by means of the external magnetic flux we change the phase difference across the SQUID (purple square). The colored lines is the voltage envelope for three different flux values. We can convert this modulation of inductance to an effective length modulation by dividing the change in inductance by the inductance per unit length of the CPW transmission line.*

than in mechanical systems, and can in fact reach an appreciable fraction of the speed of light. For a small-amplitude harmonic modulation of the effective length, δL_{eff} , the output photon flux density can then be calculated to be:^{56,59}

$$n_{\omega}^{\text{out}} = \bar{n}_{\omega}^{\text{in}} + \left(\frac{\delta L_{\text{eff}}}{v_p} \right)^2 \omega |\omega_p - \omega| \bar{n}_{\omega_p - \omega}^{\text{in}} + \left(\frac{\delta L_{\text{eff}}}{v_p} \right)^2 \omega (\omega_p - \omega) \Theta [\omega_p - \omega], \quad (2.77)$$

where $\bar{n}_{\omega}^{\text{in}} = 1 / [\exp(\hbar\omega/k_B T) - 1]$ is the thermal input field, v_p is the phase velocity in the CPW (the speed of light), ω_p is the pump frequency and Θ denotes the Heaviside Step function. In our CPW transmission lines v_p is $\sim 40\%$ of the speed of light in vacuum. The first term in this equation is the reflection of the thermal input field. The second term is the up-conversion of the thermal input field to the pump frequency and the last term is the DCE radiation. If we integrate the DCE part over frequency from zero to the pump frequency ω_p , we recover Eq. (2.75) (actually with a factor of $1/2$, because we have a single-sided mirror). We plot the result of Eq. (2.77) in Fig. 2.16

2.4.3 Two-mode squeezing and second-order coherence

The photons in the DCE are created in pairs such that their frequencies add up to the pump frequency. This is reflected in the parabolic spectrum which is symmetric around $\omega_p/2$. Two photon processes are known to generate a two-mode squeezed state, which in this case means that there are strong



2. THEORY

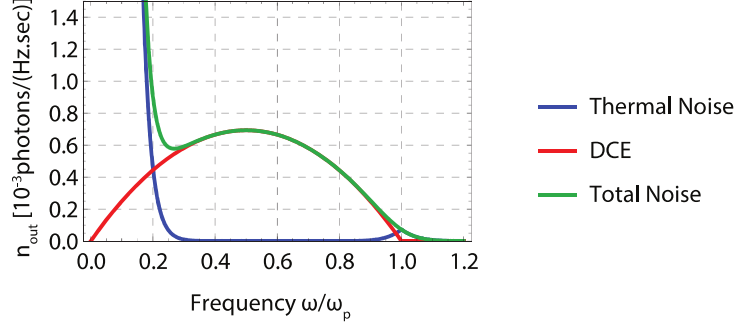


Figure 2.16: The output photon flux density of a pumped SQUID at the end of a CPW transmission line. The blue line denotes the thermal contribution, with the reflection of the thermal input field at low frequencies and the upconverted thermal noise to the pump frequency (first term and second term in Eq. (2.75) respectively). The red parabola denotes the DCE radiation (third term in Eq. (2.75)). The green line is the then the total output amount of output photons per Hertz bandwidth and per second.

correlations between the photons symmetric around half the pump frequency. The two-mode squeezing is theoretically treated by Caves and Schumaker⁶⁰.

The two-mode squeezing can be expressed in terms of the quadrature voltages at the two sidebands (I_+, Q_+ at the upper sideband and I_-, Q_- at the lower sideband), which are the quantities we measure experimentally. The two-mode squeezing is defined in terms of these quantities as:

$$\sigma_2 = \frac{\langle I_+ I_- \rangle - \langle Q_+ Q_- \rangle}{P_{\text{avg}}}, \quad (2.78)$$

where $\langle \dots \rangle$ stands for the mean and P_{avg} is the total averaged power in the two sidebands:

$$P_{\text{avg}} = \frac{1}{2} (\langle I_+^2 \rangle + \langle I_-^2 \rangle + \langle Q_+^2 \rangle + \langle Q_-^2 \rangle) \quad (2.79)$$

Note that Eq. (2.78) assumes that a proper angle has been chosen, such that $\langle I_+ Q_- \rangle = \langle I_- Q_+ \rangle = 0$. Furthermore the specific structure of the two-mode squeezing requires that $\langle I_+ I_- \rangle = -\langle Q_+ Q_- \rangle$ and that $\langle I_+ Q_- \rangle = \langle I_- Q_+ \rangle$. It is important to realize that the individual sidebands remain unsqueezed, which is quantified by their single-mode squeezing:

$$\sigma_1 = \frac{\langle I^2 \rangle - \langle Q^2 \rangle}{\langle I^2 \rangle + \langle Q^2 \rangle}. \quad (2.80)$$

This means that each individual sideband will appear as a thermal state. An overview of the different squeezing parameters can be found in Fig. 2.17.

Finally I introduce another statistical property of the radiation. Because DCE photons are created pairwise, the output radiation should also exhibit photon number correlations between the symmetrically offset frequencies around

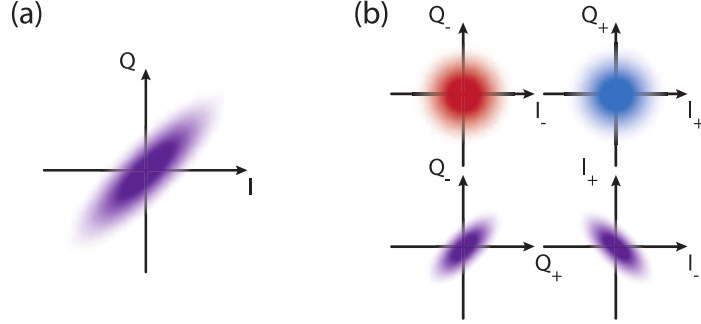


Figure 2.17: *Noise quadrature squeezing. (a) Single-mode squeezing manifests itself as a difference in the noise of the different quadratures of a single mode. The noise in one quadrature will be suppressed whereas the noise in the other gets equally larger. (b) Two-mode squeezing will keep the individual modes at the upper and lower sidebands unsqueezed (top two panels). There will however be strong correlations between the noise of the two modes. In two-mode squeezed radiation $\langle I_+ I_- \rangle = -\langle Q_+ Q_- \rangle$, whereas $\langle I_+ Q_- \rangle = \langle I_- Q_+ \rangle$.*

half the pump, $\omega_p/2 - \delta\omega$ and $\omega_p/2 + \delta\omega$, where $\delta\omega < \omega_p/2$. In the time-domain this means that the radiation should exhibit photon-bunching. This is because the probability to detect two photons simultaneously, one at each symmetrically offset frequency, is the same as the probability to detect just one photon (in the absence of noise). These correlations are expressed using the normalized second-order correlation function, $g_{+-}^{(2)}(\tau)$. We can express $g_{+-}^{(2)}(\tau)$ in terms of the measured powers as:^{56,61}

$$g_{+-}^{(2)}(\tau) = 1 + \frac{\langle P_+(\tau)P_-(t+\tau) \rangle - \langle P_+(\tau) \rangle \langle P_-(t+\tau) \rangle}{(\langle P_+(t) \rangle - \langle P_{N,+}(t) \rangle)(\langle P_-(t) \rangle - \langle P_{N,-}(t) \rangle)}, \quad (2.81)$$

where τ is the time delay between the detectors, $P_{\pm} = I_{\pm}^2 + Q_{\pm}^2$ is the output power measured at the symmetric offset frequencies, $\omega_p/2 \pm \delta\omega$ and $P_{N,\pm}$ is the output power at those frequencies when the pump is turned off, such that we measure just the amplifier noise.

2.5 On-chip Mach-Zehnder interferometer

The Mach-Zehnder interferometer is a device which was proposed by Ludwig Zehnder in 1891 and improved by Ludwig Mach in 1892.^{62,63} It is a relatively simple device which allows for the measurement of the relative phase shift between the light traveling in two paths. To do so the light interferes by division-of-amplitude. Note that this is different from interference by the division-of-wavefront, such as in Young's double slit experiment, where it is also the relative phase difference between two paths which is measured.⁶⁴ The working principle of the Mach-Zehnder interferometer is explained in



2. THEORY

Fig. 2.18(a). We analyze the case where the path lengths are equal and where the additional phase shift ϕ in the bottom path is 0. The collimated light from the source falls onto a 50/50 beamsplitter, A. When following the upper arm, it then reflects off mirror B' and falls onto beamsplitter C. At this point, the phase of the light has picked up a phase 2π (a π shift for each reflection at A and B'), where we neglect the phase due to the path length as this is the same for both arms. The light following the bottom path goes straight through beamsplitter A, and reflects off mirror C, picking up a phase shift of π (again neglecting the path length phase). When we now look at the light going to detector 1, then the light from the top arm goes through the beamsplitter, meaning that the total additional phase remains 2π . The light from the bottom arm makes an additional reflection and picks up an additional π , such that the light from both arms constructively interferes (the light picked up a phase of 2π in both arms). The situation for detector 2 is different as the light reaching detector 2 from the bottom arm retains its π phase shift, whereas the light from the upper arm retains its 2π phase shift. This is because the reflection of the glass-dielectric interface does not pick up an additional π . This means that the light from both arms has a phase difference of π , causing destructive interference. Any additional phase shift ϕ in the bottom arm will now change the interference conditions at both detectors allowing to measure the phase difference.

The device found in the Paper E is a Mach-Zehnder-type on-chip interferometer, which works at microwave frequencies, see Fig. 2.18(b). In this device a signal is split equally using an on-chip power splitter. Half of the signal is sent down a fixed length arm, where the length of the arm has been designed such that the phase shift in this arm is π for the frequency of interest. The upper arm contains a SQUID (or actually two SQUIDs in series). The inductance of the SQUIDs of the SQUID can be tuned, such that the phase shift in the upper arm can be changed.

The power splitters/combiners used on the chip have been designed such that they divide the power equally between the two arms. The choice was made to use a loss-less, non-resonant design, which minimizes the reflections at the input and output ports. This means that the splitter/combiner can not be matched at all three ports. This is because three-port networks can never be made loss-less, reciprocal and matched at the same time (one of these has to be sacrificed for the others). To match the $50\,\Omega$ input line, the arms of the interferometer have been designed to have a characteristic impedance $Z_{\text{CPW}} = \sqrt{L_0/C_0} = 100\,\Omega$. When the lines recombine at the output of the interferometer there will however be reflections as each arm will see the other arm ($100\,\Omega$) in parallel with the output line ($50\,\Omega$), which looks like an impedance of $33.33\,\Omega$. This results in a reflection coefficient $\Gamma = -0.5$, see Eq. (2.23). The reflections at the power combiner will lead to additional resonances.

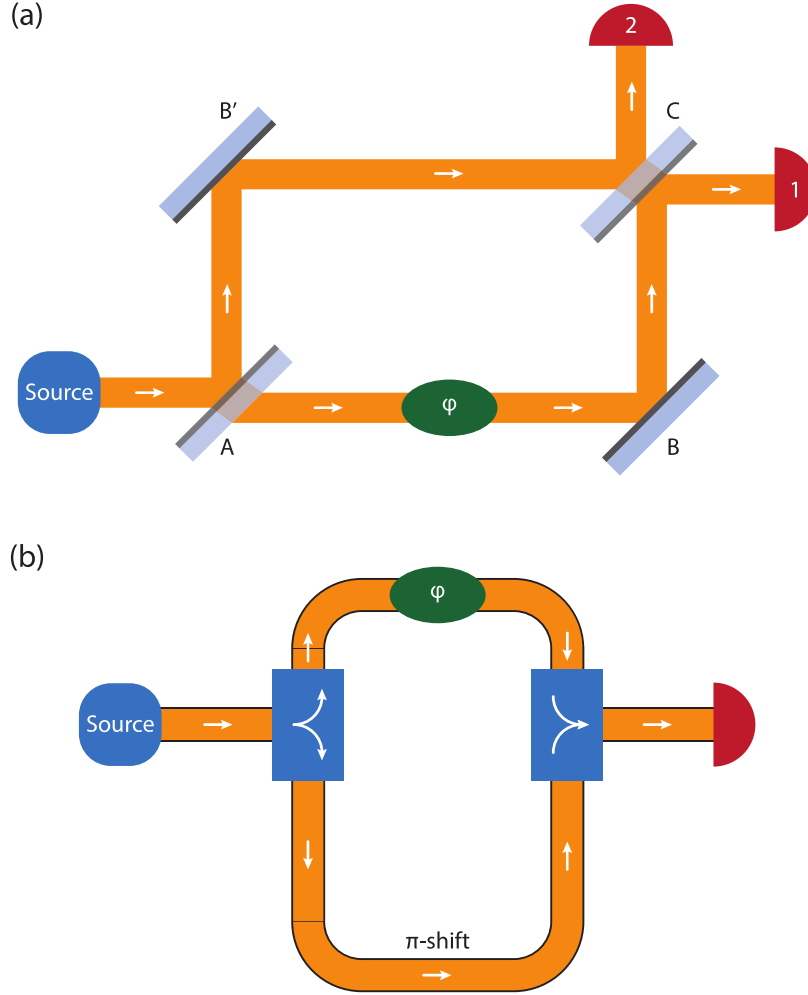


Figure 2.18: *The Mach-Zehnder interferometer. (a) The optical Mach-Zehnder interferometer allows for a measurement of the phase shift ϕ between the two arms by measuring the output of the two detectors. The light is split with a 50/50 beamsplitter (labeled A) before it reflects of the mirrors B and B'. The light is then sent through a second beamsplitter C. (b) The on-chip Mach-Zehnder interferometer. In this setup the incoming signal is split using a power splitter. The bottom arm of the interferometer is designed to have a phase shift of π at the frequency of interest. The phase shift in the top arm depends on the flux tunable SQUID inductance in that arm. The two arms are recombined in another power splitter, allowing for interference between the arms.*



3

Experimental techniques

A variety of different techniques are used, both during the fabrication of the samples as well as for the measurements performed on the samples. In the first section of this chapter I describe three key processes used in the fabrication of the samples. The detailed recipes can be found in Appendix A. In the second section I describe the working principle behind the dilution refrigerator and pulse tube coolers used to cool the samples down to their working temperature of 10 mK. I also give some pointers on how to design a microwave measurement setup. Finally in the last section I give a detailed explanation of the noise calibrations which were performed in some of the measurements.

3.1 Sample fabrication

The samples in this thesis are fabricated in the cleanroom of the MC2 department at Chalmers. This facility is a state-of-the-art cleanroom with a total floor space of 1240 m² divided into a class 10-100 and a class 1000-10000 section. A wide range of lithography equipment, evaporators, sputtering machines and characterization tools are available to the users. The samples are made on intrinsic silicon wafers using the techniques described below. The detailed fabrication recipes for the samples used in this thesis can be found in Appendix A.

3.1.1 Photolithography

Photolithography is used to make structures down to approximately 1 μm . Smaller feature sizes are technically possible, but alignment becomes progressively harder and more advanced equipment is needed. In a photolithographic process a pattern is transferred from a so called photomask onto a photosensitive resist film on the wafer by means of UV light, see Fig. 3.1. First the resist is spin-coated onto the wafer with a spinner. The thickness of the film is



3. EXPERIMENTAL TECHNIQUES

tailored, by choosing the appropriate rotation speed and duration. It has to be chosen such that the film is robust enough for processing, while still being thin enough to achieve the desired resolution. After this, the wafer is baked to stabilize the resist layer. The pattern, which needs to be transferred, has first been written onto a photomask by means of electron-beam lithography. I used soda-lime masks, with a chromium pattern deposited onto it. The transfer of the pattern is done with a mask aligner. This device contains a stage which can be used to carefully align the wafer with the mask, after which the resist can be exposed by the UV light of an Hg lamp. The resist is a polymer which will be modified by the UV light, after which it becomes more (positive resist) or less (negative resist) soluble in a chemical called the developer. The developer will thus remove the exposed parts of the resist for a positive resist and the unexposed parts when a negative resist is used. After these steps the pattern (or the inverted pattern) is transferred onto the resist, where it can be used for further processing.

In my sample designs I have used a variation on this technique, where two resists are deposited on top of each other. The top resist (S1813) is used for patterning, as described above. The bottom resist (LOR3B) is a so-called lift-off resist. It will also dissolve during the developing step, but at a larger rate than the top resist, creating an undercut, see Fig. 3.1(d-f). After development a thin layer of metal is deposited onto the wafer, and then the resist is stripped off the wafer with a solvent called the remover. This process will take off the metal which was deposited onto the resist layer, leaving the metal on the wafer behind. The undercut will help facilitate lift-off, because it causes the metal deposited onto the wafer surface and the metal deposited onto the resist to disconnect.

3.1.2 Electron-beam lithography

The smaller features in my design were fabricated with electron-beam lithography. This technique allows for much smaller feature sizes (with a spot size down to 4 nm for the JEOL JBX-9300FS system installed in the Chalmers cleanroom) and larger flexibility, as no separate mask need to be fabricated. The process is very similar to photolithography, but instead of exposing the resist with UV light, the resist gets exposed by the electron beam. The beam uses an acceleration voltage of 100 kV and can be positioned and focused to the desired position on the wafer using a set of electrostatic and magnetic “lenses”. The resist (ZEP-520A) is exposed with a dose of $150 \mu\text{C cm}^{-2}$. The writing process is divided into different steps during which a different spot size and current is used. The larger parts are written with a relatively large spot size and a current of 70 nA. The structure where a better resolution is needed, use a small spot size and a current of 2 nA is used. Given that we need to reach a fixed dose, it is easy to understand that the smaller current and step size will be slower to write, so the pattern has to be divided properly in order to minimize the total write time.

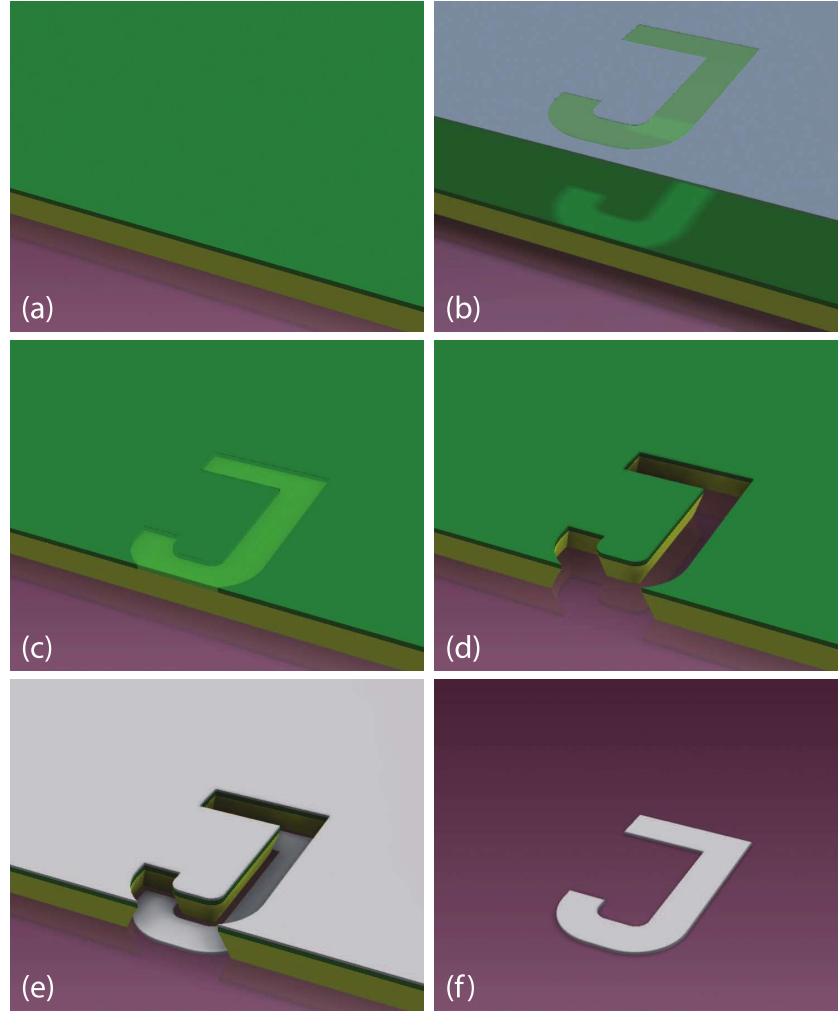


Figure 3.1: Cross-sectional view of the photolithography lift-off process. (a) Two layers of resist are deposited, a layer of lift-off resist (yellow) and a layer of photoresist (green). (b) A Chromium mask is used to selectively expose the resist. (c) The exposed resist now has the pattern transferred onto it. (d) The developer dissolves the exposed resist because a positive resist is used. The bottom resist dissolves at a larger rate creating an undercut. (e) Metal is evaporated on the wafer. (f) The remaining resist is stripped using a remover to lift-off the excess metal. The final remaining structure is the copy of the photomask because we used a positive resist and a lift-off process.



3. EXPERIMENTAL TECHNIQUES

We also have to take care of the proximity effect which will limit the achievable resolution by partially exposing unwanted areas near the edges of the pattern due to electron backscattering. Conversely parts in the middle of the pattern will receive a larger than expected dose due to the accumulated electron backscattering of the regions around it. These effects are mitigated by dividing the pattern into a grid and using a script (PROXECCO) to vary the deposited dose for each grid element, such that the proximity effect is correctly accounted for.⁶⁵ After the exposure step, processing is very similar as for photolithography, with a development step and further processing consisting of deposition or etching steps.

3.1.3 Two-angle evaporation

The experiments in this thesis depend strongly on the Josephson junction, as discussed in the previous chapter. The Josephson junction is a weak link between two superconductors. We use a technique called the two-angle evaporation (also known as shadow evaporation or Dolan bridge technique) to fabricate Josephson junctions, and by extension SQUIDS.⁶⁶ It is a variation of the lift-off process described before and is shown in Fig. 3.2. We start with a double resist layer as before and we use electron-beam lithography to expose the desired pattern. The pattern will now contain narrow lines in the top resist, which after development will be free hanging due to the large undercut. In the next step we evaporate the first metal layer (aluminium in my case) under an angle. This will have as a result that the free hanging bridges create a shadow which is offset from the original pattern. The aluminium is then exposed to oxygen, such that an oxide layer, covering the aluminium, is formed. We then evaporate aluminium under the opposite angle, displacing the pattern in the opposite direction. Finally the resist is removed and the unwanted metal is lifted off. In Fig. 3.2(h), we see a blowup of the junction itself. We can see that there is an overlap between the two metal layers, with a layer of oxide between the two. By varying the angle of evaporation and the height of the bottom resist we can control the overlap of the junctions and thus also their area. The oxidation parameters can in addition to the area be used to adjust the junction resistance. Note that the size of the SQUID loop will also depend on the evaporation angle and the pattern has to be adjusted accordingly. Care has to be taken such that the evaporation angle isn't too large for a given undercut, avoiding that metal is evaporated on the sidewalls of the bottom resist.

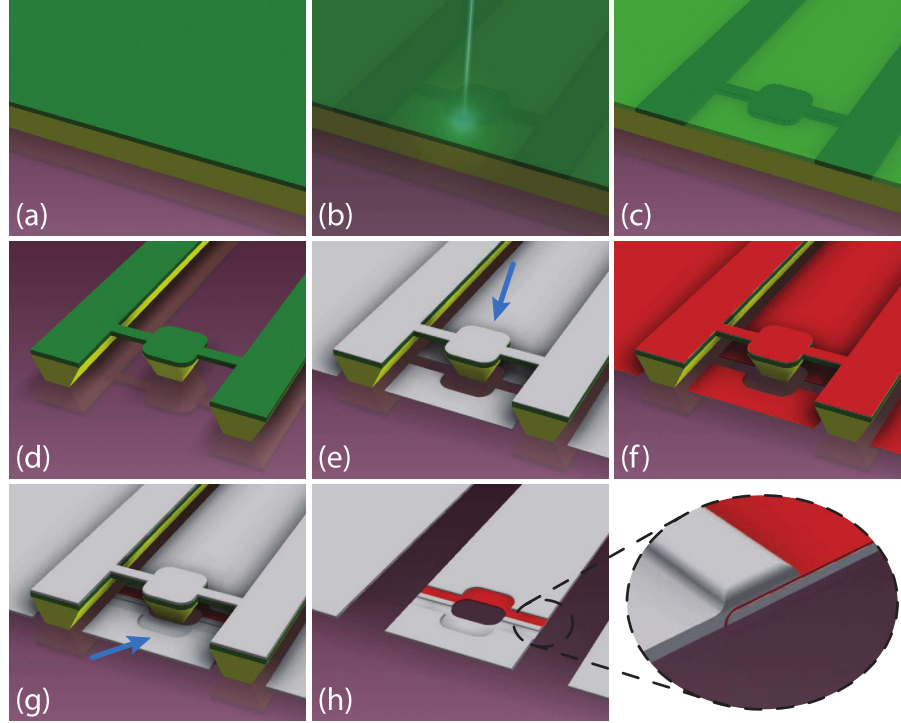


Figure 3.2: Cross-sectional view of the electron-beam lithography and two-angle evaporation process. (a) Two layers of resist are deposited, a layer of lift-off resist (yellow) and a layer of photoresist (dark green). (b) The pattern is written using a focused beam of electrons. (c) The exposed resist now has the pattern transferred onto it. (d) The developer dissolves the exposed positive resist. The bottom resist dissolves at a larger rate creating an undercut. (e) Aluminium is evaporated on the wafer using a positive angle (marked by the arrow). (f) The aluminium is oxidized (red layer). (g) The second layer of aluminium is evaporated using a negative angle (marked by the arrow), creating an overlap. (h) The remaining resist is stripped using a remover to lift-off the excess metal. The blow up shows the Josephson junction, formed by the two aluminium layers separated by the oxide.



3.2 Measurement techniques

3.2.1 Cryogenics

Dilution Cryostat

All the measurements presented in this thesis are performed at cryogenic temperatures. The sample is typically cooled to approximately 10 to 50 mK. A dilution cryostat is used to achieve these low temperatures. The cooling process in a dilution cryostat is based on the phase separation which occurs in a $^3\text{He}/^4\text{He}$ -mixture, when it is cooled down below 0.7 K, see Fig. 3.3.⁶⁷ This phase separation divides the liquid in a nearly pure ^3He -phase (the concentrated phase) and a denser ^3He -poor phase (the dilute phase) that consists of 6.6% ^3He and 93.4% ^4He at 0 K. The two phases behave similar as oil on water, with the concentrated phase “floating” on top of the dilute phase. The cooling process happens in the mixing chamber, by “evaporation” of ^3He across the phase boundary from the concentrated phase into the dilute phase. This process is driven by the continuous removal of ^3He from the dilute phase, by means of a distillation process, occurring in the still. The still is connected to the dilute phase in the mixing chamber by a small tube. The still is electrically heated to around 0.7 K and because of the much larger vapor pressure of ^3He to ^4He mostly ^3He will evaporate from the still. This will disturb the concentration balance in the dilute phase and ^3He will be forced to cross the phase boundary, to replenish the ^3He removed from the still. To ensure the continuity of the cooling process we have to replace the ^3He in the concentrated phase. This is done by circulating the ^3He which is removed at the still, to the cryostat. The gas is first cooled to around 4 K and then reliquefied by either a ^4He bath and a 1 K pot (in a wet cryostat) or by a pulse-tube cryocooler (in a dry cryostat). It is then cooled further on its way down to the mixing chamber by heat exchangers at the different temperature stages. At the still a flow impedance is installed in the He down line in order for the ^3He pressure to be high enough for condensing.

The primary cooling of the reintroduced ^3He gas is thus achieved by a 1 K pot in a wet cryostat. This works by the evaporative cooling of ^4He . The ^4He is funneled into the 1 K pot from the surrounding ^4He bath and then a pump is used to lower the pressure and achieve the forced evaporation. The flow into the 1 K pot is controlled by means of a needle valve. The sample and dilution unit are isolated from the environment by the surrounding bath of ^4He and the inner vacuum chamber (IVC).

Pulse tube cryocooler

In a dry cryostat the primary cooling comes is provided by a pulse tube cryocooler, see Fig. 3.4.^{68,69} The working principle of a cryocooler is explained in Fig. 3.4(a) and is based on the adiabatic compression and expansion of ^4He . A pulse tube consists of a number of different parts. From left to right we

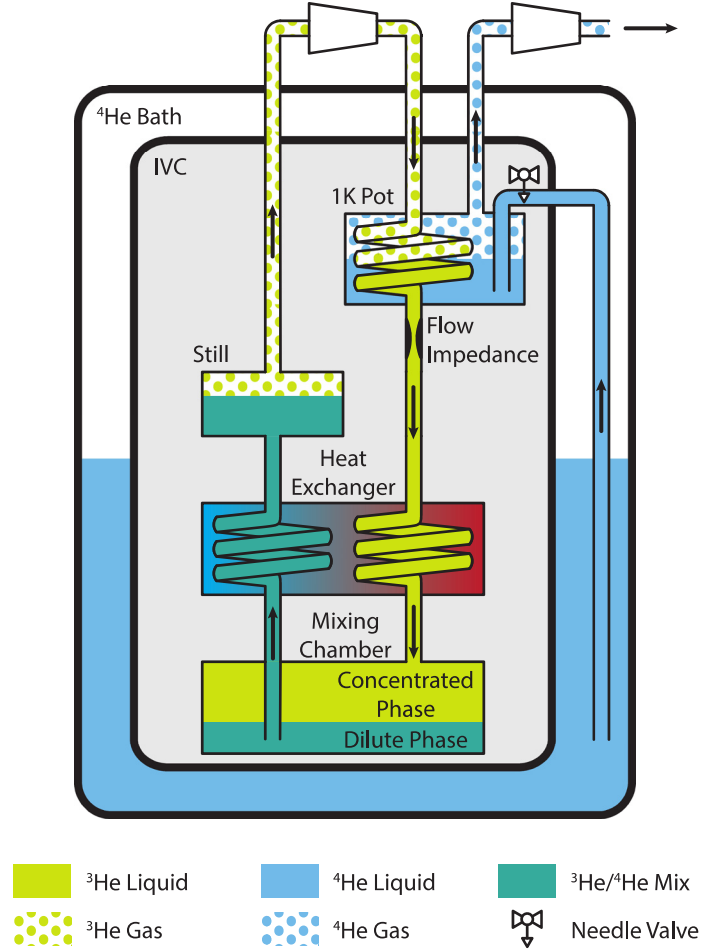


Figure 3.3: The dilution cryostat. Our experiments are performed at approximately 10 mK. In order to achieve these temperatures a $^3\text{He}/^4\text{He}$ -mixture is circulated in a closed loop in the dilution unit. The circulation works as follows. In the still, ^3He is pumped out of the dilute phase in a distillation process. This will disturb the concentration balance in the dilute phase and force ^3He to cross from the concentrated-to the dilute phase in the mixing chamber. This “evaporation” across the phase boundary costs energy and provides thus cooling power at the mixing chamber. The ^3He which is pumped out at the still is then circulated as gas at the other side of the dilution unit. In a wet cryostat the gas is first cooled by the ^4He bath and then recondensed in the 1 K pot. The liquid ^3He is then cooled further using heat exchangers before it reaches the mixing chamber again. A flow impedance is installed at the still to ensure that the ^3He pressure is high enough for condensing. The cooling power at the 1 K pot is the result of the evaporative cooling of ^4He which is funneled out of the surrounding bath. The flow is controlled by means of a needle valve. The dilution unit is isolated from the bath by the inner vacuum chamber (IVC).



3. EXPERIMENTAL TECHNIQUES

have a warm heat exchanger (X_1), a regenerator, a cold heat exchanger (X_2), a thermally isolated tube, called the pulse tube, another warm heat exchanger (X_3), an orifice, and a buffer tank. The system is driven by oscillating the pressure (P_{osc}) at the warm side of the regenerator. This can either be done by a moving piston or by a rotating valve which connects the system alternatingly between the high and low pressure side of a compressor. The former is called a Stirling-type pulse tube, whereas the latter is called a Gifford-McMahon-type pulse tube.

The cooling process in a pulse tube can be explained as follows. First we look at the region around heat exchanger X_3 , including the buffer. At this heat exchanger gas will only enter the pulse tube when the pressure in the pulse tube is smaller than the pressure in the buffer, $P_t < P_b$. The gas entering the pulse tube will now be at temperature T_H . When the pressure is increased at the other side of the pulse tube, gas will keep entering the tube until the pressure equals the buffer pressure, $P_t = P_b$. As the pressure keeps rising, gas will flow back into the buffer. The temperature of the gas leaving the tube will now be higher, $T > T_H$, as the gas entered the tube with a temperature T_H when $P_t < P_b$ and leaves the tube when $P_t > P_b$. As a result heat will be given off in X_3 to the environment. We can give a similar explanation for the region around heat exchanger X_2 . Here gas will enter the pulse tube at a temperature T_L from the regenerator and leave the tube when the pressure is decreased. As a result the gas flowing out will be colder, $T < T_L$, and heat is absorbed from the heat exchanger, providing cooling. It can be shown that the heat flow into X_2 equals the heat flow out of X_3 . For X_1 , the heat exchanger on the warm side of the regenerator, it can be shown that the heat flow out equals the power input to the compressor. Note that heat exchanger X_1 in a Gifford-McMahon-type pulse tube is dissipated in the compressor in the form of water cooling.

A regenerator consists of a porous matrix through which gas can flow. Its function is to gradually cool down the gas flowing from the warm to the cold side during compression, by absorbing and storing the heat. Similarly the gas flowing in the other direction during the other half of the cycle is heated up by releasing the stored heat. For this purpose an ideal regenerator tries to match the following conditions as well as possible: the flow impedance should be close to zero; the heat capacity per unit volume should be much larger than that of the gas; the heat contact between the gas and the regenerator should be as high as possible; and the heat conduction in the matrix in the direction of the flow should be zero. These partly conflicting requirements are difficult to meet and subject to advanced study. The function of the orifice and buffer is to allow for a flow into and out of the pulse tube at the warm side. Without this the cooling during the adiabatic expansion at the cold side would be canceled out during the compression part of the cycle. The orifice restricts the flow and ensures a nearly constant pressure in the buffer. Finally the task of the pulse tube is to isolate the cooling process at its cold side from the heating process at its warm side. To this effect the pulse tube is dimensioned such

that the gas cell in the middle of the tube (marked by the green dashed box in Fig. 3.4(a)) never comes in contact with either ends. The gas cell plays a similar role to the displacer in a Gifford-McMahon cooler. It is important that there is no turbulence in the tube to ensure the isolation effect.

In order to reach temperatures low enough for the condensation of the mixture a double-stage Gifford-McMahon-type pulse tube cryocooler is used in our dry dilution cryostats, see Fig. 3.4(b). The pressure oscillation comes from a rotating valve, operating between 1 Hz and 2 Hz, connecting the regenerator to the compressor. It uses two pulse tubes working in parallel, which share a regenerator. The middle of the regenerator is anchored at the lowest temperature of the first pulse tube (approximately 50 K). This reduces the heat load of the regenerator on the second pulse tube, allowing it to reach lower temperatures (approximately 3 K). Note that the hot ends of both pulse tubes are at room temperature, such that the hot end of the second tube second tube doesn't present a heat load on the first one. In practical systems a secondary orifice is installed between the compressor side and the hot side of each pulse tube. This is to counteract the phase difference in the pressure oscillation between both sides of the pulse tube. This phase difference comes from the compressibility of the gas in the pulse tube.

When condensing, the $^3\text{He}/^4\text{He}$ -mixture is brought into thermal contact with the cryocooler at different levels. As the final temperature of the pulse tube cryocooler is at a higher than the temperatures reached in a 1 K pot found in a wet cryostat, a higher condensation pressure is needed in order to condense the $^3\text{He}/^4\text{He}$ -mixture.

3.2.2 Microwave measurements

The measurements I have performed are all in the microwave domain. We install the sample in a reflectometry setup at the mixing chamber stage of our cryostat. A typical setup is shown in Fig. 3.5. The setups were very similar in the two different cryostats that were used. These setups require a careful design of the microwave lines to manage the noise seen by the sample. For this purpose a series of attenuators are installed, distributed over the different temperature stages. This way the black-body radiation from the higher temperatures stages will be attenuated down the lines. The attenuators of course inject noise into the line, but only at a power proportional to their temperature. The attenuators also dissipate the signal on the way down and the dissipated power will act as a thermal load on the cryostat. The available cooling power at each stage as well as the temperature difference between the stages will be different. Keeping these constraints in mind it is still possible to distribute the attenuators over the different stages, such that the noise in the line is approximately equal to the vacuum noise at the sample without heating up the different temperature stages significantly. The microwaves lines on the way down are UT-034 cables (with an outer diameter of 0.86 mm). The inner conductor is silver-plated CuNi and the outer conductor is CuNi.



3. EXPERIMENTAL TECHNIQUES

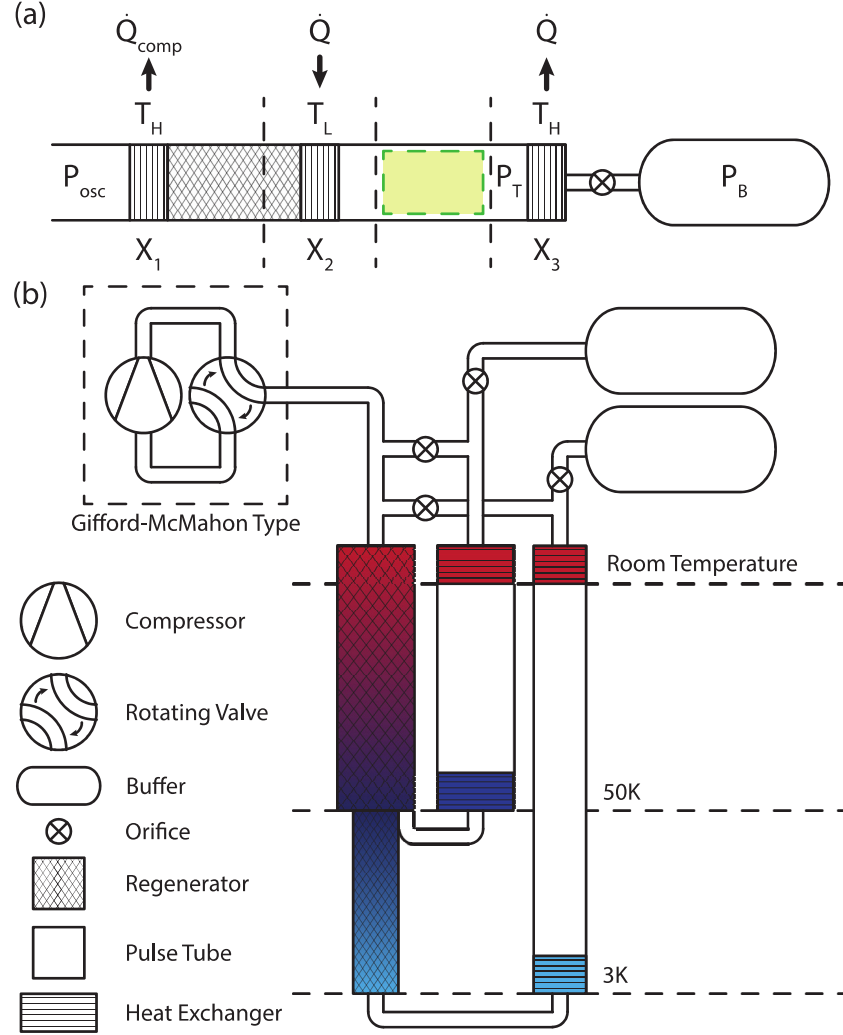


Figure 3.4: The pulse tube cryocooler. (a) Schematic overview of a pulse tube. A pulse tube consists of a number of different parts. From left to right we have a warm heat exchanger (X_1), a regenerator, a cold heat exchanger (X_2), a thermally isolated tube, called the pulse tube, another warm heat exchanger (X_3), an orifice, and a buffer tank. The green dashed volume of gas never leaves the pulse tube and thus isolates the processes at the ends. (b) The double-stage Gifford-McMahon-type pulse tube cryocooler, as used in most commercial dry dilution cryostats. Note that the hot ends of both pulse tubes are at room temperature, such that the second tube doesn't present a heat load on the first one. The secondary orifices, installed between the compressor side and the hot side of each pulse tube, are present to counteract the phase difference in the pressure oscillation between both sides of the pulse tube

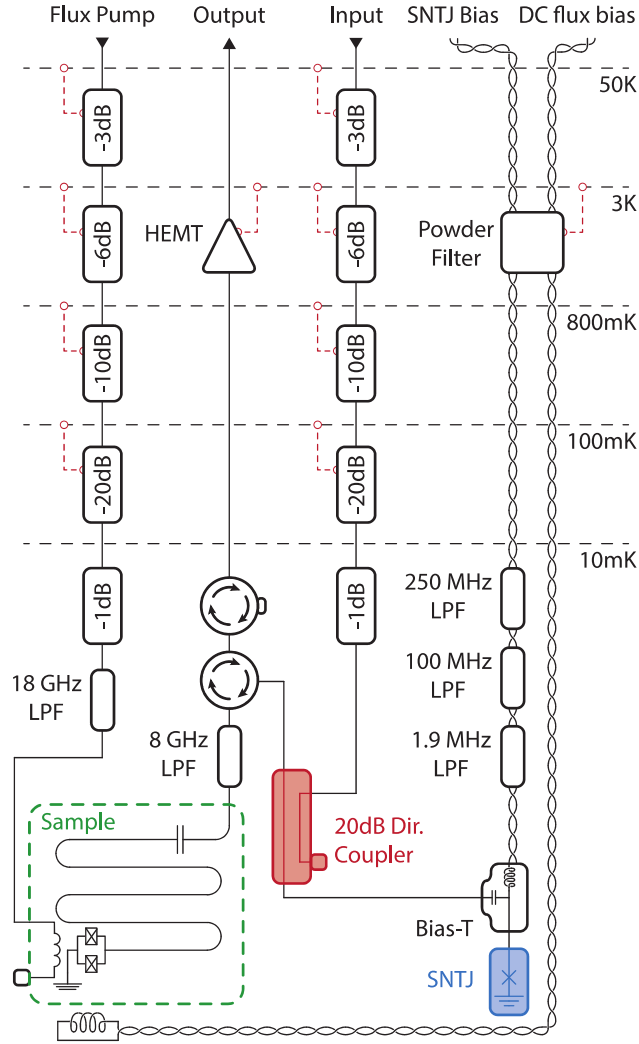


Figure 3.5: A detailed view of a reflection measurement setup. This setup is the one used in the parametric amplification results, a very similar setup without the SNTJ was used for the experiments on the DCE. The microwave frequency signals are sent down the cryostat with coaxial lines. These lines are attenuated at the different temperature stages in order to reduce the room temperature radiation and to thermalize the cables to the different temperature. The incoming and outgoing signals are separated from each other with a circulator. A second circulator is terminated with a 50Ω and isolates the sample from any radiation coming down from the low-noise HEMT amplifier. To allow for a noise calibration the output of a SNTJ, colored blue, is combined with the incoming signal in a directional coupler, colored red. The SNTJ is biased with a filtered superconducting twisted pair and bias-T. Another twisted pair is used to DC flux bias the experiment. A third microwave line, labeled flux pump, is used to modulate the flux through the SQUID in the experiments.



3. EXPERIMENTAL TECHNIQUES

In a reflectometry measurement a signal is reflected off the sample and the reflection coefficient is analyzed. We typically use a 4 to 8 GHz circulator to separate the incoming and outgoing signal. A second circulator, terminated with 50Ω , is installed between the sample and the cryogenic low noise HEMT amplifier (a Low Noise Factory LNF-LNC4_8A with a factory measured noise temperature $T_N = 1.8\text{ K}$) at the 3 K/4.2 K-stage, in order to absorb any radiation coming down the amplifier line. Additional filtering is installed in the form of an 8 GHz low-pass filter installed in front of the sample, with the goal to filter out any noise above the cutoff frequency of the circulators. When the signal is taken out of the cryostat, additional room temperature amplifiers are used before we feed the signal into the measurement equipment. The noise performance of amplifiers can be expressed by their noise temperature. This is the temperature a 50Ω input resistor would need to have to produce the same noise power at the output of amplifier, assuming the amplifier is perfect. The low-noise HEMT amplifier has a noise temperature $\sim 2\text{ K}$. This is important as the noise performance of a chain of amplifiers is largely determined by the first amplifier.³⁸

$$T_{N,\text{chain}} = T_{N,1} + \frac{T_{N,2}}{G_1} + \frac{T_{N,3}}{G_1 G_2} + \dots \quad (3.1)$$

This means that the following amplifiers only contribute to the total noise temperature, with their noise temperature divided by the power gain of the amplifiers preceding it. This also shows that it is imperative that the attenuation between the sample and the amplifier is kept to an absolute minimum. Any attenuation will raise the total noise temperature as it will act as an amplifier with a gain $G < 1$. For this reason the coax cable up to the first amplifier are made of superconducting NbTi.

In Paper A, I present measurements on the statistical properties of the produced radiation resulting from the dynamical Casimir effect. To do this it is necessary to measure the quadratures of the field at two different frequencies simultaneously. To achieve this we split the microwave signal coming out of the cryostat after amplification and feed it into two Aeroflex microwave digitizers. These digitizers perform a heterodyne measurement to measure the I and Q quadrature. Inside the digitizer the signal gets mixed down with a local oscillator to an IF frequency of $f_{\text{IF}} = 187.5\text{ MHz}$. For experiments on the dynamical Casimir effect it is crucial that only the frequency content of symmetrically offset frequencies from half the pump are measured. To filter out the response at the image frequency we use an image-rejection filter (a sharp bandpass filter) on the input. This setup relies on the fact that the amplifier noise is uncorrelated between different frequencies. The setup is shown in Fig. 3.6.

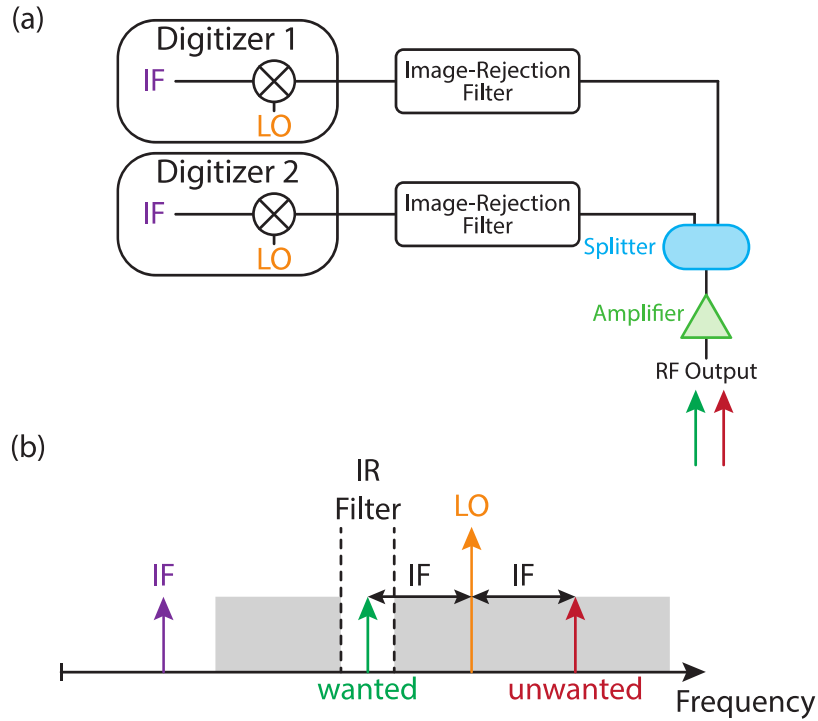


Figure 3.6: (a) The room temperature two-mode squeezing setup. The signal gets split after amplification before being fed into two digitizers. Two image rejection filters, filter out the unwanted part of the noise. (b) When mixing with a frequency $f_{LO} = f_s + f_{IF}$ any signal at frequency f_s gets mixed down to the IF frequency. The noise at $f_{LO} + f_{IF}$ will however also end up at the IF frequency. The image-rejection filter is a sharp bandpass filter installed at the input of the digitizer to filter out the unwanted noise before mixing.



3.3 Noise calibration

If we are interested in the noise performance of a device, it is needed to calibrate the microwave measurement setup, such that the noise generated by the device can be separated from the system noise. The system noise, which is the noise added by the setup, can be calibrated with the use of a controlled primary noise source. Such a noise source injects a well defined amount of noise depending on a user-controllable parameter. It is possible to separate the system noise from the noise injected by the noise source, if we then measure the noise at the output of the measurement setup as a function of this parameter. At the same time it is possible to calibrate the gain of the measurement setup. One example of such a primary noise source is the so-called hot-cold load. A switch is used to connect one of two matched impedances, which are kept at two different well-defined temperatures, to the input of the measurement setup. The noise injected by these impedances is Johnson-Nyquist noise, which depends on the temperature. If the temperature of the impedances is known accurately, it is possible to use such loads to calibrate the measurement setup. This method is also referred to as a Y-factor method.³⁸ In our measurements, see Paper C, we have used another primary noise source, known as a Shot-Noise Tunnel Junction (SNTJ).

3.3.1 Noise calibration setup

The SNTJ is a $50\,\Omega$ aluminum-aluminum oxide-aluminum junction. The junction is kept normal by means of a permanent magnet installed in the enclosure of the junction.⁷⁰ The calibration relies on the principle of measuring the noise of such a junction as a function of the bias voltage applied to the junction. More specifically we are interested in measuring the current noise spectral density $S_I(V, T)$ as it crosses over from the Johnson-Nyquist regime (where $S_I = 4k_B T / R_{\text{SNTJ}}$, for $V = 0$) to the shot noise regime (where $S_I = 2eI$, for $eV \gg k_B T$). The full expression of the current noise spectral density at low frequency is:⁷⁰

$$S_I(V, T) = \frac{2eV}{R_{\text{SNTJ}}} \coth\left(\frac{eV}{2k_B T}\right) = 2eI \coth\left(\frac{eV}{2k_B T}\right), \quad (3.2)$$

where R_{SNTJ} is the resistance of the SNTJ, T is the temperature and V is the voltage across the junction. Measuring the noise at zero bias and at least in 2 points in the shot-noise dominated regime, will allow us to calibrate the gain and noise temperature of the measurement chain, making shot noise thermometry a good primary thermometry technique.

However, as we are dealing with temperatures $T \ll \frac{hf}{k_B}$, where f is the measurement frequency, we will need to account for the zero-point fluctuations. The formula for the current spectral density of the noise of the SNT becomes

then:⁷¹

$$S_I(f, V, T) = \frac{1}{R_{\text{SNTJ}}} \left((eV + hf) \coth \left(\frac{eV + hf}{2k_{\text{B}}T} \right) + (eV - hf) \coth \left(\frac{eV - hf}{2k_{\text{B}}T} \right) \right). \quad (3.3)$$

From here on we will use Eq. (3.3) to calculate the noise.

We measure the power at room temperature with a chain of amplifiers and a digitizer. The complete expression for the total noise power becomes:

$$\begin{aligned} P_{\text{N}}(f, V, T) &= G \cdot BW \cdot k_{\text{B}} \left[T_{\text{N}} + \frac{R_{\text{SNTJ}} \cdot S_I}{4k_{\text{B}}} \right] \\ &= G \cdot BW \cdot k_{\text{B}} \left[T_{\text{N}} + \frac{1}{4k_{\text{B}}} \left((eV + hf) \coth \left(\frac{eV + hf}{2k_{\text{B}}T} \right) + (eV - hf) \coth \left(\frac{eV - hf}{2k_{\text{B}}T} \right) \right) \right]. \end{aligned} \quad (3.4)$$

Here G is the gain of the measurement chain, BW is the measurement bandwidth, T_{N} is the noise temperature of the measurement chain. Note that in Eq. (3.4) we assumed that the SNTJ impedance is perfectly matched with the measurement setup. I have plotted this expression and the simplified classical version, derived using Eq. (3.2), in Fig. 3.7.

The SNTJ is biased with a filtered twisted pair of DC wires using a bias-T. At room temperature there is a bias resistor of $R_{\text{b}} = 100 \text{ k}\Omega$ in series with the twisted pair. Given that this resistance is much higher than the resistance of the junction, one can calculate the bias current across the junction I_{b} as follows:

$$I_{\text{b}} = \frac{V_{\text{b,RT}}}{R_{\text{b}}}, \quad (3.5)$$

where $V_{\text{b,RT}}$ is the bias voltage set at room temperature. The bias voltage across the junction $V_{\text{b,SNTJ}}$ is then simply calculated as follows:

$$V_{\text{b,SNTJ}} = I_{\text{b}} R_{\text{SNTJ}}. \quad (3.6)$$

The resistance of the SNTJ was measured in a separate 4-probe measurement and was found to be 52.5Ω . The necessity of a separate measurement of the SNTJ resistance can be avoided by using a 4-probe setup when performing the noise calibration, which allows for a direct measurement of $V_{\text{b,SNTJ}}$.

To calibrate the actual setup, we have to inject the generated noise into the measurement line. This can be done with a microwave switch, where the measurement line with the low-noise amplifier can be connected to either the sample or the SNTJ. In our experiments we have chosen to combine the output of the SNTJ with the incoming signal in a 20 dB-directional coupler, see Fig. 3.5, before reflecting the signal off the sample and sending it up the measurement line. During the calibration procedure, we make sure that the



3. EXPERIMENTAL TECHNIQUES

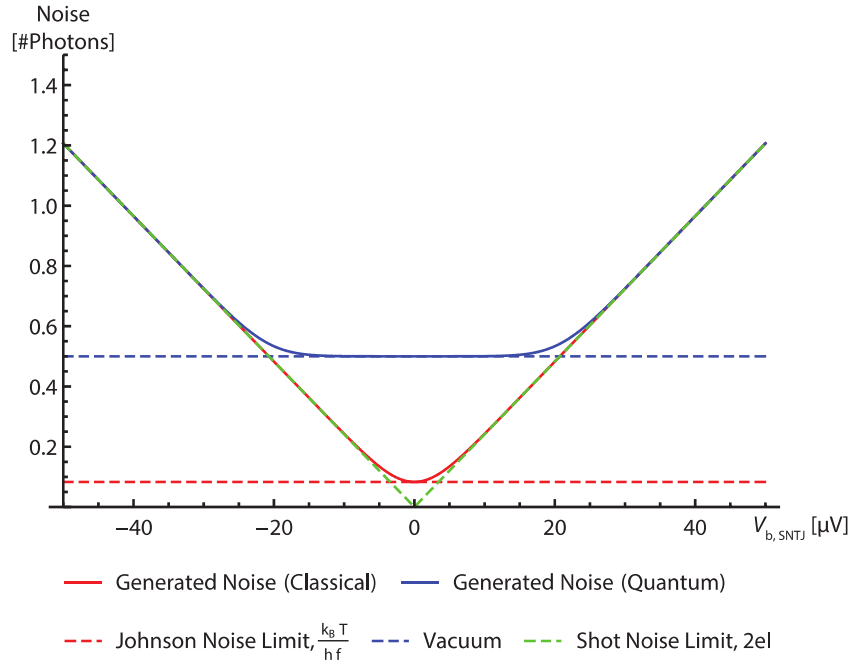


Figure 3.7: A calculation of the noise generated by the SNTJ as a function of the bias voltage, $V_{b,SNTJ}$, for a temperature $T = 20 \text{ mK}$, a SNT resistance of 50Ω and a measurement frequency of 5 GHz . These calculations include no contribution of the measurement chain (assuming $G = 1$ and $T_N = 0$). Both the classical result and the quantum result, Eq. (3.4), are plotted.

resonance frequency of the sample is tuned out of the band of interest, such that it reflects all the generated noise to the amplifier.

The measurement setup used at room temperature is described in Fig. 3.8(a). We bias the SNTJ using an arbitrary wave generator (AWG), and we sweep the voltage with a triangle wave at a frequency of 123 Hz. This allows us to average the measured noise curves, by triggering on the start of the waveform. The noise power generated by the SNTJ is amplified at room temperature with two amplifiers before passing an image-rejection filter. As described in the previous section, the digitizer performs a heterodyne measurement of the incoming signal by mixing the signal down with a local oscillator to an IF frequency of $f_{\text{IF}} = 187.5$ MHz. The image-rejection filter is then responsible to filter out the image frequency. The power measured by the digitizer follows Eq. (3.4), but as positive and negative bias voltages give the same noise power, the result is frequency doubled compared to the applied triangle wave, see Fig. 3.8.

Each triangle period is sampled with 4000 points, which gives a sampling frequency $f_{\text{samp}} = BW = 4000 \times 123 \text{ Hz} = 492 \text{ kHz}$. Note that the bandwidth BW is the same as f_{samp} , because we sample both quadratures. This means that positive and negative frequencies can be distinguished. For each measurement frequency I average 25000 periods together to get one noise power curve. We extract the Gain G , noise temperature T_{N} and temperature T as a function of frequency, by measuring these noise power curves at different measurement frequencies of interest (spaced 500 kHz apart) and fitting them using Eq. (3.4). Note that the BW is chosen to be smaller than the step in measurement frequency. The peak-to-peak amplitude of the bias voltage triangle wave is $V_{\text{b}} = 1 \text{ V}$ at the output of the AWG. This should give a peak-to-peak bias voltage on the SNT of $V_{\text{b,SNTJ}} = 1 \text{ V}/2000 = 500 \text{ }\mu\text{V}$. This is significantly larger than the voltage, V_{co} , at which the transition between the zero-point fluctuations and the shot-noise regime occurs, see Fig. 3.7:

$$V_{\text{co}} = \frac{hf}{e} = \frac{h \times 5 \text{ GHz}}{e} \approx 20 \text{ }\mu\text{V} < \frac{V_{\text{b,SNTJ}}}{2} = 250 \text{ }\mu\text{V}. \quad (3.7)$$

3.3.2 Calculation of the added noise

The noise calibration was used to quantify the noise performance of the multimode parametric amplifier, see Paper C. In principle we now have all the tools needed to calculate the amount of noise which the JPA adds. I will do this rigorously in number of photons, approximating the measurement chain according to Fig. 3.9. The components between the SNTJ and the JPA are represented as a single element with insertion loss factor $A_{\text{IL}} = 1/G_{\text{IL}} > 1$. The noise temperature ($T_{\text{N,IL}}$) and the number of added noise photons (N_{IL})



3. EXPERIMENTAL TECHNIQUES

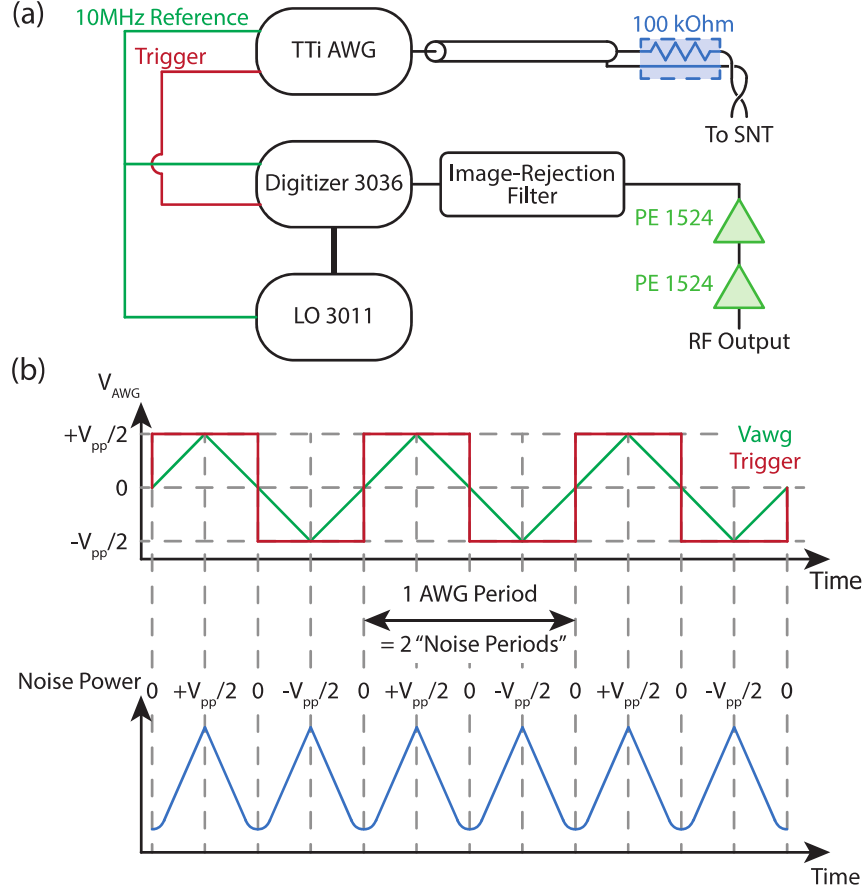


Figure 3.8: The waveform from the AWG is sent through a $100\text{ k}\Omega$ bias resistor, via a twisted pair and a bias-T. The RF measurement line coming from the cryostat is amplified with two room temperature amplifiers. We perform a heterodyne measurement with an Aeroflex digitizer and calculate the emitted shot-noise power. In order to filter out the image frequencies from the downconversion process in the digitizer we have used an image-rejection bandpass filter. The AWG and the digitizer share a 10 MHz reference and the AWG waveform trigger is also supplied to the digitizer to trigger the capture. The AWG is set to generate a triangle wave with a frequency of 123 Hz. The SNT will however generate noise curves at double this frequency (both positive and negative bias voltages generate the same output noise power). The digitizer is triggered on the rising edge of the AWG trigger signal and captures 4000 points per period, giving a sampling frequency of $4000 \times 123\text{ Hz} = 492\text{ kHz}$. This will be the bandwidth value used when fitting the noise power curves. For each measurement frequency I average 25000 periods together.

of such an element is given by:³⁸

$$T_{\text{N,IL}} = T_{\text{IL}} (A_{\text{IL}} - 1) \quad (3.8)$$

$$N_{\text{IL}} = \frac{1}{2} \coth \left(\frac{hf}{2k_{\text{B}} T_{\text{IL}}} \right) (A_{\text{IL}} - 1), \quad (3.9)$$

where T_{IL} is the physical temperature of the components causing the insertion loss. The JPA contributes to the chain with a gain G_{J} and added noise number N_{J} . When the JPA is turned off, $G_{\text{J}} = 1$ and $N_{\text{J}} = 0$ (this does assume that the unpumped JPA is strongly overcoupled). The effect of the rest of the measurement chain is abstracted in the element labeled “System”, with a total gain G_{SYS} and added noise of N_{SYS} .

We can now make an analysis of the signal-to-noise ratio (SNR) for the setup, both with the JPA turned on and off. The input noise into the measurement line is the noise generated by the unbiased SNTJ, which is essentially vacuum noise ($N_{\text{in}} = \frac{1}{2} \coth \left(\frac{hf}{2k_{\text{B}} T_{\text{SNTJ}}} \right) \approx 0.5$). As the insertion loss element is at the same physical temperature as the SNTJ, the total noise at the output of the insertion loss element, $N_{\text{out,IL}}$, is thus:

$$\begin{aligned} N_{\text{out,IL}} &= \frac{\frac{1}{2} \coth \left(\frac{hf}{2k_{\text{B}} T_{\text{SNTJ}}} \right) + N_{\text{IL}}}{A_{\text{IL}}} \\ &= \frac{\frac{1}{2} \coth \left(\frac{hf}{2k_{\text{B}} T_{\text{SNTJ}}} \right) + \frac{1}{2} \coth \left(\frac{hf}{2k_{\text{B}} T_{\text{IL}}} \right) (A_{\text{IL}} - 1)}{A_{\text{IL}}} \\ &= \frac{N_{\text{in}} + N_{\text{in}} (A_{\text{IL}} - 1)}{A_{\text{IL}}} \\ &= N_{\text{in}}. \end{aligned} \quad (3.10)$$

The effect is thus that the noise is unchanged, but any signal which has passed will be attenuated with a factor $1/A_{\text{IL}}$.

We can now calculate the output signal level (S_{out}) and output noise level (N_{out}) at the output of the whole chain, with the JPA off:

$$\begin{aligned} S_{\text{out},0} &= G_{\text{SYS}} \cdot \frac{1}{A_{\text{IL}}} \cdot S_{\text{in}} \\ N_{\text{out},0} &= G_{\text{SYS}} \left(N_{\text{SYS}} + \frac{1}{A_{\text{IL}}} (N_{\text{IL}} + N_{\text{in}}) \right) \\ &= G_{\text{SYS}} (N_{\text{SYS}} + N_{\text{in}}). \end{aligned} \quad (3.11)$$

We can do the same with the JPA on:

$$\begin{aligned} S_{\text{out,JPA}} &= G_{\text{SYS}} \cdot G_{\text{J}} \cdot \frac{1}{A_{\text{IL}}} \cdot S_{\text{in}} \\ N_{\text{out,JPA}} &= G_{\text{SYS}} \left(N_{\text{SYS}} + G_{\text{J}} \left(N_{\text{J}} + \frac{1}{A_{\text{IL}}} (N_{\text{IL}} + N_{\text{in}}) \right) \right) \\ &= G_{\text{SYS}} (N_{\text{SYS}} + G_{\text{J}} (N_{\text{J}} + N_{\text{in}})). \end{aligned} \quad (3.12)$$



3. EXPERIMENTAL TECHNIQUES

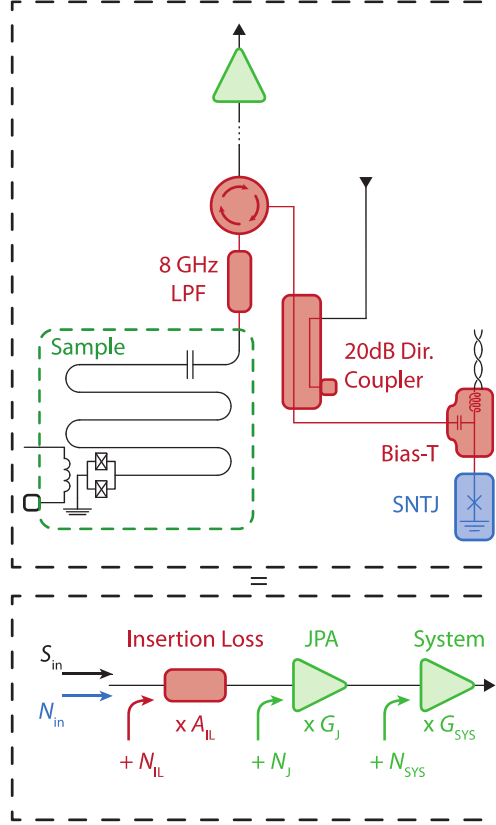


Figure 3.9: *Simplified schematic of the measurement chain and an analogue representation. We represent the loss of the components between the SNTJ and the sample by means of the insertion loss A_{IL} . The insertion loss will also add noise, represented by N_{IL} , which is referred to its input. The noise generated by the unbiased SNTJ is vacuum noise, represented by N_{in} , as the temperature of the SNTJ was calibrated to be close to 10 mK. The input signal is labelled as S_{in} . The JPA has a gain G_J and an added noise, referred to its input, of N_J . Finally the rest of the measurement chain is represented by the gain G_{SYS} and the added noise N_{SYS} . These two quantities are quantified in the noise calibration.*

Here S_{in} represents the input signal. From Eqs. (3.11) and (3.12), we can calculate the output SNR (SNR_{out}):

$$\begin{aligned}
 \text{SNR}_{\text{out},0} &= \frac{G_{\text{SYS}} \cdot \frac{1}{A_{\text{IL}}} \cdot S_{\text{in}}}{G_{\text{SYS}} (N_{\text{SYS}} + N_{\text{in}})} \\
 &= \frac{\frac{1}{A_{\text{IL}}} \cdot S_{\text{in}}}{N_{\text{SYS}} + N_{\text{in}}} \\
 \text{SNR}_{\text{out},\text{JPA}} &= \frac{G_{\text{SYS}} \cdot G_{\text{J}} \cdot \frac{1}{A_{\text{IL}}} \cdot S_{\text{in}}}{G_{\text{SYS}} (N_{\text{SYS}} + G_{\text{J}} (N_{\text{J}} + N_{\text{in}}))} \\
 &= \frac{G_{\text{J}} \cdot \frac{1}{A_{\text{IL}}} \cdot S_{\text{in}}}{N_{\text{SYS}} + G_{\text{J}} (N_{\text{J}} + N_{\text{in}})}. \tag{3.13}
 \end{aligned}$$

The SNR improvement ΔSNR is then:

$$\begin{aligned}
 \Delta\text{SNR} &= \frac{\text{SNR}_{\text{out},\text{JPA}}}{\text{SNR}_{\text{out},0}} \\
 &= \frac{G_{\text{J}} (N_{\text{SYS}} + N_{\text{in}})}{N_{\text{SYS}} + G_{\text{J}} (N_{\text{J}} + N_{\text{in}})} \\
 &= \frac{N_{\text{SYS}} + N_{\text{in}}}{\frac{N_{\text{SYS}}}{G_{\text{J}}} + N_{\text{J}} + N_{\text{in}}}. \tag{3.14}
 \end{aligned}$$

An example of how the signal and noise levels as well as the SNR evolves throughout the measurement chain, both with the JPA turned on and off, is shown in Fig. 3.10(a) and Fig. 3.10(b) respectively. The maximum SNR improvement possible happens when the $G_{\text{J}} \rightarrow \infty$ ($N_{\text{J}} \rightarrow 0.5$) and the input $T_{\text{SNTJ}} = 0$ ($N_{\text{in}} = 0.5$). In this case $\Delta\text{SNR} \rightarrow 0.5 + N_{\text{SYS}}$.

The input noise N_{in} is a quantity we get from the SNTJ calibration. The ΔSNR and the gain of the JPA are quantities which are extracted from the measurements. N_{SYS} is calculated from Eq. (3.11) using the measured value of $N_{\text{out},0}$:

$$\begin{aligned}
 N_{\text{out},0} &= G_{\text{SYS}} (N_{\text{SYS}} + N_{\text{in}}) \\
 N_{\text{SYS}} &= \frac{N_{\text{out},0}}{G_{\text{SYS}}} - N_{\text{in}}. \tag{3.15}
 \end{aligned}$$

$G_{\text{SYS}} = A_{\text{IL}} \cdot G_{\text{TOT}}$ is calculated from the total gain of the measurement chain G_{TOT} (from the SNTJ calibration, with the JPA turned off) and the insertion loss A_{IL} . With these numbers the noise added by the JPA can be calculated as.

$$N_{\text{J}} = N_{\text{SYS}} \left(\frac{1}{\Delta\text{SNR}} - \frac{1}{G_{\text{J}}} \right) + N_{\text{in}} \left(\frac{1}{\Delta\text{SNR}} - 1 \right) \tag{3.16}$$



3. EXPERIMENTAL TECHNIQUES

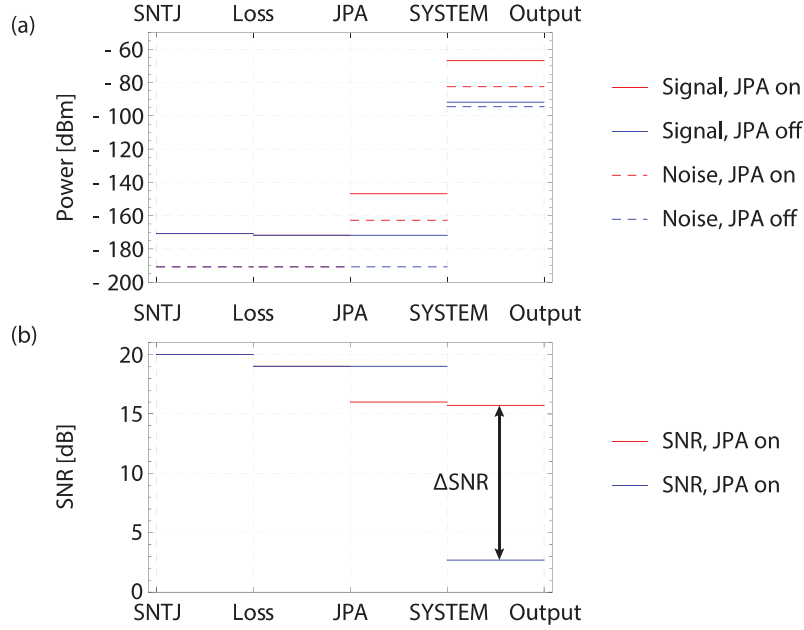


Figure 3.10: Evolution of (a) the signal and noise level and (b) the SNR throughout the measurement chain. The input SNR is 20 dB. $G_{\text{SYS}} = 80$ dB and $G_{\text{J}} = 25$ dB. The JPA is assumed to be quantum limited, $N_{\text{J}} = 0.5$, and $N_{\text{SYS}} = 20.8$. The insertion loss is 1 dB. We used an input noise level set by the temperature of 20 mK, a bandwidth of 50 Hz and a frequency of 5 GHz, when calculating the power levels. We assume that the JPA is quantum limited. The ΔSNR is marked in panel (b) and is 13.02 dB ($< \Delta\text{SNR}_{\text{max}} = 13.28$ dB).

4

Results

I have theoretically discussed the different parametric effects in Chapter 2. In this chapter I present the results of the appended papers, where I first discuss the dynamical Casimir effect. Next I discuss the parametric amplification where I show that we can reach quantum-limited performance for both the single-mode pumping scheme and the multimode pumping scheme. I also present some data where the pump is on resonance with mode 2, 3 and 4 at the same time. I then continue to present our first measurements on the intermode conversion in a multimode resonator, where the pump frequency is at the difference frequency of two modes, inducing a beam splitter like interaction between the modes. Finally I also discuss the measurements on the Mach-Zehnder interferometer, showing that the device performs qualitatively the same as in our simulations, with an on-off ratio as large as 45 dB.

4.1 The dynamical Casimir effect

The DCE has eluded experimental verification for more than 40 years, since the first proposals in 1970.¹⁵ A number of theoretical derivations have been made and I have discussed these in Section 2.4. In this section I will take a look at the experimental realization of the DCE and I will discuss the results found in Paper A a bit more in detail.

We have measured and observed the DCE in two different samples. These samples are made on a Si substrate, which is covered by a 400 nm thick layer of thermally grown SiO₂. The metal layer is all aluminum and is deposited in a two-angle evaporation process after patterning the double resist layer with e-beam lithography, see also Section 3.1. The two samples consist of a coplanar-waveguide transmission line which is shorted to ground by means of a SQUID. The length of the transmission line, counted from the taper onto the chip to the SQUID is different for the two samples and was 43 mm for sample 1 and 0.1 mm for sample 2. The difference is chosen to prevent



4. RESULTS

possible problem with stray resonances formed between the bonding wires and the SQUID. For these lengths, these resonances would fall firmly outside of the available measurement band of our setup. The normal resistance of the SQUID is $170\,\Omega$ and $218\,\Omega$ for samples 1 and 2 respectively. This gives an $L_{\text{sq}} = 180\,\text{pH}$ for sample 1 and $230\,\text{pH}$ for sample 2. The inductance of the SQUID can be modulated using an on-chip tuning line, which is shorted on the sample $20\,\mu\text{m}$ from the SQUID. The samples were bonded into a sample holder onto which an external coil was mounted for DC flux tuning. We have also checked that there is an isolation between the on-chip tuning line and the transmission line, which is terminated by the SQUID, which is larger than $50\,\text{dB}$.

The samples were installed in a wet dilution refrigerator (an Oxford Instruments Kelvinox-400 High Access) at the mixing chamber. The base temperature of the cryostat was approximately $25\,\text{mK}$. The samples are connected with a well-filtered superconducting coax line to the low-noise cryogenic HEMT amplifier (a Low Noise Factory LNF-LNC4_8A). The noise temperature of the setup has been verified in a separate measurement to be approximately $6\,\text{K}$. There is a well attenuated probe line for characterization of the sample, which is separated from the measurement line by means of a circulator. Another circulator installed between the sample and the amplifier is terminated with $50\,\Omega$ in order to provide extra isolation. We know from previous experiments that the radiation temperature at the sample is comparable with the physical temperature of the cryostat. The full setup is shown in Fig. 4.1.

The first measurements which are performed are reflection measurements on the SQUID as a function of DC magnetic flux. As the inductance of the SQUID changes periodically with flux, we look for a periodic pattern in the phase of the reflection coefficient, see Fig. 1 in the supplementary material of Paper A. We biased the SQUID at $\Phi_{\text{DC}} = -0.35\Phi_0$.

The next step is to modulate the SQUID inductance sinusoidally with a pump frequency f_p . We know from Eq. (2.77) that the maximum output power is expected at $f_p/2$, so to find a good pump frequency we record the output power at $f_p/2$ as a function of pump power, P_p , and frequency. This data is presented in Fig. 2 of the supplementary material of Paper A. Essentially we see that there is radiation produced over the whole available measurement band. In the results presented here the pump frequency was fixed at $10.3\,\text{GHz}$.

At this pump frequency we then proceed to measure the DCE radiation as a function of the detuning from half the pump frequency. We do this by sweeping the analysis frequency and record the output power with two digitizers simultaneously at symmetric frequencies around $f_p/2$, and this at different P_p . These outputs were measured up to a detuning of $\pm 850\,\text{MHz}$ (up to the maximum frequency of our digitizers of $6\,\text{GHz}$) is presented in Fig. 4.2. We can see that there is a clear symmetry in the output photon flux density between the positive and negative detuned frequencies. This is to be expected according to Eq. (2.77). The output does not show the expected

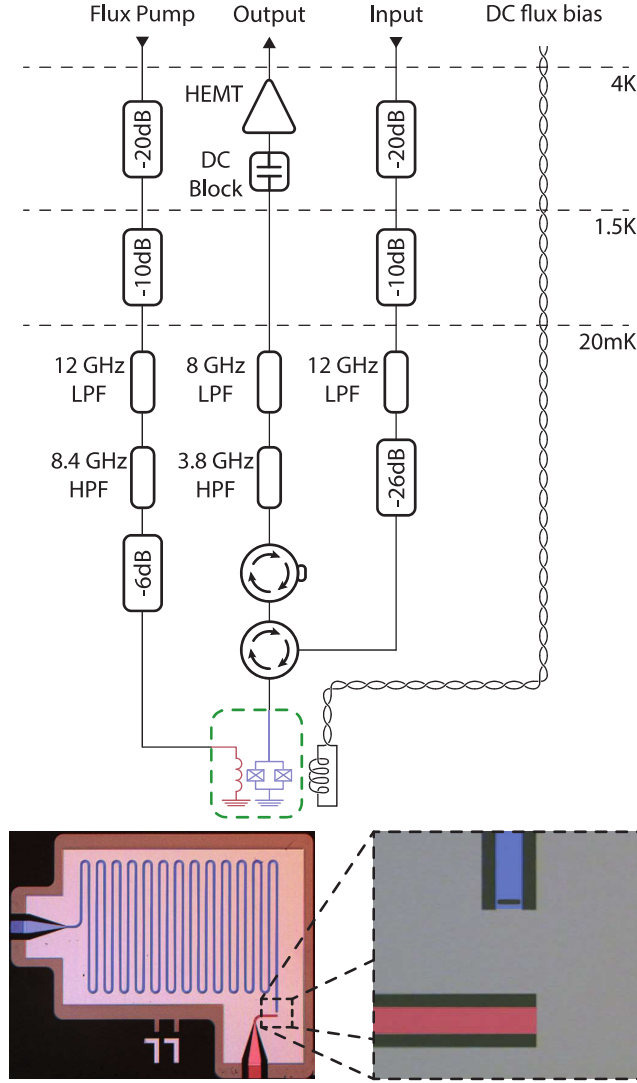


Figure 4.1: The microwave measurement setup. The DCE samples were installed at the mixing chamber of a wet dilution cryostat. The probe line down to the sample is attenuated with -56 dB. It is separated from the output by a circulator. An additional circulator, terminated with $50\ \Omega$, provides isolation from the noise of the amplifier line. There are filters installed to filter out any radiation falling outside of the circulator band. The amplifier is a cryogenic low-noise HEMT amplifier. Flux modulation of the SQUID at high frequency is done by means of an on-chip CPW transmission line shorted to ground $20\ \mu\text{m}$ from the SQUID. External DC flux biasing is done by means of an external coil mounted on the sample holder. The micrograph shows one of the samples with a $43\ \text{mm}$ long transmission line. The center line is marked in blue, whereas the flux tuning line is marked red.



4. RESULTS

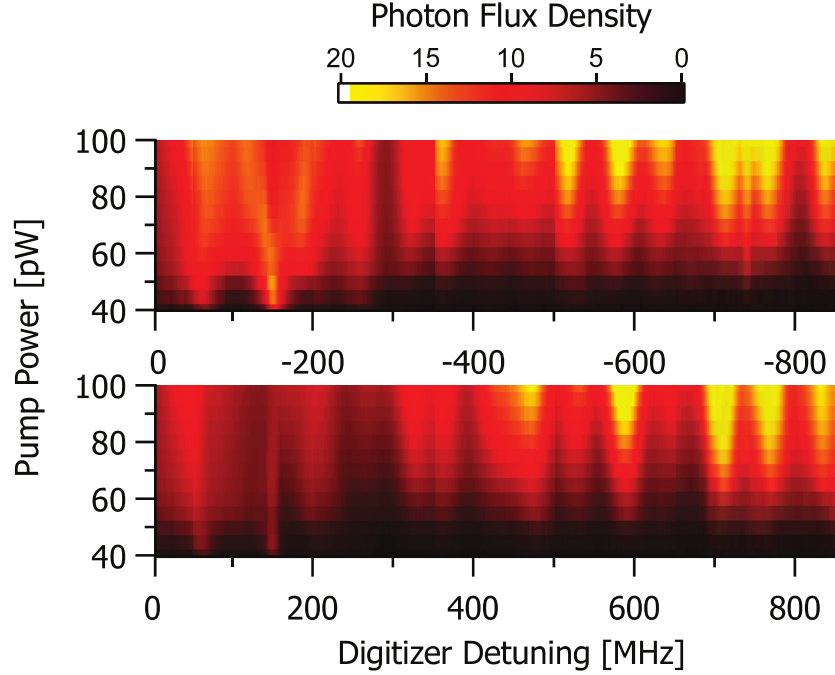


Figure 4.2: *Photon generation by the dynamical Casimir effect. These panels show the output photon flux density as a function of detuning from $f_p/2$ and pump power, P_p . The SQUID is modulated with $f_p = 10.3$ GHz and the radiation is produced symmetrically around $f_p/2$. The upper panel shows the measured photon flux density for negative detunings while the bottom panels show the results for positive detunings. The symmetry in the output spectrum with respect to $f_p/2$ is clearly visible. The corrugated structure can be explained by spurious resonance present in the measurement line.*

parabolic shape of the output spectrum. The reason for this is twofold. First, the measurement band of 1.7 GHz only a small region around the top of the parabola. On top of that we also see that there is clearly a corrugated structure in the output spectrum. This is because the mode density of the transmission line varies due to stray resonances in the transmission line. The parabolic shape is only valid when the mode density is flat, which is the case for an ideal transmission line. The output photon flux density increases with P_p . For pump powers, P_p , larger than 100 pW (referred to the sample) the output saturates. We assume that this is the point where the Josephson inductance saturates because the AC flux amplitude reaches $0.15\Phi_0$, such that the sum of the DC and AC flux reaches $0.5\Phi_0$, see Fig. 2e in Paper A.

Another signature of the DCE is two-mode squeezing. In Section 2.4.3 I discuss two-mode squeezing a bit more in detail. To calculate the amount of squeezing, we measure the quadratures at frequencies symmetric around $f_p/2$. We do this by splitting the signal after amplification in two different

4.2. PARAMETRIC AMPLIFICATION IN A MULTIMODE RESONATOR

microwave digitizers. When we do this we make use of the fact the noise of the amplifiers is uncorrelated between different frequencies. An important property is that the even though the two-mode squeezing increases with P_p , the individual modes remain unsqueezed. This is shown in Fig. 4.3(a) for a detuning of 588 MHz from $f_p/2$. The two-mode squeezing has a specific structure for the voltage correlators where $\langle I_+ I_- \rangle = -\langle Q_+ Q_- \rangle$, see Fig. 4.3(b) and $\langle I_+ Q_- \rangle = \langle I_- Q_+ \rangle$. The latter cross correlator can be made equal to zero by changing the pump phase. We have also measured the two-mode squeezing as a function of temperature and this for three different detunings from $f_p/2$ and a pump power of 100 pW.

Finally we have also measured the normalized second-order correlation function $g_{+-}^{(2)}$, see Eq. (2.81). In Fig. 4.5, we measure $g_{+-}^{(2)}$ as a function of pump power. The first digitizer is then set to $f_p/2 - 712$ MHz and the second digitizer is set to $f_p/2 + 712$ MHz. We then offset the second digitizer from this symmetric frequency to see $g_{+-}^{(2)}$ disappear. This shows that there is photon bunching between symmetric frequencies around $f_p/2$. The width of the peak is set by the bandwidth of the digitizers (10 MHz). Even though we see bunching, $g_{+-}^{(2)}$ never becomes larger than two, meaning that we have not observed the expected superbunching.

In conclusion we have measured the DCE in a transmission line terminated to ground with a SQUID. We observed broadband generation of radiation in a frequency span of 1.7 GHz centered around half the pump frequency. We have also measured the correlations in the noise measured symmetrically around $f_p/2$ and we have shown that the noise exhibits two-mode squeezing. These measurements are clear signatures of the DCE. What remains is to explicitly prove the non-classicality of the radiation and show the parabolic spectrum of the radiation.⁷²

4.2 Parametric amplification in a multimode resonator

In this section I will present the results from Paper C. In Section 2.2 I have treated phase-insensitive parametric amplification for both the degenerate and the nondegenerate case theoretically. We have performed careful noise calibrations to characterize the performance of the measurement chain according to the procedures described in Section 3.3

The parametric amplifier we used in Paper C is a quarter-wavelength resonator, terminated to ground using a SQUID. The CPW resonator has a length of 3 cm, giving it a bare resonance frequency (meaning neglecting the SQUID) of 959 MHz. This is substantially lower than the lower cutoff of our measurement setup, which is 4 GHz. The frequency was chosen such that several higher modes of the resonator fall within the bandwidth, allowing us to study multimode parametric effects. The spectrum of the resonator follows the



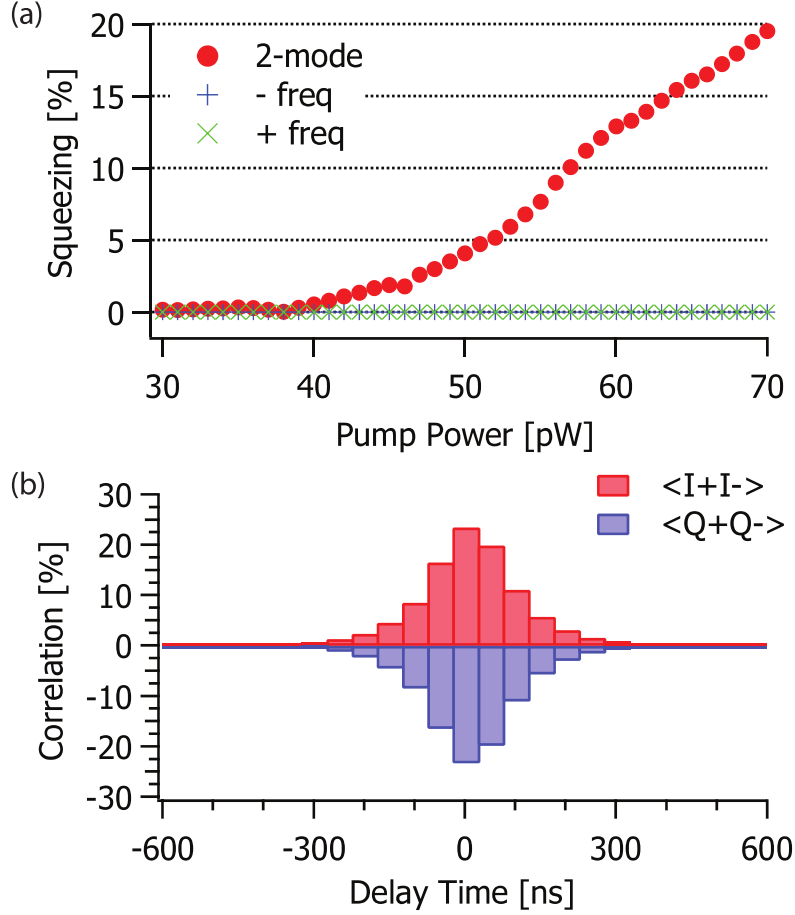


Figure 4.3: *Two-mode squeezing of the DCE radiation. (a) The two-mode squeezing of the field, measured with a detuning from $f_p/2$ equal to 588 MHz, as a function of P_p . The SQUID is pumped at $f_p = 10.3$ GHz. We see that the two-mode squeezing increases with pump power, while the individual modes remain unsqueezed. (b) The normalized cross-correlation $\langle I_+ I_- \rangle / P_{\text{avg}}$ and $\langle Q_+ Q_- \rangle / P_{\text{avg}}$, measured at a detuning from $f_p/2$ equal to 833 MHz. The cross-correlation reaches as high as 25% and clearly shows that $\langle I_+ I_- \rangle = -\langle Q_+ Q_- \rangle$ as predicted.*

4.2. PARAMETRIC AMPLIFICATION IN A MULTIMODE RESONATOR

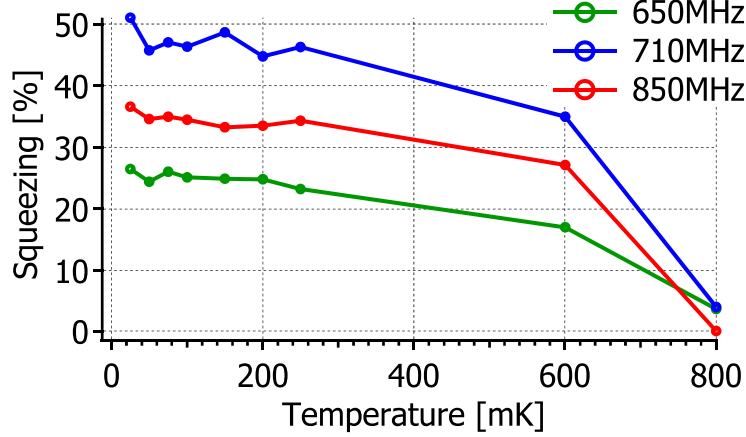


Figure 4.4: *Two-mode squeezing as a function of temperature. The two-mode squeezing of the field measured for three different detunings from $f_p/2$ as a function of temperature. The SQID is pumped at $f_p = 10.3$ GHz with a pump power of 100 pW. With increasing temperature, the two-mode squeezing starts to drop off.*

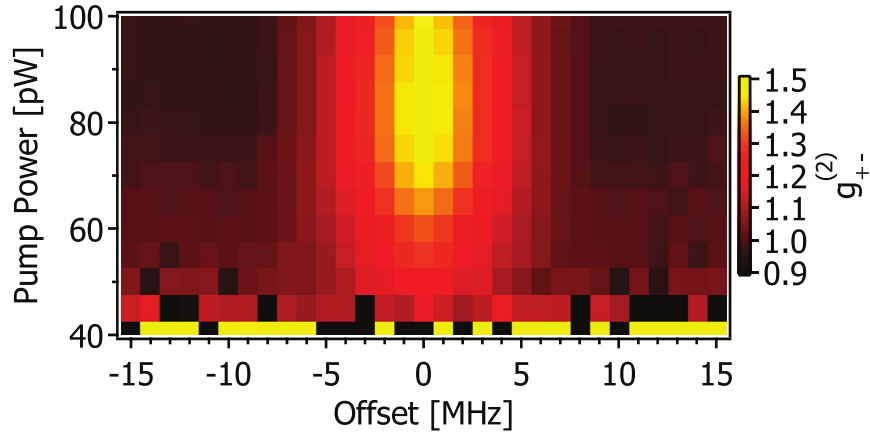


Figure 4.5: *The normalized second-order correlation function. We have performed measurements of the $g_{+-}^{(2)}$ function as a function of pump power and offset between the digitizers. At zero offset, the digitizers are detuned from $f_p/2 = 5.15$ GHz by ± 712 MHz. We then offset one of the digitizers from this symmetric frequency. This will lower the measured $g_{+-}^{(2)}$ and the width of the peak will be the bandwidth of the digitizers, 10 MHz. When increasing the pump power $g_{+-}^{(2)}$ rises, and although the radiation shows bunching it never becomes larger than two.*



4. RESULTS

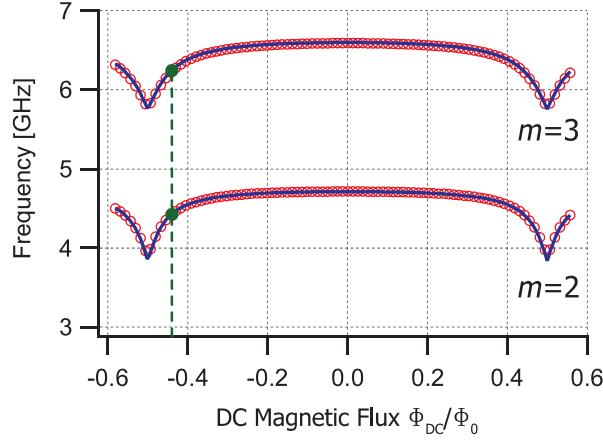


Figure 4.6: Measured resonance frequencies of the different modes ($m = 2, 3$) as a function of DC magnetic flux Φ_{DC} (red circles). At zero DC flux bias, the resonance frequencies of modes 2 and 3 are, respectively, 4.713 GHz and 6.588 GHz. The blue line is a fit to the mode resonance frequencies $f_m(\Phi_{\text{DC}})$. The resonances were fit simultaneously by numerically solving the characteristic Equation, see Eq. (2.38). Our Josephson parametric amplifier is operated by magnetic flux-pumping. This is achieved by applying an AC tone to the on-chip flux line, while keeping the DC flux constant at a fixed nonzero value. Our measurements are performed around a DC flux of $-0.44\Phi_0$, denoted by the green dashed line.

dispersion relation, see Eq. (2.38). The SQUID has a critical current of $1.65 \mu\text{A}$ which translates into a Josephson inductance of 200 pH . We have two modes, $m = 2, 3$, accessible in the measurement bandwidth and the dependence of the mode frequencies on the DC magnetic flux is shown in Fig. 4.6. Fitting the spectrum numerically with the dispersion relation allows us to extract a SQUID inductance participation ratio $\gamma = L_{\text{sq},0}/(L_0 d) = 1.76\%$. The capacitance participation ratio, $C_{\text{sq}}/(C_0 d)$, was found to be negligible. The resonator is coupled to the measurement line with an interdigitated coupling capacitor of $C_c = 53 \text{ fF}$. The internal damping rate of the resonator was found to be significantly lower than the coupling rate to the measurement line, meaning that the resonator is firmly overcoupled. The internal quality factor, Q^i was approximately 3750, independent of the mode number, whereas the external quality factor, Q^e was about 500 for mode 2 and 460 for mode 3. The sample was fabricated using the same techniques as the DCE samples. The sample consist of two-angle evaporated aluminum on top of intrinsic silicon. The patterning was done using electron-beam lithography, for more details see Section 3.1.

The sample was installed at the mixing chamber stage of a dry dilution cryostat (a Bluefors LD250) with a base temperature $< 10 \text{ mK}$. The measurement setup is shown in Fig. 3.5 and discussed in Section 3.2.2. The DC flux biasing is achieved in the same way as in the DCE measurements, using a

4.2. PARAMETRIC AMPLIFICATION IN A MULTIMODE RESONATOR

superconducting external coil mounted on the sample holder. For the AC flux tuning there is an on-chip transmission line which couples inductively to the SQUID. This flux pump line is terminated off-chip using a $50\,\Omega$ load. The line is also attenuated with 40 dB and filtered with an 18 GHz low-pass filter. The shot-noise calibration setup consists of a SNTJ mounted on the mixing chamber. It is combined with the signal line, which is attenuated with 40 dB on its way down to the mixing chamber, in a 20 dB directional coupler. The SNTJ is biased with a superconducting twisted pair through a Bias-T. The microwave-frequency noise is then fed into the directional coupler. The twisted pairs for the SNTJ and the DC flux biasing are filtered at the 3 K stage with a copper-powder filter.

When we perform the shot-noise calibration we are able to quantify the performance of the measurement chains in terms of its added noise and the total gain. We follow the method set out in Section 3.3 and we have extracted the added noise referred to the input of the JPA. As described above, the components between the SNTJ and the input of the JPA need to be taken into account. We have measured the attenuation of these components in a separate measurement and found it to be 1.75 ± 0.4 dB for the frequency range around mode 2 and 2.25 ± 0.4 dB for the frequency range around mode 3. We present the added noise referred to the input of the JPA, N_{SYS} , and the gain, G_{SYS} of the measurement setup in Fig. 4.7. These have been measured with the JPA turned off and tuned out of the frequency band of interest. We use the results of these measurements to analyze the performance of the JPA.

4.2.1 Single-mode parametric amplification

For the single-mode parametric amplification we have measured the gain, G_J , the signal-to-noise improvement, ΔSNR , and the change in the noise floor as a function of pump frequency, f_p , and pump power, P_p . The circuit is flux biased at $\Phi_{\text{DC}} = -0.44\Phi_0$ so that the resonance frequency of mode 2 is tuned down to 4.420 GHz. We measure the power spectrum in a 100 kHz wide band centered around our signal which is offset from $f_p/2$ with 100 kHz, so that we have nondegenerate amplification. Because of the offset between the signal frequency and $f_p/2$ this will be single-mode, phase-insensitive parametric amplification. We measure the signal gain, as well as the increase in the noise floor. Using these we can calculate the ΔSNR . We present G_J , ΔSNR and the minimum added noise N_J as a function of G_J in Fig. 4.8. We do this by calculating the added noise for each point in Fig. 4.8(a) and then retaining the points with the lowest noise for each 0.1 dB wide range of gain in Fig. 4.8(c). The maximum ΔSNR we reach is 10.5 dB. We see that the noise follows the quantum limit, see Eq. (2.39), nicely and that the added noise drops below 0.5 photons for low gain. The error bars are the result of the uncertainty on the insertion loss of the components between the SNTJ and the JPA.

We have also measured the G_J as a function of signal frequency with a vector network analyzer sweeping f_p and P_p . For each pump setting we sweep



4. RESULTS

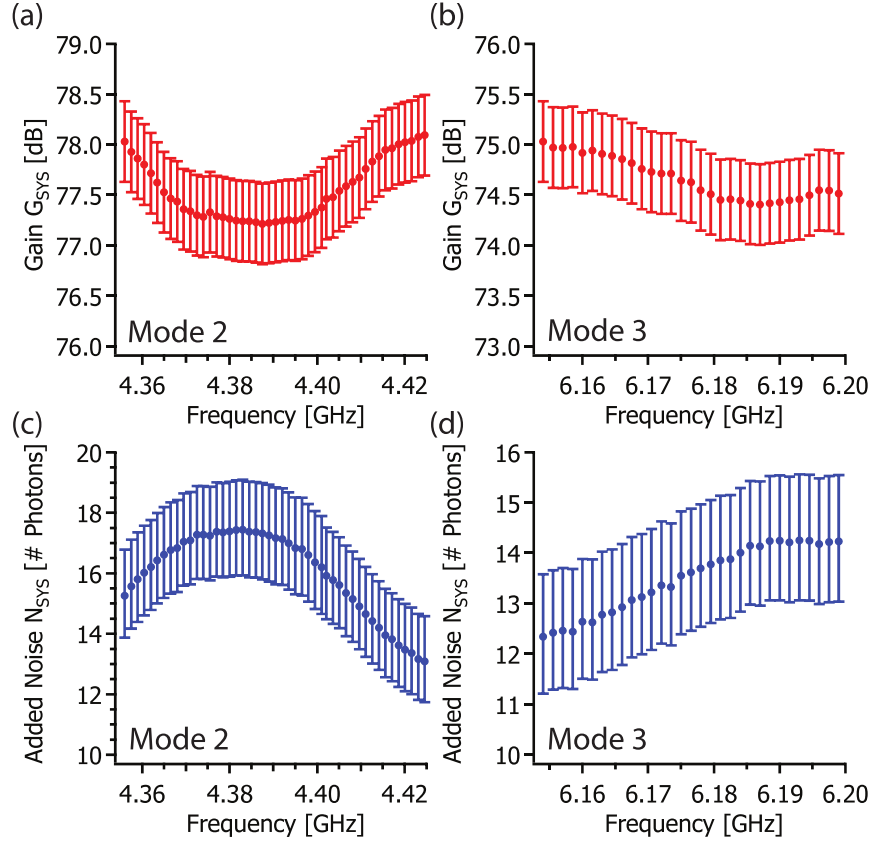


Figure 4.7: *Measurement setup performance.* (a) The gain, G_{SYS} , of the measurement setup in a frequency band around mode 2 (at a DC flux bias of $-0.44\Phi_0$), from the input of the JPA onwards. (b) G_{SYS} , of the measurement setup in a frequency band around mode 3. (c) The added noise, N_{SYS} , of the measurement setup, referred to the input of the JPA, around mode 2. (d) N_{SYS} around mode 3. These have been measured using the method described in Section 3.3. We have measured the combined insertion loss of these components in a separate measurement and found it to be 1.75 ± 0.4 dB for the frequency range around mode 2 and 2.25 ± 0.4 dB for the frequency range around mode 3. The error bars reflect the uncertainty of the insertion loss for the components between the SNTJ and the input of the JPA.

4.2. PARAMETRIC AMPLIFICATION IN A MULTIMODE RESONATOR

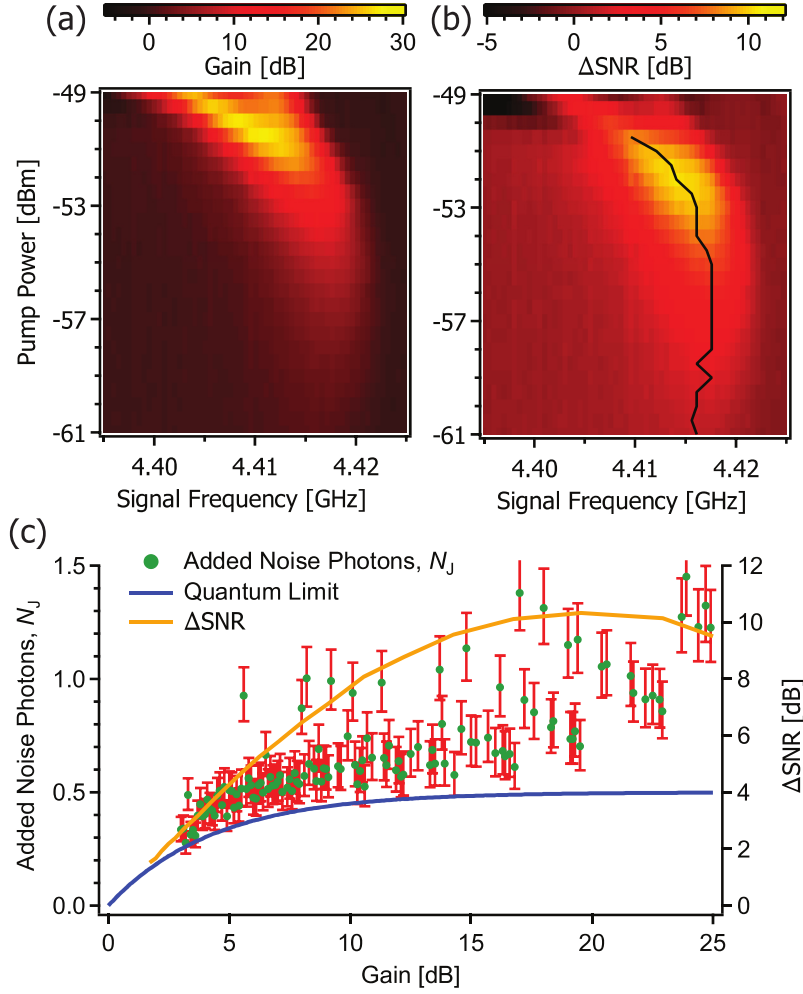


Figure 4.8: Single-mode pumping of mode 2. (a) Power gain, (b) SNR improvement, ΔSNR , observed at $f_p/2 + 100$ kHz. The optimal point of operation is where the maximum ΔSNR is achieved, which is 10.5 dB in this case. The black line in panel (b) marks the points with a maximum ΔSNR as a function of pump power. Panel (c) shows the minimum added noise as a function of gain (in 0.1 dB wide bins). The error bars reflect the uncertainty on the insertion loss of the components installed between the SNTJ and the sample (1.75 ± 0.4 dB). The blue line marks the quantum limit as a function of gain, see Eq. (2.39). The orange line shows the ΔSNR as a function of gain taken along the black line in panel (b).



4. RESULTS

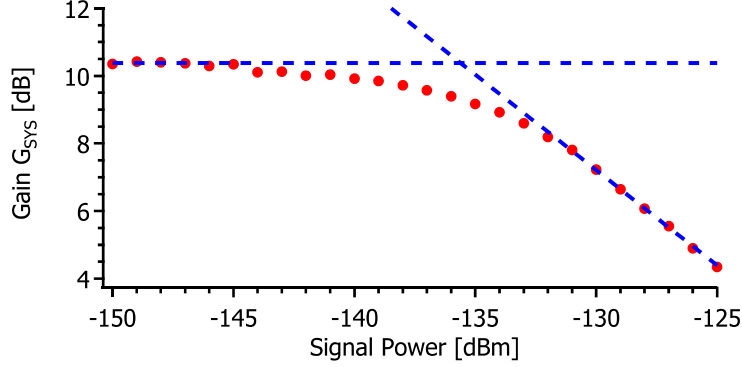


Figure 4.9: Gain compression in mode 2. We show the gain as a function of signal power, when the circuit was biased for a power gain of 10.5 dB. As the signal power increases the gain will start to drop off. The 1 dB compression point (at which the gain is reduced with 1 dB) is found to be at a signal power of -133.5 dBm, referred to the input of the sample. This is to be compared to a 1 dB compression point of -133 dBm and -131 dBm for modes 2 and 3, when using the multimode pumping scheme and when the gain was 11 dB.

the signal frequency and record G_J . This allows us to extract the bandwidth of the JPA, which we do by fitting a Lorentzian to the response, see Fig 6(b) in Paper C. With increasing pump power we can then see that the gain-bandwidth product, \sqrt{GBW} , shows a plateau at 12 MHz. For the higher pump powers (when $G_J > 20$ dB), \sqrt{GBW} starts to drop off, which is most likely due to the crossover into the parametric oscillation regime.

Finally, we have also measured the gain compression. We have done this for a moderate gain, $G_J \approx 10.5$ dB. We do this by biasing the pump for the desired gain and then sweep the signal power. The gain compression is characterized by the 1 dB compression point, the signal power for which the gain is compressed with 1 dB. This occurred at a signal power of -133.5 dBm, referred to the input of the sample. We show the gain as a function of signal power in Fig. 4.9.

4.2.2 Multimode parametric amplification

Two-mode parametric amplification

As I have described in Section 2.2 there exist another operation scheme where the pump is on resonance with the sum of two modes. We again DC flux bias the circuit at $\Phi_{\text{DC}} = -0.44\Phi_0$. At this flux bias the mode frequencies are $f_2 = 4.420$ GHz and $f_3 = 6.219$ GHz. We have measured the gain G_J and the increase in the noise floor in a similar way as in the single-mode case. We sweep the pump frequency, f_p , and pump power tracking the pump at $f_p/2 \pm 899$ MHz, such that the signal ends up in either mode 2 or 3, with a

4.2. PARAMETRIC AMPLIFICATION IN A MULTIMODE RESONATOR

signal offset $\Delta = \pm 500$ kHz. We then measure the power spectrum in a 100 kHz bandwidth around the signal. The G_J and ΔSNR are shown in Fig. 4.10. The maximum ΔSNR is 9.5 dB and 10.5 dB for modes 2 and 3, respectively. We also extracted the minimum added noise as a function of gain in a similar fashion as in the single-mode case. For low gain, the added noise closely follows the quantum limit, but for higher gains the added noise starts to increase.

We also recorded the gain as a function of signal frequency, where we fixed the pump frequency and amplitude. This allowed us to extract the maximum gain and the bandwidth. The gain-bandwidth product $\sqrt{G}\text{BW}$ as a function of P_p is presented in Fig. 8 in Paper C. For low gain, we find $\sqrt{G}\text{BW}$ plateaus at 17.5 MHz for both modes. When increasing P_p , $\sqrt{G}\text{BW}$ starts to drop off when the gain surpasses 20 dB. As before this is most likely when we enter the parametric oscillation regime. Finally we also present the gain compression. We have biased the circuit such that we have approximately 11 dB of gain. We then increased the signal power and the point at which the gain was compressed by 1 dB was -133 dBm and -131 dBm for modes 2 and 3 respectively.

Simultaneous single-mode and two-mode parametric amplification

Finally we also present some measurements where the pump is on resonance with twice the frequency of mode 3. Interestingly, the pump is that at the same time on resonance with sum of the frequencies of mode 2 and mode 4. This is because the spectrum is fairly equidistant due to the limited SQUID participation ratio. Furthermore the widths of the resonances are relatively large due to the modest quality factors. For the flux bias point of $\Phi_{\text{DC}} = -0.445\Phi_0$ the modes are found at 4.398 GHz for mode 2, 6.197 GHz for mode 3 and 8.006 GHz for mode 4. We present measurements of G_J and ΔSNR as a function of f_p and P_p . To measure the response in modes 2 and 4 we track the pump at $f_p/2 \pm 1.8005$ GHz, which gives a $\Delta = \pm 3.5$ MHz. Note that this is significantly larger than the signal detunings used before. As an effect this will lower the maximum gain we can reach. For mode 3 the data is taken at $f_p/2 + 100$ kHz ($\Delta = 100$ kHz.). The results are shown in Fig. 4.11, where we reach a maximum SNR improvement of $\Delta\text{SNR} = 6.7$ dB and $\Delta\text{SNR} = 11.7$ dB for modes 2 and 4 respectively. In mode 3 the maximum SNR improvement was $\Delta\text{SNR} = 11$ dB. Unfortunately it was very difficult to get an accurate calibration of the added noise and the gain of the measurement chain as mode 4 ended up close to the edge of the measurement band (which is 8 GHz). This means that it is impossible to report accurate numbers for the noise performance of this pumping scheme. Nevertheless the reported ΔSNR is similar as for the other pumping schemes.

In conclusion, we have measured parametric amplification in a multimode CPW resonator. We have performed a careful calibration of the measurement setup using a SNTJ. We have shown that we can reach quantum-limited performance in both the single-mode operation scheme as well as in the multimode operation scheme. The optimal point of operation is the point



4. RESULTS

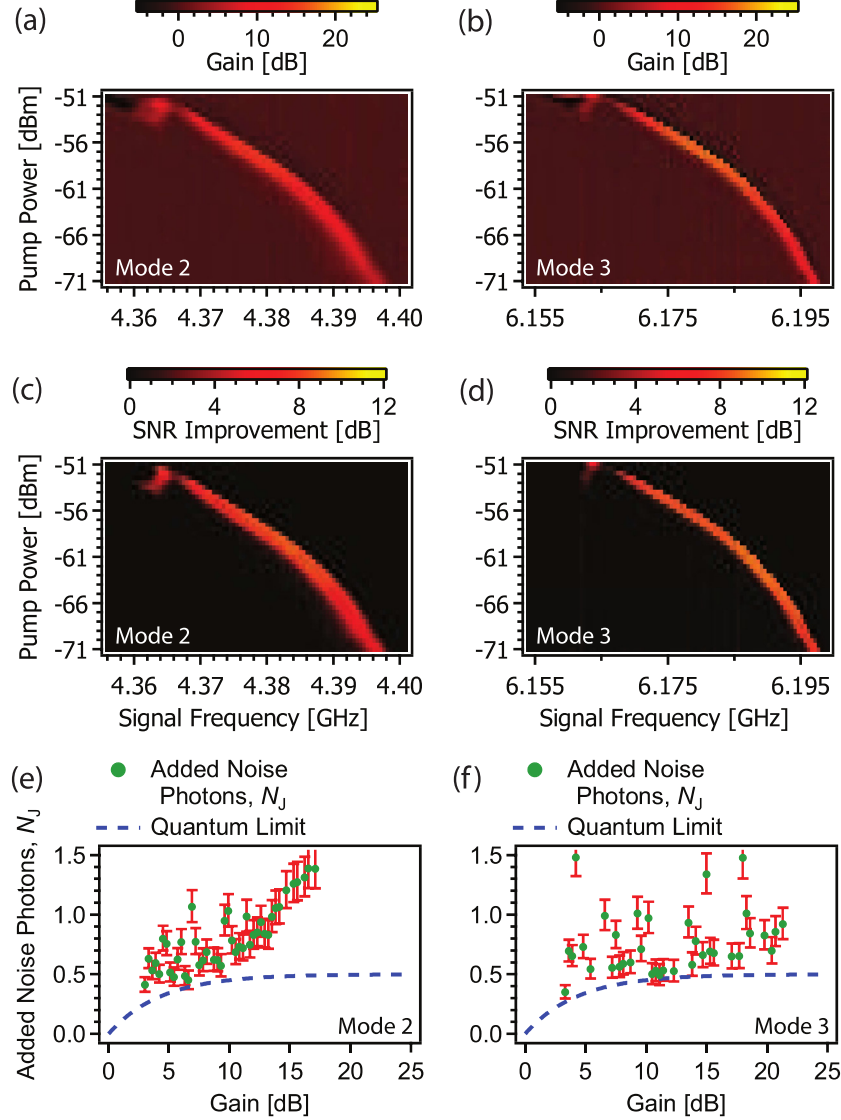


Figure 4.10: Multimode pumping at the sum frequency of modes 2 and 3. (a) and (b) Power gain and (c) and (d) improvement in SNR observed at $f_p/2 - 899$ MHz (mode 2, left column) and at $f_p/2 + 899$ MHz (mode 3, right column). The optimal point of operation gives a maximal Δ SNR of 9.5 dB and 10.5 dB for modes 2 and 3 respectively. Panels (e) and (f) show the minimum added noise as a function of gain (in 0.1 dB wide bins). The error bars reflect the uncertainty on the insertion loss of the components installed between the SNTJ and the sample (1.75 ± 0.4 dB for mode 2 and 2.25 ± 0.4 dB for mode 3). The blue line marks the quantum limit, see Eq. (2.39).

4.2. PARAMETRIC AMPLIFICATION IN A MULTIMODE RESONATOR

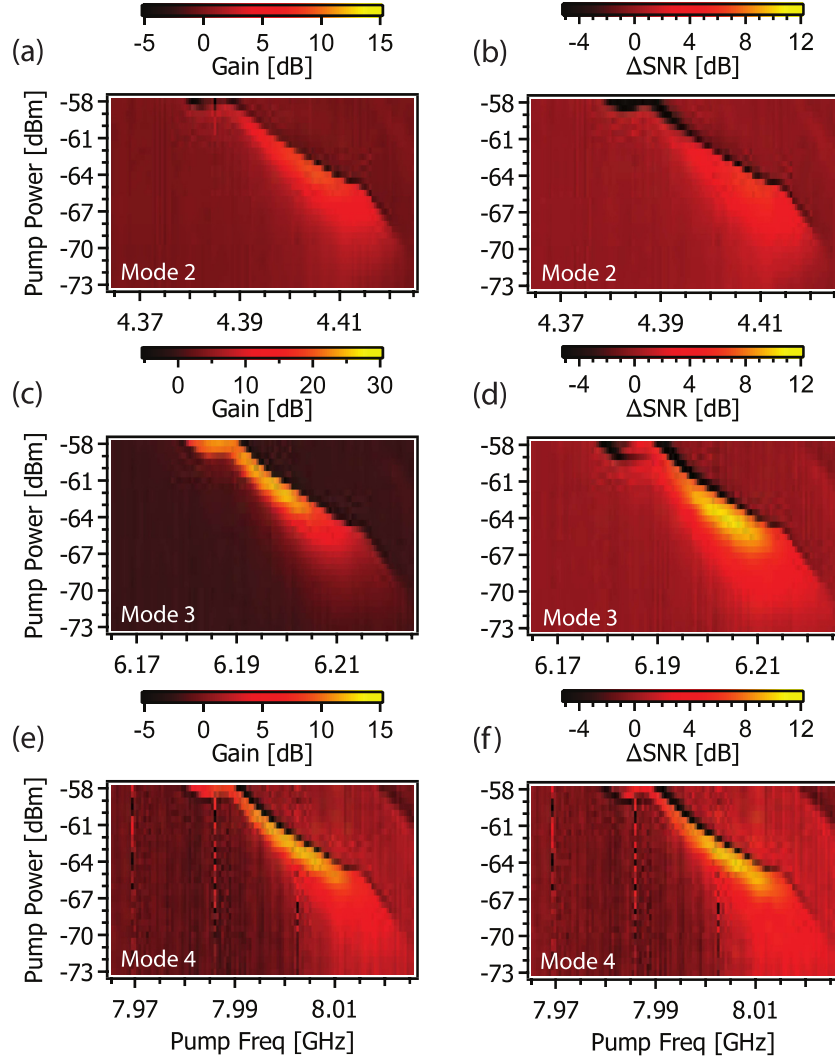


Figure 4.11: *Multimode pumping at twice the frequency of mode 3. (a), (c) and (e) Power gain and (b), (d), (f) improvement in SNR for modes 2, 3 and 4 respectively. The response is measured at $f_p/2 - 1.8005$ GHz (mode 2, top row) , $f_p/2 + 1.8005$ GHz (mode 4, bottom row) and $f_p/2 + 100$ kHz (mode 3, middle row). The optimal point of operation gives a maximal Δ SNR of 6.7 dB, 11 dB and 11.7 dB for modes 2, 3 and 4 respectively. Note that the optimal point of operation is not the same for the combination of modes 2 and 4, compared to mode 3.*



4. RESULTS

with the largest SNR improvement. In the single-mode operation scheme, we reach a $\Delta\text{SNR} = 10.5$ dB. At that point the parametric amplifier adds about 0.7 photons, which translates in a total noise referred to the SNTJ of 1.5 photons (including the noise from the insertion loss and the following amplifiers). In the multimode operation scheme (when pumping at the sum frequency of modes 2 and 3), the maximum $\Delta\text{SNR} = 9.5$ dB for mode 2 and $\Delta\text{SNR} = 10.5$ dB for mode 3. This translates to an added noise by the parametric amplifier of 1.0 photons and 0.7 photons from modes 2 and 3 respectively. Translated to the SNTJ this gives a total noise of 2.59 photons and 1.76 photons. Finally I also presented results where we pump the amplifier at twice the frequency of mode 3. Because of the spectrum is fairly equidistant, we also see amplification in mode 2 and 4 at this point because $2f_3 \approx f_2 + f_4$. The maximal $\Delta\text{SNR} = 6.7$ dB for mode 2, $\Delta\text{SNR} = 11$ dB for mode 3 and $\Delta\text{SNR} = 11.7$ dB for mode 4. It was not possible to do a full noise calibration for mode 4 as the mode frequency was on the edge of the available measurement band.

4.3 Intermode conversion in a multimode resonator

In this section I present my measurements on the intermode conversion between different pairs of modes. I discuss the results found in Paper D and also show some preliminary results where we couple three different modes using two pump frequencies simultaneously.

The sample used in Paper D consists of a quarter-wavelength CPW transmission line resonator with a length of 3 cm, terminated to ground in one end using a SQUID. The inductance of the SQUID at zero magnetic flux, was found to be 223 pH, from a normal resistance measurement resulting in $R_N = 213 \Omega$. This means that the critical current is 1.48 μA . We estimate the SQUID participation ratio $\gamma_0 = 1.95\%$. At the other side of the CPW the resonator is coupled to the measurement line by means of an interdigitated coupling capacitance of 53 fF. The resonator was designed such that the fundamental resonance frequency is close to 1 GHz, just as in the sample used for the parametric amplification measurements presented in Paper C. In order to provide sufficient selectivity between the different pairs of modes, we have used a stepped impedance design. We have divided the resonator into six equal sections. We vary the impedance between the sections by changing the ratio between the width of the center conductor, W_{CPW} , and the gap between the ground planes and the center conductor, G_{CPW} . This is done in such a way that the distance between the ground planes remains constant, ($2G_{\text{CPW}} + W_{\text{CPW}} = 27 \mu\text{m}$), see Fig. 4.12. The exact dimensions were determined by means of a microwave simulation using Microwave Office, where the geometry was optimized to spread out the frequency difference between neighboring modes as far as possible. The resulting design is presented in Table II in Paper D.

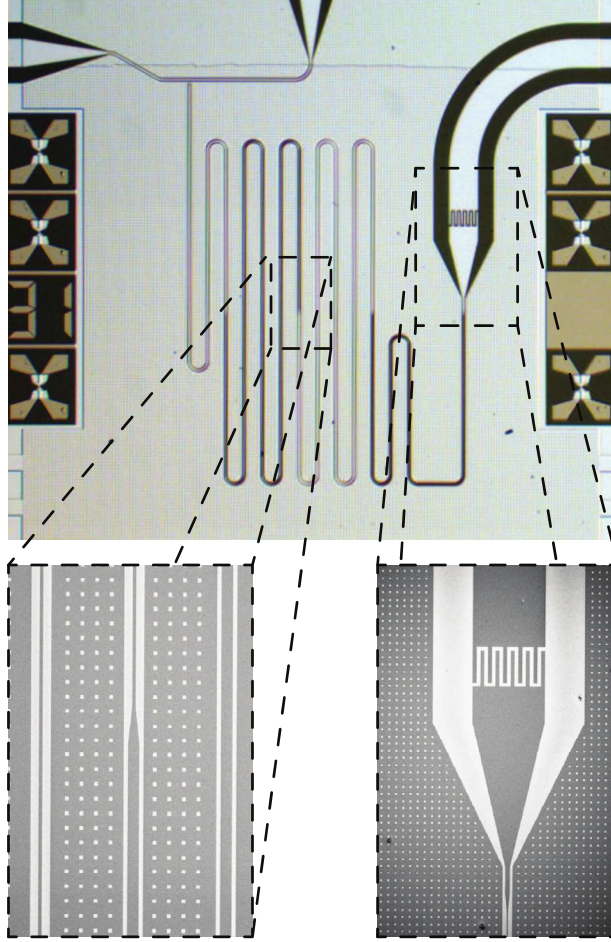


Figure 4.12: A microscope image of the stepped impedance CPW transmission line resonator. The sample consists of a 3 cm long transmission line divided into six sections. The impedance of each section is varied by changing the ratio between the width of the center conductor, W_{CPW} , and the gap between the ground planes and the center conductor, G_{CPW} . This is done in such a way that the distance between the ground planes remains constant, $(2G_{\text{CPW}} + W_{\text{CPW}} = 27 \mu\text{m})$. The bottom left panel shows an SEM image of the taper between the sections. The resonator is coupled to the measurement line by means of an interdigitated coupling capacitance of 53 fF, which is shown in the bottom right panel.



4. RESULTS

The sample is installed at the mixing chamber of a dry dilution cryostat (a Bluefors LD250), with a base temperature of approximately 10 mK, and is measured using a microwave reflectometry setup. In contrast to the setups used in the DCE and parametric amplification measurements, this setup used a wideband cryogenic low-noise HEMT amplifier (a low noise factory LNF_LNC1_12A with a bandwidth of 1 to 12 GHz). The input signal is separated from the output by means of a 20 dB directional coupler. In order to isolate the sample from any noise coming down the amplifier line we have installed two 3 to 12 GHz isolators. This means that we have access to six different modes in the available bandwidth. There is an on-chip tuning line for modulating the magnetic flux through the SQUID loop and an external superconducting coil mounted on the sample holder for DC flux tuning. The measurement setup is given in Fig. 1 in Paper D.

We start out by measuring the spectrum of the resonator as a function of applied magnetic DC flux Φ_{DC} , see Fig. 4.13. I compare the measured resonance positions with the result of the microwave simulations and we see that even though there is an offset between the results and the simulations, the frequency difference between neighboring modes corresponds quite well with the simulations. The exact resonance positions as well as the quality factors of the different modes are given in Table I in Paper D.

We have measured the intermode conversion between modes 2 and 3 and between modes 3 and 4 for different pump frequencies and pump strengths. The measurements are performed at the DC flux bias of $\Phi_{\text{DC}} = 0.45\Phi_0$, where the modes are found at 4.439 GHz, 6.44 GHz and 8.138 GHz. We have measured the reflection coefficient in a frequency range around each of the pumped modes with a vector network analyzer. The phase response of the reflection coefficients are presented in Fig. 4.14 for a pump strength of -42 dBm. Similar to Fig. 2.11 in Section 2.3 we see that we get an avoided level crossing when the pump is exactly on resonance with the difference frequency of the two modes. We have fitted a linecut of the phase response using Eqs. (2.68) and (2.69) where the pump detuning is approximately zero.

We have extracted the coupling between the modes as a function of RMS pump current, see Fig. 4.15. The coupling equals the effective pump strength ϵ . We see that the coupling scales linearly with the RMS pump amplitude. Using Eq. (2.61) we have calculated the AC flux amplitude as a function of RMS pump current, see Fig. 5(b) in Paper D. This shows that we get a maximum coupling of 44 MHz for an AC flux amplitude of 3.5 % of a Φ_0 . From these values we extract a mutual inductance of 2.3 pH between the on-chip flux pump line and the SQUID loop, at $f_p \approx 2$ GHz.

Finally in Fig. 4.16, I also present some preliminary data where we simultaneously apply two pump tones to the sample. The circuit is again biased at $\Phi_{\text{DC}} = 0.45\Phi_0$. The first pump tone has a frequency of 1.704 GHz, which is close to the difference frequency between modes 3 and 4. The pump strength is -51 dBm. This pump hybridizes modes 3 and 4. We then sweep another pump tone in a region around 2 GHz. This pump tone also has a strength of

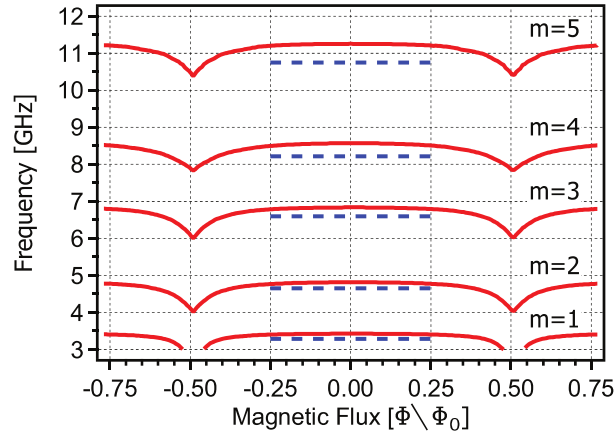


Figure 4.13: The flux tuning of the resonator modes (red full line). The resonator has a fundamental mode of approximately 1 GHz. This gives us access to modes 1 to 5 in the available measurement bandwidth of 3 to 12 GHz. The frequency of the modes can be tuned by means of modulating the magnetic flux through the SQUID. The frequency tuning is periodic with a flux quantum, $\Phi_0 = h/2e$. To be able to address individual pairs of modes, the spectrum needs to be sufficiently non-equidistant with respect to the width of the modes. This has been achieved by varying the characteristic impedance of the CPW throughout the resonator, see Table I in Paper D. The simulation results (for $\Phi_{DC} = 0$) are plotted with the blue dashed line. We see that the frequency difference is matched relatively well even though there is an offset between the measured frequencies and the simulation results.



4. RESULTS

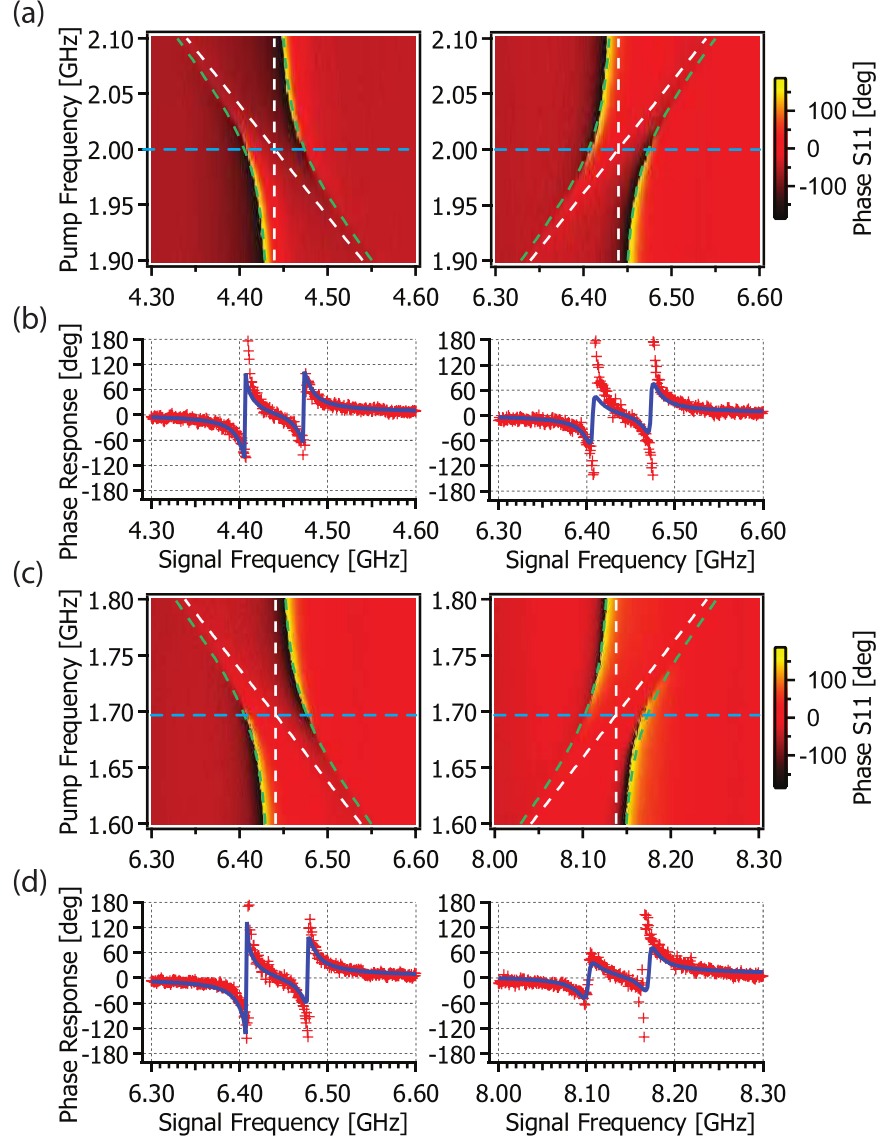


Figure 4.14: Parametric coupling for a pump power of -42 dBm (corresponding to a RMS current of $18 \mu\text{A}$). (a) The coupling of modes 2 and 3. (b) A linecut of the phase response along the blue dashed line in panels (a). The phase response is fitted using Eqs. (2.68) and (2.69) and is given by the blue line. (c) The coupling of modes 3 and 4. (d) A linecut of the phase response along the blue dashed line in panels (c). The phase response is fitted using Eqs. (2.68) and (2.69) and is given by the blue line. The modes are tuned down with a DC magnetic flux, $\Phi_{\text{DC}} = 0.45\Phi_0$, such that the modes end up at 4.439 GHz, 6.44 GHz and 8.138 GHz. In both panels the white dashed lines represent the uncoupled resonances. These resonances get hybridized when the parametric coupling is introduced, see Eq. (2.74) and are represented by the green dashed lines. The minimum splitting as a function of pump frequency is equal to twice the effective pump strength, $2\epsilon/2\pi \approx 70 \text{ MHz}$

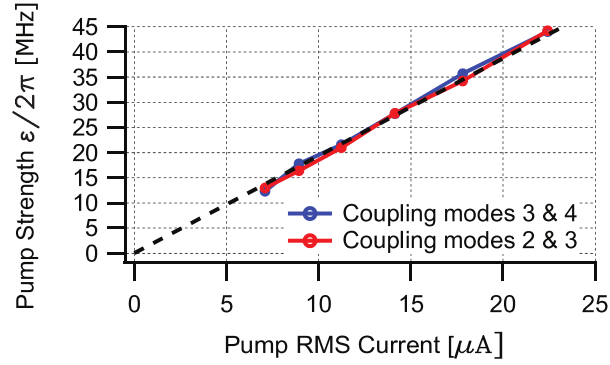


Figure 4.15: *The effective pump strength. We have extracted the effective pump strength, ϵ , as a function of applied pump amplitude for modes 2 and 3 and for modes 3 and 4. To show that ϵ scales linearly with pump amplitude, we have added a linear fit (the black dashed line). The maximum effective pump strength achievable is 44 MHz.*

-51 dBm. We see that when this second pump is on resonance with modes 2 and 3 that a double avoided level crossing occurs indicating the coupling of all three modes.

In conclusion, I have presented the first preliminary measurements on the intermode frequency conversion between the modes of a multimode resonator. The resonator was designed using microwave simulation in order to tailor the spectrum and make it more nonequidistant. This is necessary to provide sufficient selectivity between neighboring pairs of modes. We have shown that we can couple different pairs of modes together with a coupling strength proportional to the pump amplitude. We achieve a maximum coupling strength of 44 MHz for an AC flux modulation amplitude of 3.5% of a Φ_0 . This allows us to determine a mutual inductance of 2.3 pH between the flux pump line and the SQUID loop. Lastly, I have also shown some first preliminary data on the mode coupling between three different modes, using 2 pump tones simultaneously.

4.4 On-chip Mach-Zehnder interferometer

The on-chip-Mach-Zehnder interferometer is a relatively simple device consisting of a $50\ \Omega$ CPW line which is split using a power divider into two $100\ \Omega$ lines. The electrical length of one of these lines is designed such that it has a phase shift of π (for a signal around 5 GHz) compared to the other arm, when they are recombined at the second power splitter (acting as a combiner now). Two SQUIDs in series are embedded into the shorter arm of the two. The SQUID inductance (of one SQUID) at zero flux is estimated to be 0.36 nH from a measurement of the SQUID normal resistance. By tuning the magnetic



4. RESULTS

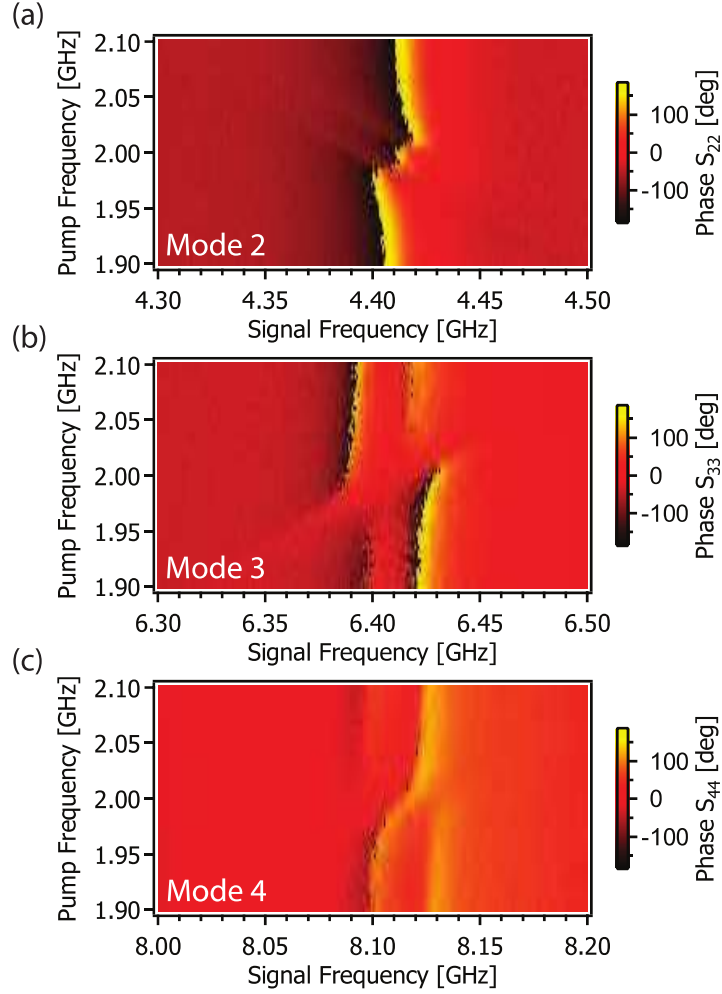


Figure 4.16: *Parametric coupling with two pump tones. (a) The reflection coefficient at mode 2. (b) The reflection coefficient at mode 3 (c) The reflection coefficient at mode 4. (d) The modes are tuned down with a DC magnetic flux, $\Phi_{DC} = 0.45\Phi_0$, such that the modes end up at 4.439 GHz, 6.44 GHz and 8.138 GHz. The first pump tone is applied at 1.704 GHz with a pump strength of -51 dBm. This pump tone will couple modes 3 and 4 together. We then sweep a second pump tone in a region around 2 GHz (also with a strength of -51 dBm). When this pump is on resonance with modes 2 and 3, we couple all three modes together resulting in a double avoided level crossing.*

DC flux through the SQUIDS we can change the SQUID inductance. This results in a phase difference across the SQUID and thus a phase difference between the arms, changing the interference condition at the power combiner. As I discussed in Section 2.5, the power dividers consist of a simple T-junction, which was simulated using Microwave Office. Because the divider is meant to work broadband and lossless, it can not be matched at all three ports and as a result we expect reflections to occur in the interferometer setup.

The sample is cooled down in a ^3He -cryostat with a base temperature of 300 mK. The signal is attenuated on the way down with 50 dB and filtered using an 8 GHz low-pass filter. After the sample there is a circulator installed which is terminated with $50\ \Omega$, and another 8 GHz low-pass filter, to isolate the sample from noise coming down the amplifier line. At the 4 K stage we have a cryogenic low-noise HEMT amplifier of the same type as the ones used in the previous sections. There was an external superconducting coil installed on the sample holder in order to tune the DC magnetic flux. All the measurements were performed using a vector network analyzer to measure the modulation of the transmission coefficient as a function of the applied flux. We present the measurement setup and a picture of the device in Fig. 4.17.

We start by examining the transmission coefficient, S_{21} , as a function of frequency and magnetic flux. We have made microwave simulations, showing the modulation of the transmission through the interferometer, see Fig. 4.18(a). We see that we have a double-dip response, for a low SQUID inductance (0.7 nH). When increasing the inductance, the dips merge together into a single dip around 6.095 MHz. The maximum depth of $-56\ \text{dB}$ is reached at a SQUID inductance of 2.13 nH. When increasing the inductance even further, the dip levels.

When we measure the actual transmission of the device we see a modulation over a large range of frequencies, the strongest modulation is observed around 6.095 GHz which corresponds well with the simulations, see Fig. 4.18(b). When tuning the SQUID inductance to the minimum value ($\Phi = 0$), we do not recover the full well-separated double-dip structure as in the simulations though. This seems to suggest that there is some additional inductance present in the interferometer arm with the SQUID, limiting how far we can lower the inductance in that arm. Lastly we also look at the periodicity of the modulation. We extract the transmission at 6.095 GHz for several flux bias points. These are denoted with the red dots in Fig. 4.18(c). We were not able to make a lot of measurements at large flux values as this requires running large currents through the external coil, which would warm up the cryostat. In order to check the periodicity we have added the dashed line, which is a trace of the measured points (between $-0.5\Phi_0$ and $0.5\Phi_0$) shifted with $\pm\Phi_0$. We see that the few points at larger flux values indeed end up on the dashed line. An interesting observation is that the transmission modulation has a peculiar structure, having a maximum around 0 and around $0.5\Phi_0$. This essentially tells us that the initial phase difference between the two arms is different from π . This means that when we tune the SQUID inductance, and thus the phase



4. RESULTS

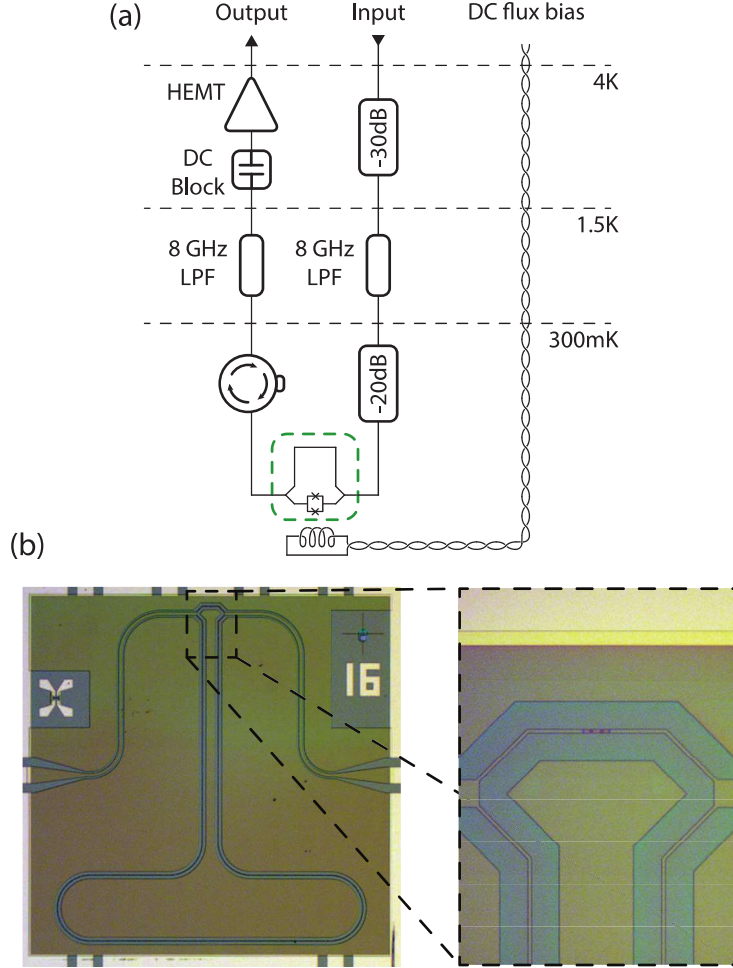


Figure 4.17: *Measurement setup and microscope image of the Mach-Zehnder interferometer. (a) The sample is measured using a ^3He -cryostat with a base temperature of 300 mK. The sample is measured using a transmission setup. The input line is attenuated on the way down with 50 dB and filtered with an 8 GHz low-pass filter before being fed into the sample. On the output line we have a 50Ω terminated circulator providing isolation for any noise coming down the amplifier line. An additional 8 GHz low-pass filter takes care of noise outside of the circulator band. The output is then amplified using a cryogenic low-noise HEMT amplifier of the same type as used in the previously discussed results. The magnetic flux through the SQUID loop is tuned by means of an external superconducting coil mounted on the sample holder. (b) A microscope image of the interferometer. The electrical length of the long arm is designed such that it has a phase shift of π (for a signal around 5 GHz) compared to the shorter arm. Two SQUIDs in series are embedded into the shorter arm of the two. These are shown in the right panel. By tuning the magnetic DC flux through the SQUIDs we can change the SQUID inductance. This results in a phase difference across the SQUID and thus a phase difference between the arms, changing the interference condition at the power combiner.*

difference, we first have a drop in the transmission coefficient (when the phase difference reaches π), before it starts rising again. We see that we reach a phase difference between the arms for a DC magnetic flux value of $0.15 \Phi_0$.

In conclusion, we have designed and performed measurements on a Mach-Zehnder interferometer in the microwave regime. The design showed a behavior similar to the simulations although there seems to be both an offset in the inductance and the initial phase difference between the arms. Interestingly, the difference between the minimal and maximal transmission reaches over 45 dB, which is close to the simulations. We note that any effects limiting the maximum inductance the SQUID can reach, such as junction asymmetry, was not taken into account in the simulations. Neither was the SQUID capacitance taken into account. Most likely there are significant ring resonances in the interferometer which could be mitigated by designing the power splitters such that all ports are matched.



4. RESULTS

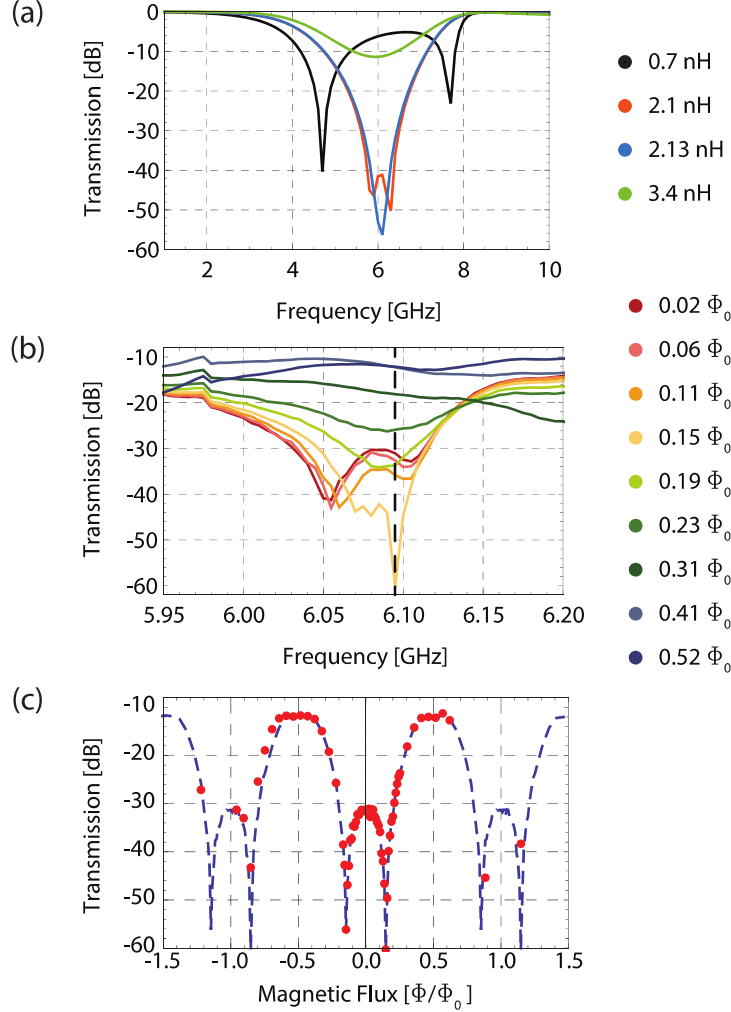


Figure 4.18: Transmission of the Mach-Zehnder interferometer. (a) Simulations show that the transmission is tunable with changing SQUID inductance. For low inductance values the response shows a double dip. Increasing the inductance merges the dips together. The minimum transmission is found at 6.095 GHz. (b) The measured response of the interferometer, in the region around 6.095 GHz, marked with the black dashed line. The results follow the simulation qualitatively with a maximum difference of 45 dB. The splitting of the dips is not as large as in the simulations which suggests the presence of some extra inductance in the arm containing the SQUID. (c) The periodicity of the transmission at 6.095 GHz, emphasized by the added the blue dashed line, which is the measured response between $-0.5\Phi_0$ and $0.5\Phi_0$ shifted with $\pm\Phi_0$. The dip at $n \pm 0.15\Phi_0$, shows that the phase difference between the arms is π at these points.

Conclusions and outlook

In this thesis, I have presented a series of experiments studying the interaction between a parametrically driven system on the one hand and externally applied signals or the vacuum on the other. The experiments were performed at very low temperatures and at microwave frequencies.

I started with the first experimental observation of the dynamical Casimir effect. I have shown that we observed broadband radiation from a SQUID terminated CPW transmission line. This radiation is the result of the parametric amplification of vacuum fluctuations by means of a modulated boundary condition on the electromagnetic field. The dynamical Casimir effect produces photons in pairs, which manifests itself in correlations of the radiation generated symmetrically around half the pump frequency. We have investigated these correlations in the form of two-mode squeezing and second-order photon correlations. Theory states that the photons produced at these symmetric frequencies should also be entangled. In future work I think it is necessary to explicitly prove that the radiation is entangled, by sufficiently squeezing the output radiation.⁷² Further experiments are also needed to show the parabolic shape of the spectrum of the produced radiation. For this measurement a wideband setup will be required.

I have also presented measurements on the interaction of a parametrically pumped multimode resonator with classical signals. We have used the parametric amplifier both in the single-mode operation scheme, where signals falling within a single mode will be amplified, as well as in the multimode operation scheme, where the circuit is modulated at the sum of two mode frequencies. In both cases we have shown, after a careful calibration of the measurement setup, that we reached quantum-limited noise performance. I have presented measurements of the gain and bandwidth of the amplifier. The 1 dB-compression power was found to be very modest, and in future work it could be valuable to try to improve the compression point by for instance changing the critical current of the SQUID.

We have used a similar multimode resonator to measure the frequency



5. CONCLUSIONS AND OUTLOOK

conversion between two of the modes, when the system is pumped at the difference frequency of two modes. The resonator was modified using a stepped-impedance design in order to make the spectrum less equidistant. As a result we were able to selectively couple individual pairs of neighboring modes. I have presented some preliminary results showing the avoided level crossing resulting from the intermode conversion by measuring the reflection coefficient of the coupled modes. I have extracted the coupling strength as a function of applied pump amplitude and shown a linear dependence. This has allowed me to extract the mutual inductance between the on-chip flux line and the SQUID loop. I also present some measurements where we applied two different pump tones, coupling three different modes together. What remains to be done are measurements where the output of one of the coupled modes is recorded when applying a signal to the other one, which would be a direct measurement of the intermode conversion. I believe that these different parametric effects (amplification and intermode conversion) can potentially be useful for the distribution of entangled radiation over several modes of the same resonator. This could potentially be used to measure multipartite entanglement and is a possible candidate for continuous-variable quantum computing using cluster states.⁷³

In Chapter 2, I have presented a theoretical model which can be used to study parametric amplification using a parametrically modulated SQUID. I have treated the case of degenerate amplification, where the signal is at half the pump frequency. In that case the signal and idler interfere with each other providing quadrature dependent gain. This so called pumpistor model provides an intuitive equivalent circuit which will contain a “pumpistor” element which has an impedance depending on the pump phase. This model has been shown to work well for a degenerately pumped parametric amplifier, and it has also been extended to nondegenerate amplification in more recent work.²⁷

Finally, we have also measured a Mach-Zehnder interferometer in the microwave regime. This circuit uses the variable inductance of the SQUID in one of the arms to change the phase difference between the arms. In doing so the interference conditions can be changed yielding a maximum change in transmission through the interferometer of 45 dB. The device uses a simple design of a power splitter which is hampered by the fact that it is not matched at all three ports. This will result in a large amount of internal reflection. As the length of the fixed arm of the interferometer is designed for a specific frequency, it should be possible to redesign the power splitters opting instead for a more complicated microwave coupler such that the internal reflection can be reduced.

Appendix A

Recipes for sample fabrication

A.1 Wafer cleaning

1. Dip the wafer in 1165 remover at 60 to 70 °C for 10 min.
2. Place the wafer, in a beaker of 1165 remover, in an ultrasonic bath at maximum power for 1 min.
3. Place the wafer in a bath of IPA for 2 min.
4. Dip the wafer in the QDR bath.
5. Blow dry the wafer.
6. Plasma etch with the Batchtop: 40 sccm O₂ at a pressure of 500 mT and a plasma power of 250 W for 1 min.
7. Optionally: Dip the wafer in and HF bath for 30 s and blow dry.

A.2 Photolithography for lift-off

1. Prebake the wafer for 1 min at 110 °C.
2. Spin resist LOR3B: acceleration time 1.5 s to 3000 rpm for 1 min.
3. Bake the wafer for 5 min at 200 °C.
4. Spin resist S1813: acceleration time 1.5 s to 3000 rpm for 1 min.
5. Bake the wafer for 2 min at 110 °C.

6. Expose with the MA6 mask aligner: Lo-Vac Mode (0.4 mbar) for 8.5 s.
7. Develop using MF319 for 45 s.
8. Ash using the Batchtop: 10 sccm O₂ at a pressure of 250 mT and a plasma power of 50 W for 10 s.

A.3 Deposition of the contact pads

1. Using the Lesker evaporator:
 - Deposit 30 Å of Ti at 1 Å/s.
 - Deposit 800 Å of Au at 1 to 2 Å/s.
 - Deposit 100 Å of Pd at 1 Å/s.
2. Lift-off using remover 1165 at 70 °C for approximately 30 min.

A.4 Protective resist and dicing

1. Spin resist S1813: acceleration time 1 s to 2000 rpm for 1 min.
2. Bake the wafer for 2 min at 110 °C.
3. Dice the wafer from the backside leaving approximately 170 µm.
4. Dip the wafer in 1165 remover at 60 to 70 °C for 15 min.
5. Place the wafer in a bath of IPA for 2 min.
6. Dip the wafer in the QDR bath.
7. Blow dry the wafer.

A.5 Electron-beam lithography for lift-off

1. Spin resist EL10: acceleration time 2 s to 500 rpm for 5 s and then acceleration time 0.5 s to 2000 rpm for 45 s.
2. Softbake the wafer for 5 min at 170 °C.
3. Spin resist ZEP520A (1:1 dilution): acceleration time 0.5 s, 3000 rpm for 45 min.
4. Softbake the wafer for 5 min at 160 °C.
5. Expose the wafer using an electron-beam lithography system.
6. Develop the top resist using o-Xylene for 2 min.

7. Dip briefly in IPA.
8. Blow dry the wafer and divide into individual chips.
9. Develop the bottom layer using an H_2O :IPA solution (1:4 dilution).
10. Rinse in IPA.
11. Blow dry gently.

A.6 Two-angle evaporation and lift-off

1. Ash using the Batchtop: 10 sccm O_2 at a pressure of 250 mT and a plasma power of 50 W for 10 s.
2. Two-angle evaporation using the Plassys (exact parameters need to be tweaked for correct junction resistance):
 - Deposit 40 nm of Al at 0.5 Å/s at an angle of 28° .
 - Dynamic oxidation using O_2 at 0.2 mbar for 30 min.
 - Deposit 50 nm of Al at 0.5 Å/s at an angle of -28° .
 - Static oxidation using 100 sccm of O_2 at 10 mbar for 4 min.
3. Lift-off using remover 1165 at 70°C for approximately 15 min.
4. Rinse in IPA.
5. Rinse in Methanol.
6. Blow dry.

References

- [1] C. M. Wilson, G. Johansson, A. Pourkabirian, M. Simoen, J. R. Johansson, T. Duty, F. Nori, and P. Delsing. Observation of the dynamical Casimir effect in a superconducting circuit. *Nature* **479**: 376, 2011. DOI: 10.1038/nature10561.
- [2] K. M. Sundqvist, S. Kintaş, M. Simoen, P. Krantz, M. Sandberg, C. M. Wilson, and P. Delsing. The pumpistor: A linearized model of a flux-pumped superconducting quantum interference device for use as a negative-resistance parametric amplifier. *Applied Physics Letters* **103**: 102603, 2013. DOI: 10.1063/1.4819881.
- [3] M. Simoen, C. W. S. Chang, P. Krantz, J. Bylander, W. Wustmann, V. Shumeiko, P. Delsing, and C. M. Wilson. Characterization of a multimode coplanar waveguide parametric amplifier. *Journal of Applied Physics* **118**: 154501, 2015. DOI: 10.1063/1.4933265.
- [4] M. Simoen, A. Bengtsson, J. Bylander, W. Wustmann, V. Shumeiko, C. M. Wilson, and P. Delsing. Intermode conversion in a superconducting multimode resonator. *Unpublished manuscript*, 2015.
- [5] S. Schuermans, M. Simoen, M. Sandberg, P. Krantz, C. M. Wilson, and P. Delsing. An on-chip Mach-Zehnder interferometer in the microwave regime. *IEEE Transactions on Applied Superconductivity* **21**: 448, 2011. DOI: 10.1109/TASC.2010.2088354.
- [6] M. U. Staudt, I.-C. Hoi, P. Krantz, M. Sandberg, M. Simoen, P. Bushev, N. Sangouard, M. Afzelius, V. S. Shumeiko, G. Johansson, P. Delsing, and C. M. Wilson. Coupling of an erbium spin ensemble to a superconducting resonator. *Journal of Physics B: Atomic, Molecular and Optical Physics* **45**: 124019, 2012. DOI: 10.1088/0953-4075/45/12/124019.
- [7] P. Krantz, A. Bengtsson, M. Simoen, S. Gustavsson, V. Shumeiko, W. D. Oliver, C. M. Wilson, P. Delsing, and J. Bylander. Single-shot readout of a superconducting qubit using a Josephson parametric oscillator. arXiv: 1508.02886.
- [8] M. Faraday. On a peculiar class of acoustical figures; and on certain forms a by groups of particles upon vibrating elastic surfaces. *Philosophical Transactions of the Royal Society of London* **121**: 299, 1831. DOI: 10.1098/rstl.1831.0018.

- [9] J. W. S. B. Rayleigh. XXXIII. On maintained vibrations. *Philosophical Magazine Series 5* **15**: 229, 1883. DOI: 10.1080/14786448308627342.
- [10] J. W. S. B. Rayleigh. XVII. On the maintenance of vibrations by forces of double frequency, and on the propagation of waves through a medium endowed with a periodic structure. *Philosophical Magazine Series 5* **24**: 145, 1887. DOI: 10.1080/14786448708628074.
- [11] E. Alexanderson and S. Nixdorff. A magnetic amplifier for radio telephony. *Proceedings of the IRE* **4**: 101, 1916. DOI: 10.1109/JRPROC.1916.217224.
- [12] M. O. Scully and M. S. Zubairy. *Quantum optics*. Cambridge University Press, 1997.
- [13] B. S. DeWitt. Quantum field theory in curved spacetime. *Physics Reports* **19**: 295, 1975. DOI: 10.1016/0370-1573(75)90051-4.
- [14] S. A. Fulling and P. C. W. Davies. Radiation from a moving mirror in two dimensional space-time: conformal anomaly. *Proceedings of the Royal Society A: Mathematical, Physical and Engineering Sciences* **348**: 393, 1976. DOI: 10.1098/rspa.1976.0045.
- [15] G. T. Moore. Quantum theory of the electromagnetic field in a variable-length one-dimensional cavity. *Journal of Mathematical Physics* **11**: 2679, 1970. DOI: 10.1063/1.1665432.
- [16] V. V. Dodonov. Current status of the dynamical Casimir effect. *Physica Scripta* **82**: 038105, 2010. DOI: 10.1088/0031-8949/82/03/038105.
- [17] J. D. Teufel, T. Donner, M. A. Castellanos-Beltran, J. W. Harlow, and K. W. Lehnert. Nanomechanical motion measured with an imprecision below that at the standard quantum limit. *Nature nanotechnology* **4**: 820, 2009. DOI: 10.1038/nnano.2009.343.
- [18] B. Abdo, F. Schackert, M. Hatridge, C. Rigetti, and M. Devoret. Josephson amplifier for qubit readout. *Applied Physics Letters* **99**: 162506, 2011. DOI: 10.1063/1.3653473.
- [19] M. Hatridge, S. Shankar, M. Mirrahimi, F. Schackert, K. Geerlings, T. Brecht, K. M. Sliwa, B. Abdo, L. Frunzio, S. M. Girvin, R. J. Schoelkopf, and M. H. Devoret. Quantum back-action of an individual variable-strength measurement. *Science* **339**: 178, 2013. DOI: 10.1126/science.1226897.
- [20] E. Jeffrey, D. Sank, J. Y. Mutus, T. C. White, J. Kelly, R. Barends, Y. Chen, Z. Chen, B. Chiaro, A. Dunsworth, A. Megrant, P. J. J. O'Malley, C. Neill, P. Roushan, A. Vainsencher, J. Wenner, A. N. Cleland, and J. M. Martinis. Fast accurate state measurement with superconducting qubits. *Physical Review Letters* **112**: 190504, 2014. DOI: 10.1103/PhysRevLett.112.190504.
- [21] R. Vijay, D. H. Slichter, and I. Siddiqi. Observation of quantum jumps in a superconducting artificial atom. *Physical Review Letters* **106**: 110502, 2011. DOI: 10.1103/PhysRevLett.106.110502.
- [22] R. Vijay, C. Macklin, D. H. Slichter, S. J. Weber, K. W. Murch, R. Naik, A. N. Korotkov, and I. Siddiqi. Stabilizing Rabi oscillations in a

- superconducting qubit using quantum feedback. *Nature* **490**: 77, 2012. DOI: 10.1038/nature11505.
- [23] F. Mallet, M. A. Castellanos-Beltran, H. S. Ku, S. Glancy, E. Knill, K. D. Irwin, G. C. Hilton, L. R. Vale, and K. W. Lehnert. Quantum state tomography of an itinerant squeezed microwave field. *Physical Review Letters* **106**: 220502, 2011. DOI: 10.1103/PhysRevLett.106.220502.
 - [24] E. Zakka-Bajjani, F. Nguyen, M. Lee, L. R. Vale, R. W. Simmonds, and J. Aumentado. Quantum superposition of a single microwave photon in two different 'colour' states. *Nature Physics* **7**: 599, 2011. DOI: 10.1038/nphys2035.
 - [25] E. Flurin, N. Roch, J. D. Pillet, F. Mallet, and B. Huard. Superconducting quantum node for entanglement and storage of microwave radiation. *Physical review letters* **114**: 090503, 2015. DOI: 10.1103/PhysRevLett.114.090503.
 - [26] A. J. Sirois, M. A. Castellanos-Beltran, M. P. DeFeo, L. Ranzani, F. Lecocq, R. W. Simmonds, J. D. Teufel, and J. Aumentado. Coherent-state storage and retrieval between superconducting cavities using parametric frequency conversion. *Applied Physics Letters* **106**: 172603, 2015. DOI: 10.1063/1.4919759.
 - [27] K. M. Sundqvist and P. Delsing. Negative-resistance models for parametrically flux-pumped superconducting quantum interference devices. *EPJ Quantum Technology* **1**, 2014. DOI: 10.1140/epjqt6.
 - [28] M. G. A. Paris. Entanglement and visibility at the output of a Mach-Zehnder interferometer. *Physical Review A* **59**: 1615, 1999. DOI: 10.1103/PhysRevA.59.1615.
 - [29] H. Onnes. The superconductivity of mercury. *Commun. Phys. Lab. Univ. Leiden*, 1911.
 - [30] J. Bardeen, L. N. Cooper, and J. R. Schrieffer. Theory of superconductivity. *Physical Review* **108**: 1175, 1957. DOI: 10.1103/PhysRev.108.1175.
 - [31] L. Cooper. Bound electron pairs in a degenerate Fermi gas. *Physical Review* **104**: 1189, 1956. DOI: 10.1103/PhysRev.104.1189.
 - [32] B. Josephson. Possible new effects in superconductive tunnelling. *Physics Letters* **1**: 251, 1962. DOI: 10.1016/0031-9163(62)91369-0.
 - [33] V. Ambegaokar and A. Baratoff. Tunneling between superconductors. *Physical Review Letters* **10**: 486, 1963. DOI: 10.1103/PhysRevLett.10.486.
 - [34] V. Ambegaokar and A. Baratoff. Tunneling between superconductors. *Physical Review Letters* **11**: 104, 1963. DOI: 10.1103/PhysRevLett.11.104.
 - [35] J. Waldram. *Superconductivity of metals and cuprates*. CRC Press, 1996.
 - [36] M. Sandberg. *Fast-tunable resonators and quantum electrical circuits*. Chalmers University of Technology, 2009.
 - [37] F. Persson. *Fast dynamics and measurements of single-charge devices*. Chalmers University of Technology, 2010.
 - [38] D. M. Pozar. *Microwave Engineering, 4th Edition*. Wiley, 2011.

- [39] J. Bourassa, F. Beaudoin, J. M. Gambetta, and A. Blais. Josephson-junction-embedded transmission-line resonators: From Kerr medium to in-line transmon. *Physical Review A* **86**: 013814, 2012. DOI: 10.1103/PhysRevA.86.013814.
- [40] M. Wallquist, V. Shumeiko, and G. Wendin. Selective coupling of superconducting charge qubits mediated by a tunable stripline cavity. *Physical Review B* **74**: 224506, 2006. DOI: 10.1103/PhysRevB.74.224506.
- [41] C. M. Caves. Quantum limits on noise in linear amplifiers. *Physical Review D* **26**: 1817, 1982.
- [42] M. Abramowitz and I. A. Stegun. *Handbook of mathematical functions: with formulas, graphs, and mathematical tables*. Dover Publications, 1964.
- [43] W. Wustmann and V. Shumeiko. Parametric resonance in tunable superconducting cavities. *Physical Review B* **87**: 184501, 2013. DOI: 10.1103/PhysRevB.87.184501.
- [44] W. Wustmann and V. Shumeiko. *To be published*, 2015.
- [45] H. Casimir. On the attraction between two perfectly conducting plates. *Proc. Kon. Ned. Akad. Wetenschappen* **51**: 793, 1948.
- [46] W. Heisenberg. Über den anschaulichen Inhalt der quantentheoretischen Kinematik und Mechanik. *Zeitschrift für Physik* **43**: 172, 1927. DOI: 10.1007/BF01397280.
- [47] S. K. Lamoreaux. Demonstration of the Casimir force in the 0.6 to 6 μ m range. *Physical Review Letters* **78**: 5, 1997. DOI: 10.1103/PhysRevLett.78.5.
- [48] J. Schwinger. Casimir energy for dielectrics. *Proceedings of the National Academy of Sciences* **89**: 4091, 1992. DOI: 10.1073/pnas.89.9.4091.
- [49] E. Yablonovitch. Accelerating reference frame for electromagnetic waves in a rapidly growing plasma: Unruh-Davies-Fulling-DeWitt radiation and the nonadiabatic Casimir effect. *Physical Review Letters* **62**: 1742, 1989. DOI: 10.1103/PhysRevLett.62.1742.
- [50] A. Lambrecht, M.-T. Jaekel, and S. Reynaud. Motion induced radiation from a vibrating cavity. *Physical review letters* **77**: 615, 1996.
- [51] A. A. Clerk, M. H. Devoret, S. M. Girvin, F. Marquardt, and R. J. Schoelkopf. Introduction to quantum noise, measurement, and amplification. *Reviews of Modern Physics* **82**: 1155, 2010. DOI: 10.1103/RevModPhys.82.1155.
- [52] W. G. Unruh. Notes on black-hole evaporation. *Physical Review D* **14**: 870, 1976. DOI: 10.1103/PhysRevD.14.870.
- [53] S. W. Hawking. Black hole explosions? *Nature* **248**: 30, 1974. DOI: 10.1038/248030a0.
- [54] S. W. Hawking. Particle creation by black holes. *Communications in Mathematical Physics* **43**: 199, 1975.
- [55] P. D. Nation, J. R. Johansson, M. P. Blencowe, and F. Nori. Colloquium : Stimulating uncertainty: Amplifying the quantum vacuum with superconducting circuits. *Reviews of Modern Physics* **84**, 2012. DOI: 10.1103/RevModPhys.84.1.

- [56] J. Johansson, G. Johansson, C. Wilson, and F. Nori. Dynamical Casimir effect in superconducting microwave circuits. *Physical Review A* **82**: 052509, 2010. DOI: 10.1103/PhysRevA.82.052509.
- [57] P. Lahteenmaki, G. S. Paraoanu, J. Hassel, and P. J. Hakonen. Dynamical Casimir effect in a Josephson metamaterial. *Proceedings of the National Academy of Sciences* **110** (11): 4234, 2013. DOI: 10.1073/pnas.1212705110.
- [58] F. X. Dezael and A. Lambrecht. Analogue Casimir radiation using an optical parametric oscillator. *EPL (Europhysics Letters)* **89**: 14001, 2010. DOI: 10.1209/0295-5075/89/14001.
- [59] J. Johansson, G. Johansson, C. Wilson, and F. Nori. Dynamical Casimir effect in a superconducting coplanar waveguide. *Physical Review Letters* **103**: 147003, 2009. DOI: 10.1103/PhysRevLett.103.147003.
- [60] C. M. Caves and B. L. Schumaker. New formalism for two-photon quantum optics. I. Quadrature phases and squeezed states. *Physical Review A* **31**: 3068, 1985.
- [61] I.-C. Hoi. *Quantum optics with propagating microwaves in superconducting circuits*. Chalmers University of Technology, 2013.
- [62] L. Mach. Ueber einen Interferenzrefraktor. *Zeitschrift für Instrumentenkunde* **12**: 89, 1892.
- [63] L. Zehnder. Ein neuer Interferenzrefraktor. *Zeitschrift für Instrumentenkunde* **11**: 275, 1891.
- [64] T. Young. The Bakerian lecture: Experiments and calculations relative to physical optics. *Phil. Trans. R. Soc. Lond.* **94**, 1804.
- [65] H. Eisenmann, T. Waas, and H. Hartmann. PROXECCO—Proximity effect correction by convolution. *Journal of Vacuum Science & Technology B: Microelectronics and Nanometer Structures* **11**: 2741, 1993. DOI: 10.1116/1.586594.
- [66] G. J. Dolan. Offset masks for lift-off photoprocessing. *Applied Physics Letters* **31**: 337, 1977. DOI: 10.1063/1.89690.
- [67] G. K. White and P. Meeson. *Experimental techniques in low-temperature physics*. 4th ed. OUP Oxford, 2002.
- [68] A. T. A. M. de Waele. Basic operation of cryocoolers and related thermal machines. *Journal of Low Temperature Physics* **164**: 179, 2011. DOI: 10.1007/s10909-011-0373-x.
- [69] P. D. Nissen. *Closed cycle refrigerators - Pulse tube coolers*. Tech. rep. Nano-Science Center, Niels Bohr Institute, University of Copenhagen, 2010.
- [70] L. Spietz, K. W. Lehnert, I. Siddiqi, and R. J. Schoelkopf. Primary electronic thermometry using the shot noise of a tunnel junction. *Science* **300**: 1929, 2003. DOI: 10.1126/science.1084647.
- [71] L. Spietz, R. J. Schoelkopf, and P. Pari. Shot noise thermometry down to 10 mK. *Applied Physics Letters* **89**: 183123, 2006. DOI: 10.1063/1.2382736.

- [72] J. R. Johansson, G. Johansson, C. M. Wilson, P. Delsing, and F. Nori. Nonclassical microwave radiation from the dynamical Casimir effect. *Physical Review A* **87**: 043804, 2013. DOI: 10.1103/PhysRevA.87.043804.
- [73] D. E. Bruschi, C. Sabín, P. Kok, G. Johansson, P. Delsing, and I. Fuentes. Towards universal quantum computation through relativistic motion. arXiv: 1311.5619.